Titre: Title:	Time-Dependent Damage in Woven-Ply Thermoplastic Composites Above Glass Transition Temperature
Auteur: Author:	David Bouscarrat
Date:	2019
Type:	Mémoire ou thèse / Dissertation or Thesis
Référence: Citation:	Bouscarrat, D. (2019). Time-Dependent Damage in Woven-Ply Thermoplastic Composites Above Glass Transition Temperature [Thèse de doctorat, Polytechnique Montréal]. PolyPublie. https://publications.polymtl.ca/4190/

URL de PolyPublie: PolyPublie URL:	https://publications.polymtl.ca/4190/
Directeurs de recherche: Advisors:	Martin Lévesque, & Benoit Vieille
Programme: Program:	Génie mécanique

POLYTECHNIQUE MONTRÉAL
affiliée à l'Université de Montréal
et
INSA DE ROUEN

Time-dependent damage in woven-ply thermoplastic composites above glass transition temperature

DAVID BOUSCARRAT
Département de Génie mécanique

Thèse présentée en vue de l'obtention du diplôme de *Philosophiæ Doctor*
Génie mécanique

Décembre 2019

POLYTECHNIQUE MONTRÉAL
affiliée à l'Université de Montréal
et
INSA DE ROUEN

Cette thèse intitulée :

Time-dependent damage in woven-ply thermoplastic composites above glass transition temperature

présentée par **David BOUSCARRAT**
en vue de l'obtention du diplôme de *Philosophiæ Doctor*
a été dûment acceptée par le jury d'examen constitué de :

Daniel THERRIAULT, président
Martin LÉVESQUE, membre et directeur de recherche
Benoit VIEILLE, membre et codirecteur de recherche
Louis LABERGE LEBEL, membre
Nathalie GODIN, membre externe
Fodil MERAGHNI, membre externe

DEDICATION

To my family, especially my mother, who have always supported me, thank you.

ACKNOWLEDGEMENTS

First of all, I would like to thank INSA Rouen and Polytechnique Montréal for allowing me to carry out this thesis in co-supervision.

My special thanks go to my supervisors, Benoit and Martin, who supported me throughout my thesis: Benoit, for supporting me regularly with constructive advice, and Martin, for his critical point of view and his rigor.

I would like to thank the members of the jury, Nathalie Godin, Daniel Therriault, Fodil Meraghni and Louis Laberge Lebel, for agreeing to judge my thesis work. Their comments and questions showed the importance of this subject and enabled to improve this manuscript and to highlight the different perspectives for the continuation of this work.

I would also like to thank all the people who were involved, in one way or another, in this accomplishment. Thanks to Christophe Bouvet and Pierre Journoud (Institut Clément Ader) for the tomographic observations. I would also like to thank Cristhophe Gautrelet for helping me several times. Thanks again to the researchers of the GPM EIRCAP team for allowing me access to some equipment.

Many thanks to my office neighbours and colleagues (and friends) from France: Gael, Yann, Baptiste, Luc, Daniel, Oscar, Mathieu, Yan, Asih and Alireza; and from Canada: Ilyass, Rolland and Léo, for their support and patience. I would also like to thank the other members of the GPM ERMECA team: Clément, Fabrice, Alain, Mouldi, Josianne, Yosra, Morganne and Estève. A special and personal thank you to Elisabeth for her good mood and her availability.

Finally, a special thanks to my family for having always supported me during all this time. And a special thought to my mother who has always inspired me to move forward.

RÉSUMÉ

Dans les composites associant matrice organique et renfort fibreux, le couplage entre comportements visqueux (viscoélasticité, viscoplasticité) et mécanismes d'endommagement est très peu étudié à l'échelle mésoscopique et se limite principalement à des analyses post-mortem. Pour des applications aéronautiques à haute température (*e.g.*, nacelle de moteur d'avion), la problématique est encore plus complexe. Notamment au sein de stratifiés à matrice thermoplastique haute performance PPS renforcés par des tissus de fibres de carbone. Ces matériaux sont caractérisés par des zones riches en matrice dont les comportements visqueux sont amplifiés pour des températures d'utilisation en service (*i.e.*, 120 °C) supérieures à la température de transition vitreuse de la matrice (environ 95 °C).

La question fondamentale qui se pose alors est de comprendre comment mettre en évidence et quantifier l'endommagement d'origine visqueuse lorsque le comportement de stratifiés C/PPS est piloté par la réponse mécanique de la matrice. Pour apporter des réponses à cette problématique, on peut évaluer : (1) l'influence de la viscosité de la matrice sur le comportement en rupture translaminaire - (2) le visco-endommagement lors de chargements de type fluage-recouvrement. Ces deux axes d'étude reposent notamment sur la mise au point de protocoles expérimentaux adaptés à des essais mécaniques à haute température.

Ainsi, l'originalité de ces travaux est de combiner différentes techniques complémentaires (émission acoustique, réplique de bords, analyse fractographique, tomographie) qui permettent une analyse in-situ en temps réel des mécanismes d'endommagement qui coexistent et inter-agissent lors des différentes phases du chargement. En utilisant le protocole mis au point dans des conditions de température supérieure à la T_g du matériau, ces techniques apportent des informations pour quantifier et dissocier les différents comportements matériaux (viscoélasticité, viscoplasticité, endommagements) ainsi que des effets structures (rotation des fibres). Des analyses d'images basées sur des algorithmes de dilatation/érosion implémentées dans Matlab permettent d'évaluer la densité de fissuration (intra- et inter-torons) surfacique à partir des répliques de bords.

A l'échelle macroscopique, la réponse thermomécanique du C/PPS est peu influencée par les comportements visqueux du C/PSS que ce soit pour des stratifiés quasi-isotrope (comportement majoritairement piloté par les fibres à 0°) ou à plis orientés (comportement majoritairement piloté par la matrice PPS). Enfin, la rupture translaminaire ductile est caractérisée par l'évolution de l'énergie acoustique cumulée en fonction du taux de restitution d'énergie. L'instabilité de la rupture translaminaire ne permet pas d'évaluer l'influence des

effets visqueux sur la ténacité en mode I du matériau à l'initiation.

Aux échelles micro- et mésoscopiques, les résultats obtenus montrent clairement le visco-endommagement au sein de stratifiés C/PPS à plis orientés sollicités en fluage à $T > T_g$.

En mettant en oeuvre ce protocole, la pertinence/complémentarité démontrées de l'émission acoustique associée à la quantification de la densité de fissuration permettent d'envisager l'étude du couplage entre effets visqueux et endommagement au sein de stratifiés C/PPS soumis à des chargements à haute température. Cette problématique est essentielle du point de vue de la durabilité des structures composites dans un environnement moteur.

ABSTRACT

In fiber-reinforced polymer matrix composite materials, the coupling between viscous behaviour (viscoelasticity, viscoplasticity) and damage mechanisms is very little studied at the mesoscopic scale and is mainly limited to port-mortem analyses. For high-temperature aeronautical applications (*e.g.*, aircraft engine nacelle), the problem is even more complex within high performance thermoplastic matrix laminates PPS (Polyphenylene Sulfide) reinforced with carbon fiber fabrics. Indeed, these materials are characterized by matrix-rich zones whose viscous behaviors are exacerbated for service temperatures (*i.e.*, 120 °C) higher than the matrix glass transition temperature (about 95 °C).

It is therfore necessary to develop specific experimental procedures to highlight and quantify the viscous damage when the behaviour of C/PPS laminates is driven by the mechanical response of the matrix. In order to provide answers to this problem, one can evaluate : (1) the influence of the matrix viscosity on the translaminar fracture behaviour - (2) the time-dependent damage during creep-type loading. These two lines of study are based on the development of experimental protocols adapted to high temperature mechanical testing.

Thus, the originality of this work is to combine different complementary techniques (acoustic emission, edge replication, fractographic analysis, tomography) which allow in-situ and in real time analyses of the damage mechanisms that coexist and interact during the different loading phases. Using the protocol developed under conditions of temperature higher than the Tg of the material, these techniques provide information to quantify and dissociate the different material behaviours (viscoelasticity, viscoplasticity, damage) as well as structural effects (fibre rotation). Image analyses based on dilatation/erosion algorithms implemented in Matlab allow the evaluation of the surface cracking density (intra- and inter-strand) from edge replicas.

On a macroscopic scale, the thermomechanical response of C/PPS is little influenced by the viscous behaviour of C/PSS, whether for quasi-isotropic laminates (behaviour mainly driven by 0° fibres) or with oriented plies (behaviour mainly driven by the PPS matrix). Finally, the ductile translaminar fracture is characterized by the evolution of the cumulative acoustic energy as a function of the energy restitution rate. The instability of the translaminar fracture does not allow the quantification of the influence of viscous effects on the mode I toughness of the material at initiation.

At micro and mesoscopic scales, the results obtained clearly show time-dependent damage within oriented plies C/PPS laminates subjected to creep loadings at $T > T_g$.

By implementing this protocol, the demonstrated relevance/complementarity of the acoustic emission associated with the quantification of the cracking density allows the study of the coupling between viscous effects and damage within C/PPS laminates subjected to high temperature loading. This problem is essential from the point of view of the durability of composite structures in an engine environment.

TABLE OF CONTENTS

LIST OF TABLES

LIST OF FIGURES

LIST OF SYMBOLS AND ACRONYMS

5HS	5-harness satin weave
8HS	8-harness satin weave
AE	Acoustic Emission
AP	Angle-Ply
BMI	Bismaleimide
C	Carbon
CC	Cyclic Creep
CF	Carbon Fibre
CT	Compact Tension
DIC	Digital Image Correlation
DMA	Dynamic Mechanical Analysis
DSC	Differential Scanning Calorimetry
ECT	Extended Compact Tension
EPFM	Elastic-Plastic Fracture Mechanics
FPF	First-Ply-Failure
FPZ	Fracture Process Zone
FR	Felicity Ratio
HDT	Hit Definition Time
HLT	Hit Lockout Time
IR	Infrared
LcU	Load-Creep-Unload
LcUr	Load-Creep-Unload-Recovery
LEFM	Linear Elastic Fracture Mechanics
LLD	Load Line Displacement
LU	Load-Unload
PCA	Principal Component Analysis
PDF	Probability Distribution Function
PDT	Peak Definition Time
PEEK	PolyEtherEther-Ketone
PEKK	PolyEtherKetoneKetone
PMCs	Polymer Matrix Composites
PPS	PolyPhenylene Sulfide
QI	Quasi-Isotropic

RT	Room Temperature
SDZ	Singularity Dominated Zone
SEN/SENT	Single Edge Notched Tension
SERR	Strain Energy Release Rate
SIF	Stress Intensity Factor
SSY	Small Scale Yielding
TDD	Time-Dependent Damage
TID	Time-Independent Damage
TS	Thermoset
TP	Thermoplastic
UD	Unidirectional
UTS	Ultimate Tensile Strength
XμCT	X-ray computed micro-tomography

CHAPTER 1 INTRODUCTION

1.1 General context

For approximately 50 years, composite materials have been increasingly used in the aerospace industry thanks to their high specific mechanical properties and durability, when compared to metallic alloys. The use of composites in aircraft yields mass savings, hence reduces costs and CO_2 emissions [1, 2].

The use of textile reinforcements is attractive over conventional unidirectional (UD) ones for several reasons. The main advantage is their good compromise between their ease of manufacture and their cost [3]. Textile reinforcements can be produced at low cost using automated manufacturing techniques. Furthermore, textiles generally result in a better handling and drapability thanks to their higher structural stability, hence enabling the manufacturing of complex shapes, when compared to UD reinforcements. Finally, the interlacing of fibre bundles also improves damage tolerance, such as impact resistance (*i.e.*, smaller damage area and higher residual compression-after-impact strength than their cross-ply counterparts [4]).

Thermoset (TS)-based composites are the most widely used in the aerospace industry for primary structural components due to their high performance, relatively low price and processability. However, TP composites are increasingly considered for new applications due to several advantages and progresses in manufacturing processes of continuous fibre TP composites. Once polymerized, TPs can be softened or melted, which enables the use of other manufacturing processes, such as thermoforming. Thermoforming is a technique which enables high volume production due to short processing cycles. Furthermore, assembly techniques specific to TP composites (*e.g.*, thermal welding) promote their use. Improvements of the manufacturing of TP composites increased their quality and cost-competitiveness with respect to TS composites, considering the total cost of production. The nature of TPs also opens potential recycling and repair possibilities, which could lower the maintenance costs and is in line with the objectives of the European Commission. Indeed, The European Comission envisions cleaner aircraft, according to "European Aeronautics: a vision for 2020" [1] and "Flightpath 2050" [2]. Although TPs generally have lower mechanical properties than TSs, some high performances TPs (*i.e.*, PPS, PolyEtherEther-Ketone (PEEK), PolyEtherKetoneKetone (PEKK)) have mechanical properties approaching those of TSs and exhibit excellent fire and chemical resistance. Table 1.1 compares the advantages and disadvantages of TP and TS composites.

Table 1.1 Pros and Cons of TS and high performance TP composites in terms of processing and performance.

		TS (*e.g.*, epoxy)	TP (*e.g.*, PPS)
Processing	Shelf life	Limited	Unlimited
	Storage	Refrigeration	No refrigeration
	Processing T°C	Low	High
	Processing viscosity	Low	High
	Processing Time	Long	Short
	Assembly	Adhesive/Bolted	Welded/Adhesive/Bolted
	Processing cost	Relatively low	Overall processing cost generally higher
	Recycling	Under certain conditions	Possible
Performance	Glass transition temperature	Higher	Lower
	Moisture resistance	Lower	Excellent
	Fire resistance	Lower	Hardly flammable
	Impact resistance	Limited	Relatively good
	Fracture toughness	Limited	Better

1.2 Specific context

This work build on the works of Aucher [5] and Albouy [6]. The study of Aucher [5] was part of the project TOUPIE (maîTrise des cOmposites carbone/thermoplastique haUtes Performances pour pIèces de structurEs). Several industrial (Aircelle, AMPA) and academic (University Le Havre, INSA Rouen, ENSI Caen, MINES ParisTech) partners were involved. The main objective of this project was to investigate the feasibility of the stamping process (*i.e.*, a thermoforming process) for woven carbon fabric-reinforced high performance thermoplastics, to identify optimal process parameters and to characterize the mechanical performance of these composites. These composites were to be used in engine nacelles that are subjected to humidity and service temperatures around 120 °C. Two thermoplastic matrices were selected to meet the technical specifications: PPS ($T_g^{PPS} = 97.1\,°C$) and PEEK ($T_g^{PEEK} = 149.6\,°C$). A 5-harness satin weave (5HS) C fibre was chosen as the reinforcement. Aucher [5] compared consolidated (*i.e.*, hot-pressed but not stamped) 5HS C/PPS, C/PEEK and C/epoxy mechanical behaviours with and without a hygrothermal environment under several elementary mechanical solicitation (*e.g.*, tension, in-plane shear, compression, bending) or structural applications (bolted assembly, open-hole tensile test). This study underlined that C/epoxy

laminates were more sensitive to hygrothermal aging than C/TP laminates. Hygrothermal aging increased the ductility of the epoxy-based composites but it was still lower than those of the PPS- and PEEK-based laminates. Furthermore, it appeared that C/PPS laminates had inferior mechanical performance (*e.g.*, stiffness, ultimate strength in tension, compression and bending) than C/epoxy laminates, which is mainly due to their lower glass transition temperature (around 95 °C).

Albouy's work [6] compared the long term behaviour of consolidated $[(\pm 45)]_7$ and Quasi-isotropic (QI) 5HS C/PPS and C/epoxy laminates at 120 °C ($T_g^{C/PPS} < 120 < T_g^{C/epoxy}$). Firstly, the author studied the creep response of the $[(\pm 45)]_7$ laminates below a damage threshold (around 80 MPa). C/PPS specimens exhibited a more ductile behaviour, when compared to C/epoxy laminates due to the pronounced visco-elasto-plastic nature of PPS at 120 °C. Secondly, the behaviour of $[(\pm 45)]_7$ and QI C/PPS and C/epoxy laminates were investigated under fatigue solicitations. The test frequency did not have any influence on the fatigue life of $[(\pm 45)]_7$ C/PPS at 120 °C ($> T_g^{C/PPS}$), whereas an increase in frequency induced a decrease in fatigue life for C/epoxy at 120 °C $< T_g^{C/epoxy}$. Different mechanisms occurred during fatigue, depending on the matrix nature. Damage development (*e.g.*, fibre/matrix debonding, delamination) was the main mechanism in the C/epoxy case, whereas plastic deformation coming along with fibre bundle rotation seemed to prevail for the C/PPS laminates. It was concluded that the crack initiation threshold was delayed due to the plastic deformation of the PPS matrix, especially within matrix-rich regions, as illustrated in Figure 1.1. This delay in damage development in C/PPS due to the matrix plasticity was also observed in the matrix-rich areas close to 45°-plies in quasi-isotropic laminates. This delay explained the sudden failure of quasi-isotropic C/PPS specimens, in contrast with the progressive failure of QI C/epoxy laminates. Lastly, the influence of creep preloading on the fatigue behaviour of $[(\pm 45)]_7$ C/PPS laminates at 120 °C was also investigated. It appears that creep preloading significantly increases the fatigue life of those specimens, when the creep stages were long enough, or at a load level above the damage threshold (80 MPa). This was explained through plastic deformations and bundle reorientation that reduced stress concentration at the cracks tips.

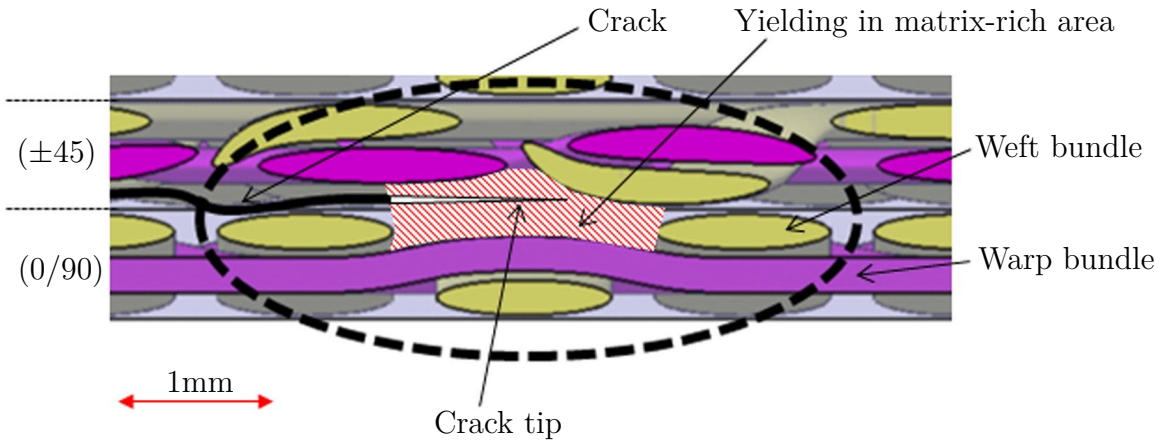

Figure 1.1 Illustration of the propagation of an inter-laminar crack within the mesostructure of a QI woven-ply laminate and possible interaction with a resin-rich area. Only two plies are represented: one (0/90) ply and one (±45) ply. The mesostructure of woven-ply laminates displays resin-rich regions that may delay damage propagation through crack blunting depending on the matrix' mechanical behaviour [6, 7].

1.3 Elements of the problem

Albouy's thesis [6] highlighted the influence of the matrix' ductility on the fatigue damage development within woven laminates. The author highlighted that matrix plasticity and time-dependent behaviour, especially in matrix-rich areas, may contribute to the delay of damage propagation within C/PPS laminates. However, several concurrent phenomena occurring in those laminates may directly or indirectly influence damage propagation, such as crack blunting, time-dependent behaviour (*i.e.*, visco-elasto-plasticity) especially when $\sigma_{mean} > 0$, structural effect (*e.g.*, fibre bundle rotation) and autogeneous heating that could reach $\Delta T = 84\,^{\circ}\mathrm{C}$.

Furthermore, Albouy studied and modeled the "undamaged" macroscopic visco-elasto-plastic behaviour of [(±45)] 5HS C/PPS laminates for stresses below 80 MPa, which is the damage threshold obtained using a stiffness-based damage variable. However, a lower damage threshold was highlighted at 35 MPa through Acoustic Emission (AE) monitoring [8]. Thus, Albouy did not explicitly take into account damage development and the possible effect of damage on the macroscopic behaviour of the laminate.

Those observations specifically questioned interactions between the matrix time-dependent behaviour and damage development within woven laminates, particularly in TP woven laminates subjected to mechanical loads at temperatures above their T_g. The matrix time-dependent behaviour could locally interact with damage accumulation (*e.g.*, near or within

matrix-rich areas) within [(±45)] or QI laminates, even though the macroscopic response of QI specimens seems time-independent.

1.4 Research objectives

By building on the works of Aucher [5] and Albouy [6], the principal objective of this thesis is to experimentally investigate the influence of the time-dependent mechanical behaviour on the damage development and failure of 5HS C/PPS laminates at 120 °C, which is above PPS glass transition temperature. The time-dependent behaviour of the PPS matrix is not investigated explicitly in this work. The time-dependent mechanical behaviour is observed through the laminates visco-elasto-plastic strain. The damage is mostly tracked at the mesoscopic and macroscopic scales in this study.

1.5 Thesis outline

The second chapter of this manuscript reviews the literature on this topic. Several themes and ideas are addressed in this literature review to approach the investigation of the interaction between time-dependent behaviour and damage within woven-ply laminates (*e.g.*, thermo-mechanical behaviour of woven composites, damage monitoring tools, fracture mechanics, etc.).

The third chapter analyses this literature review and presents the different objectives of this work.

The fourth chapter proposes a methodology to reach those objectives. It also details the experimental set-up.

The fifth chapter presents and discusses the part of the results based on a fracture mechanics approach. The investigation of a potential interaction between damage and time-dependent behaviour is done through the study of a translaminar macro-crack propagation within angle-ply and quasi-isotropic laminates under different loading conditions (*i.e.*, different loading rate, with or without creep and recovery stages). This chapter is published in Composites Part B [9].

The sixth chapter presents and discusses the results about the influence of time-dependent behaviour, by means of creep and recovery stages, on damage development within non-structural angle-ply specimens. Different techniques are used to monitor damage but also to detect time-dependent damage accumulation, as well as to decompose the different mechanisms occurring in those laminates.

The concluding chapter summarizes the important results and conclusions. Furthermore, specific improvements of the current experimental set-up and methodology are proposed. Finally, the different perspectives of this work are presented.

CHAPTER 2 LITERATURE REVIEW

2.1 Thermomechanical behaviour of woven composites

2.1.1 Composites constituents [10, 11]

2.1.1.1 Reinforcement - Carbon Fibre (CF)

CFs have good specific properties and good temperature resistance in non-oxidative environment. Figure 2.1 shows the Young's modulus and tensile strength at various temperatures for PAN-based and rayon-based fibres [12].

2.1.1.2 Matrix

Thermomechanical behaviour of TP polymers

The thermomechanical behaviour of a TP polymer is intrinsically dependent on its molecular structure. Indeed, mechanical properties depend on several parameters, such as the degree of crystallinity and molecular mass. Furthermore, the polymer's mechanical behaviour is temperature-dependent and several transitions can be observed as temperature increases. Figure 2.2 illustrates the changes in elastic behaviour, through the Young's modulus, with temperature for a semi-crystalline TP polymer. The different characteristic transitions/mechanisms observed for TP polymers are:

- secondary transitions (*e.g.*, β-relaxation, γ-relaxation, etc.), which correspond to local macromolecular conformation changes between two metastable positions without significant displacements of the gravity center of macromolecules within the amorphous phase. The stiffness remains relatively high and the amorphous phase is still in the glassy state.

- glass transition (T_g) and α-relaxation (T_α). Technically, T_g and T_α reflect the transition between the glassy state and the rubbery state, which results from the thermally activated displacements of the constitutional units in the amorphous phase. T_g represents the transition between two thermodynamic states of the amorphous phase, which are a metastable equilibrium fluid state and an out-of-thermodynamical equilibrium glassy state. T_α corresponds to the temperature at which the amorphous phase relaxation towards an equilibrium state is activated under solicitation. There is a significant drop in Young's modulus due to the amorphous phase mobility when the polymer is

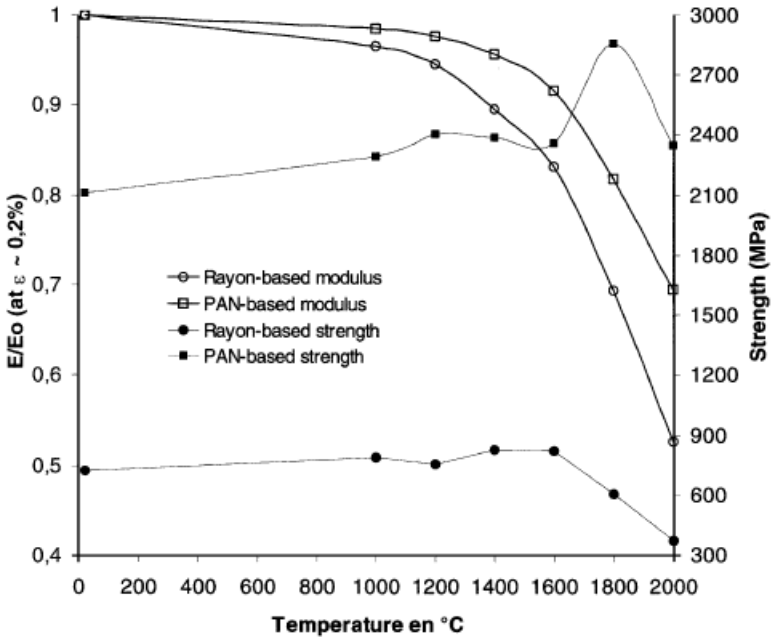

Figure 2.1 Variation of Young's modulus and tensile strength with temperature for two types of CFs. The mechanical properties is temperature-independent in the 0-1000 °C range [12].

heated up to T_g. Furthermore, the polymer's behaviour is highly viscoelastic during this transition.

- possible cold crystallization between T_g and T_m, which depends on the thermal history. The cold crystallization phenomenon can be observed by means of a Differential Scanning Calorimetry (DSC).

- melting (T_m), which corresponds to the destruction of the intermolecular bonds within the crystalline phase. Above T_m, the polymer has a viscous behaviour and is characterized by its viscosity.

- thermal decomposition (T_d) of the macromolecules.

Figure 2.3 illustrates the stress-strain behaviour of a semi-crystalline TP. At $T_g < T < T_m$, elastic strains mainly come from the reorientation of the macromolecules of the amorphous phase towards the stress direction, as shown in step 1. Crystalline phase has little elasticity due to its stiff nature at this temperature. At one point, a portion of the strain becomes irreversible (*i.e.*, plastic strains). These plastic strains come from the rotation and the shear-based separation of the crystalline lamellae (Steps 2 and 3). The amorphous phase and the crystalline lamellae continue to line up towards the stress direction and can form a fibrillar structure at the origin of crazing. Some of those crazes can break during further loading

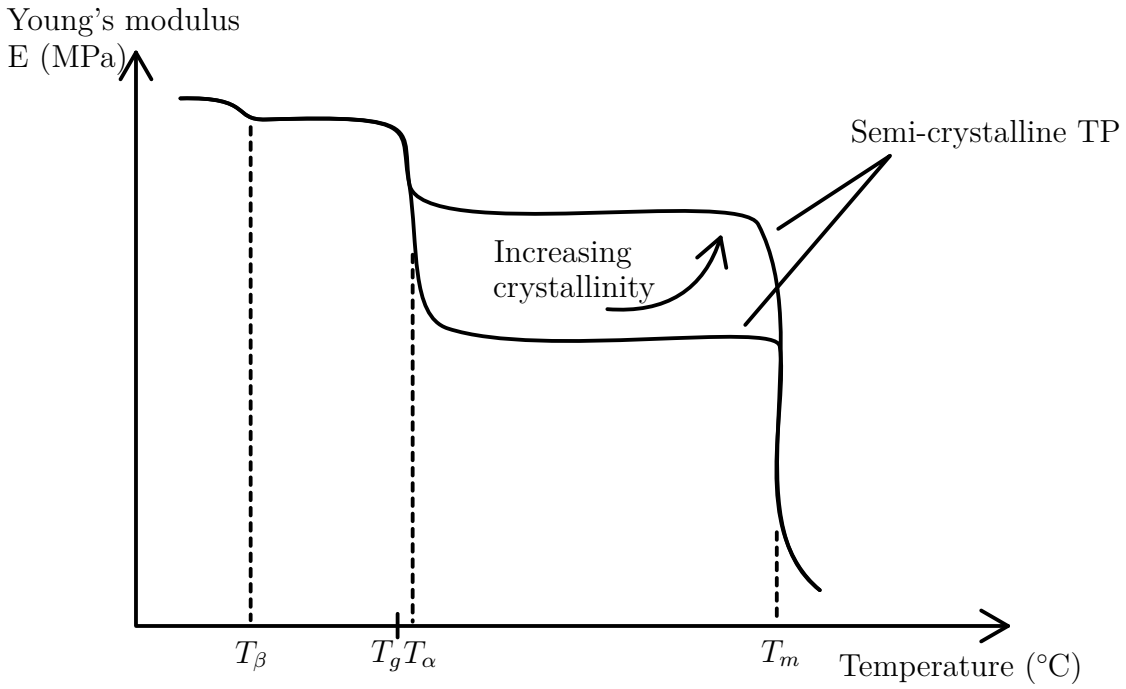

Figure 2.2 Illustration of the change in Young's modulus of a semi-crystalline TP as a function of temperature due to several transitions (inspired from [13]). Polymers generally display a brittle behaviour below T_g and ductile one above T_g. The polymers' behaviour is highly viscoelastic during this transition. Semi-crystalline TP polymers are characterized by several transition: secondary transitions (*e.g.*, β-relaxation), glass transition (T_g/T_α), melting (T_m) and thermal decomposition (T_d).

forming cracks (*i.e.*, damage). Here, plasticity refers to flow of macromolecules and possible crazing, whereas ductility is defined as the amount of strain that a material can withstand before ultimate failure.

Generally, the stiffness, the yield stress and the strength of polymers decrease with an increase of temperature, whereas the elongation at break increases. This is the case for the PPS matrix highlighted by Aucher [5]. This polymer is considered in this study and is further investigated.

Time-dependent behaviour of polymers

Most polymers exhibit a time-dependent mechanical behaviour for specific temperature and time ranges. This time-dependent behaviour corresponds to the aforementioned mechanisms related to the different relaxations. Two types of time-dependent behaviours can be observed depending on the reversibility of the phenomena involved: viscoelasticity and viscoplasticity. Several tests can be conducted to investigate such behaviours. The most common tests are

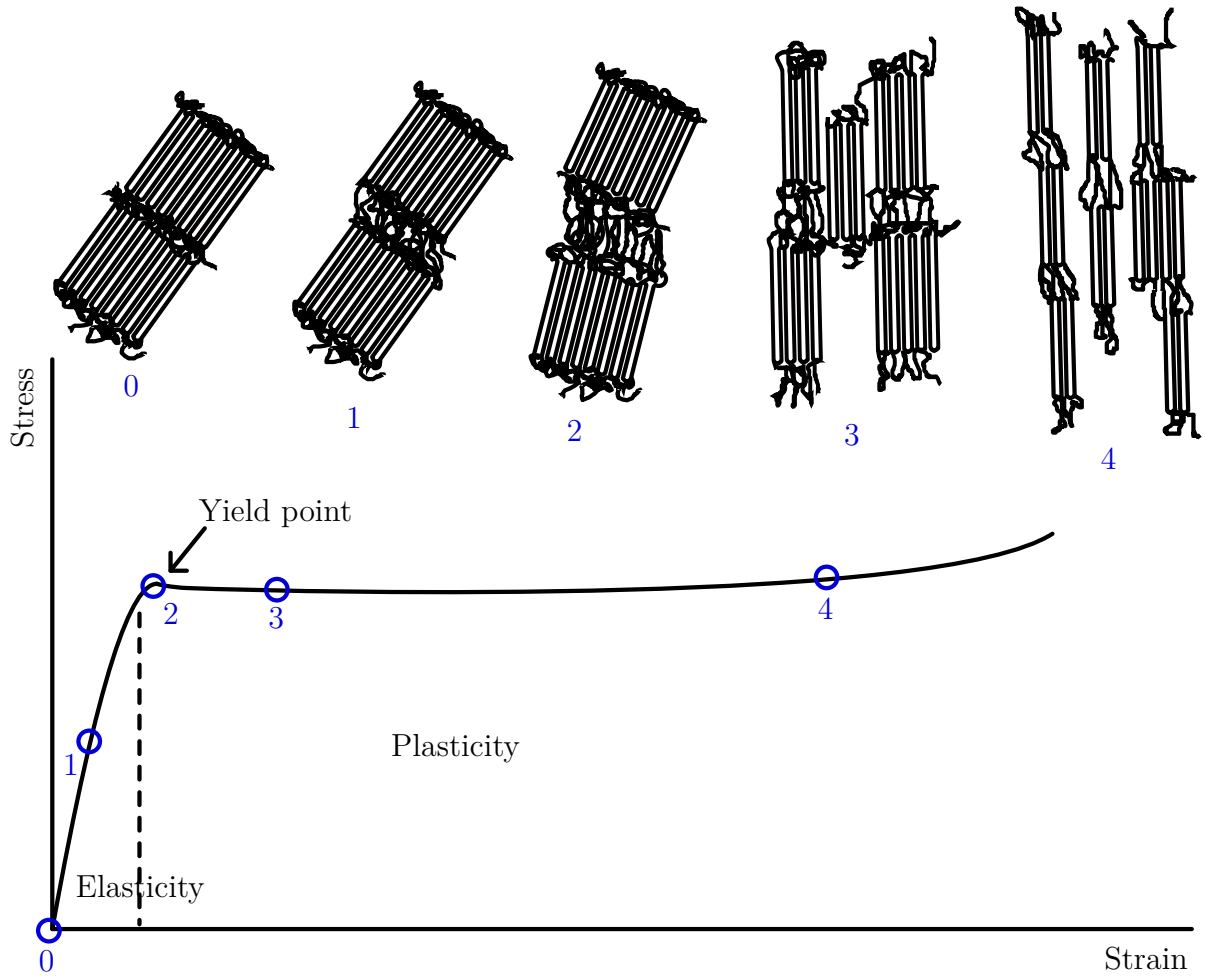

Figure 2.3 Illustration of the stress-strain behaviour of a semi-crystalline TP and the associated molecular mechanisms (inspired from [13]).

creep tests and relaxation tests. Figure 2.4a illustrates an idealized creep/recovery test (*i.e.*, instantaneous loading to creep stress σ_0 and instantaneous unloading to zero load), whereas Figures 2.4b, 2.4c and 2.4d represent the idealized responses of viscoelastic, elasto-viscoplastic (*i.e.*, elastic and viscoplastic) and visco-elasto-plastic (*i.e.*, viscoelastic and viscoplastic) materials.

The macroscopic phenomenological description of the viscoelasticity of materials focuses on the influence of time, loading rate, frequency and/or temperature on the mechanical behaviour. Viscoelasticity can be divided into two domains depending on the applied solicitation level:

- linear viscoelasticity can be assumed for low load levels. It is an "ideal" case and should satisfy the two following assumptions:

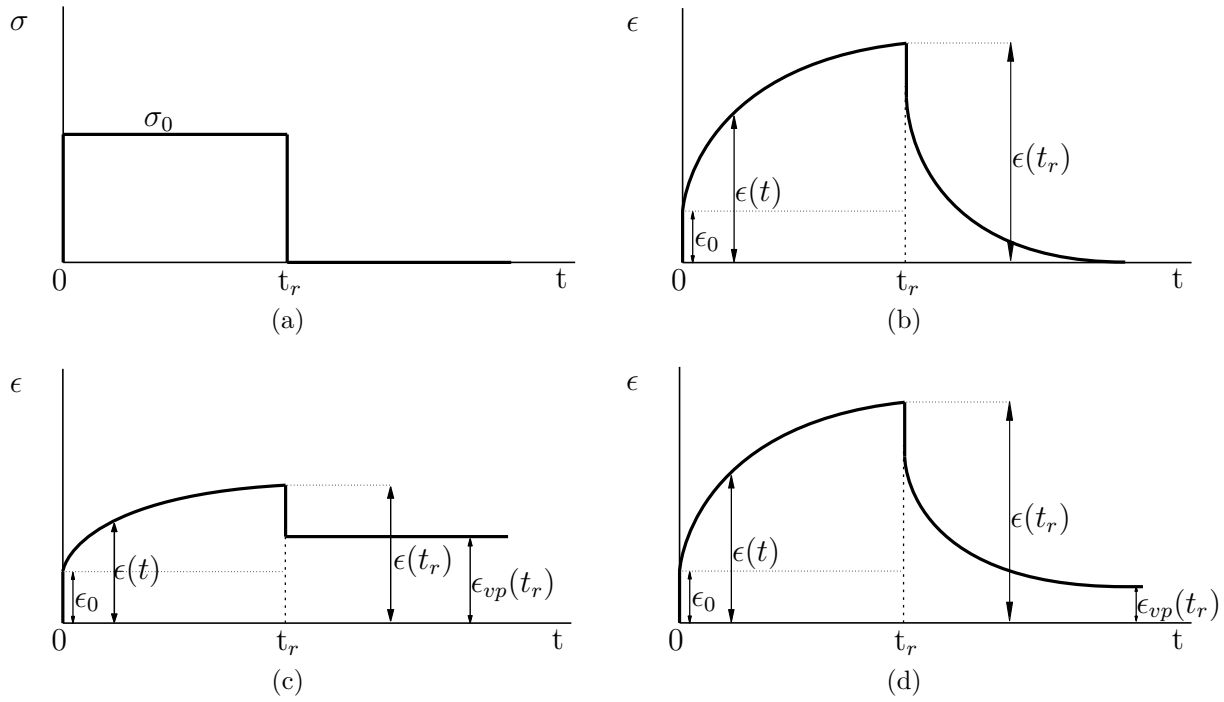

Figure 2.4 Illustrations of (a) an idealized creep/recovery test and the idealized responses of (b) viscoelastic, (c) elasto-viscoplastic and (d) visco-elasto-plastic materials. $\epsilon(t)$, ϵ_0 and $\epsilon_{vp}(t_r)$ are the total strain at time t, the instantaneous strain and the viscoplastic strain after time t_r.

- $\epsilon(\lambda\sigma) = \lambda\epsilon(\sigma))$ with $\lambda \in \mathbb{R}$, where ϵ is the strain and σ is the applied stress.
- $\epsilon(\sigma_1 + \sigma_2) = \epsilon(\sigma_1) + \epsilon(\sigma_2)$ (Boltzmann superposition principle)

Constitutive theories can be derived from thermodynamics' first and second laws. The strain can be written as,

$$\boldsymbol{\epsilon}(t) = \boldsymbol{S^{(0)}} : \boldsymbol{\sigma}(t) + \int_0^t \sum \boldsymbol{S^{(i)}}(1 - \exp[-\lambda_i(t-\tau)]) : \frac{\mathrm{d}\boldsymbol{\sigma}}{\mathrm{d}\tau}\mathrm{d}\tau \tag{2.1}$$

where $\boldsymbol{S^{(i)}}$ are the linearly viscoelastic creep compliance and are positive semi-definite, and $\lambda_i > 0$.

- nonlinear viscoelasticity when the two previous assumptions are no longer satisfied. The most commonly used constitutive equation for non-linear viscoelasticity was introduced by Schapery [14]. It can be written in its unidimensional form as follows:

$$\epsilon(t) = g_0(\sigma)S_0\sigma + g_1(\sigma)\int_0^t \Delta S(\Omega - \Omega')\frac{\mathrm{d}}{\mathrm{d}\tau}[g_2(\sigma)\sigma]\mathrm{d}\tau \tag{2.2}$$

with $\Omega' = \Omega(\tau)$. Ω is the reduced time and is defined by:

$$\Omega - \Omega' = \int_{\tau}^{t} \frac{\mathrm{d}\gamma}{g_3(\sigma(\gamma))} \tag{2.3}$$

where g_0, g_1, g_2 and g_3 (also noted a_σ) are stress-dependent material properties.

Contrary to viscoelastic strains, which are reversible, viscoplasticity induces time-dependent irreversible strains. The viscoplasticity describes the time-dependent material flow during creep, as well as the rate-dependent effects on transient loading [15]. The molecular mechanisms behind viscoplasticity in TPs are considered the same as the mechanisms behind plasticity, as detailed in Figure 2.3.

2.1.2 Macroscopic in-plane mechanical behaviour of woven composites

A woven-ply can be seen as an orthotropic homogeneous material at the macroscopic scale. The principal directions are the weft yarn, the warp yarn and the through-the-thickness directions.

2.1.2.1 Time-independent mechanical behaviour

The macroscopic mechanical behaviour of woven-ply laminates has been extensively investigated in the literature for TS-based [16–19] or TP-based [5,6,20,21] composites. It depends on several parameters such as the components' properties, the stacking sequences, the direction of solicitation, temperature, etc.

On-axis solicitation

The on-axis mechanical behaviour is generally elastic-brittle due to the dominating mechanical behaviour of carbon fibres resulting in a linear or quasi-linear stress-strain curve. A slight non-linearity in the stress-strain curve, characterized by a knee-point, may be observed during tensile loading [17, 18]. The inflection point is related to matrix cracking, which mainly occurs at crimp regions and is influenced by the weave pattern [17].

Off-axis solicitation

The off-axis mechanical behaviour is mainly controlled by the matrix and the fibre/matrix interface. Thus, the stress-strain curve generally reflects the matrix behaviour, which exhibits a more ductile behaviour, especially for TP-based laminates. Figure 2.5a [22] shows the stress-strain behaviour at different solicitation angles for a plain weave C/epoxy at Room

Temperature (RT). The larger the solicitation angle is, the more ductile the behaviour is. This is due to the fact that the matrix is more solicited as the solicitation angle increases.

By means of tensile tests on 45° oriented specimens, Daniel et al. [16] also highlighted that the in-plane shear behaviours of woven and UD composites are almost the same in the initial elastic region, but in the end the woven laminates show a much higher ductility than their UD counterparts. This non-linear behaviour is associated with matrix plasticity and cracking, even for low load levels.

Progressive rotation of the fibre bundles also occurs during off-axis tensile tests [18,19,21,23]. The early local damage and matrix plasticity in the crimp regions enable the fibre bundles rotation according to the solicitation direction, which commonly results in a secondary stiffening of the laminates (Figure 2.5b). This phenomenon comes along with the necking of the sample. Those nonlinear behaviours are especially pronounced in TP woven composites.

Influencing parameters

A varying contribution of the matrix on the laminates behaviour is observed depending on the solicitation direction. Therefore, any parameter influencing the matrix' mechanical properties will influence to a certain extent the mechanical behaviour of woven composites.

The effect of temperature on the behaviour of woven composites during off-axis loading is quite unanimous in the literature [5, 24, 25]. An increase in temperature generally results in an increase in strain to failure and a decrease in shear modulus, ultimate tensile strength and yield stress. For example, Figure 2.6a shows the influence of temperature on the stress-strain curves for $[(\pm 45)]_8$ 5HS C/epoxy and $[(\pm 45)]_7$ 5HS C/PPS laminates [5]. The effect is more pronounced for C/PPS in this case because 120 °C is above the glass transition of the PPS matrix.

The effect of temperature on the axial stiffness of woven composites during on-axis loading is relatively weak [5, 24, 25], when compared to off-axis loading. For example, the axial stiffness reduction of a QI C/PPS laminate is about 2.8% between RT and 120 °C, whereas the shear modulus loss of a C/PPS $[(0/90)]_7$ laminate is about 67% for the same temperature range [5]. However, a decrease in modulus can be observed in some cases due to thermally-induced cracks [25]. The strain to failure seems to be temperature-independent [5, 24, 25]. The tensile strength temperature-dependency is less obvious. Aucher [5] noted a decrease in strength between RT and 120 °C for QI 5HS C/epoxy and C/PPS specimens (Figure 2.6b), whereas Kawai et al. [24] observed an increase in strength between RT and 100 °C for plain C/epoxy laminates loaded in the warp and weft directions. Gupta and Raghavan [25] noted an increase in strength between RT and 80 °C followed by a decrease between 80 °C and

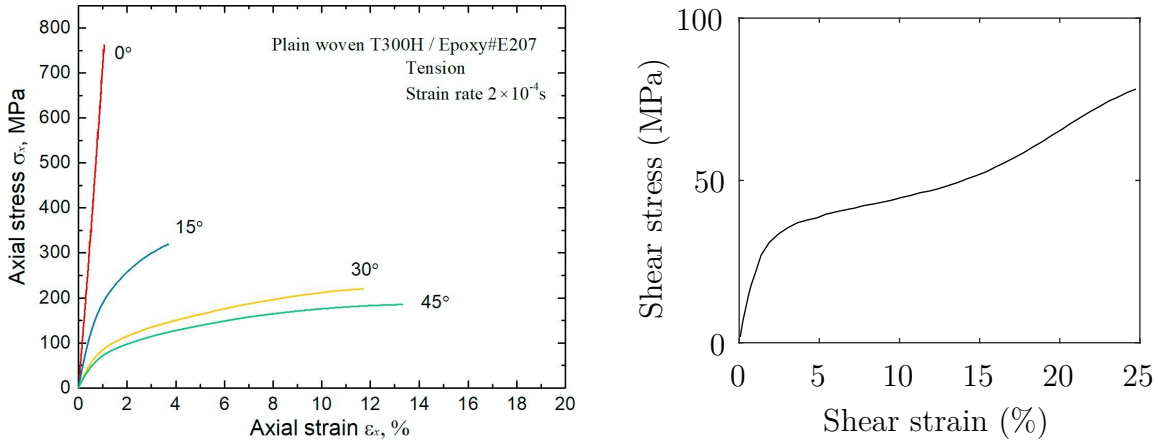

(a) (b)

Figure 2.5 Woven-ply composite's off-axis loading behaviour: (a) effect of solicitation angle for a plain weave C/epoxy laminate at RT [22] and (b) possible stiffening due to fibre bundle rotation during in-plane shear tests for a 5HS C/PPS composite at RT [21].

240 °C, which could be explained by the existence of thermally-induced cracks. However, the influence of temperature on on-axis mechanical behaviour of CF-based composites is relatively insignificant when compared to that of the off-axis mechanical behaviour due to the temperature resistance of CF, as summarized in Table 2.1.

The weave mesostructure also influences the time-independent macroscopic behaviour. Several authors noted that the crimp regions play a significant role on the on-axis stress-strain curves [17, 26], as illustrated in Figure 2.7. The fewer the interlacing points, the less manufacturing-induced fiber crimping, which reduces fiber straightening. The proportion of initially straight regions is larger in 8-harness satin weave (8HS) composites when compared to its 5HS counterparts, for example. Patterns with fewer crimping regions result in stiffer laminates with higher ultimate strengths.

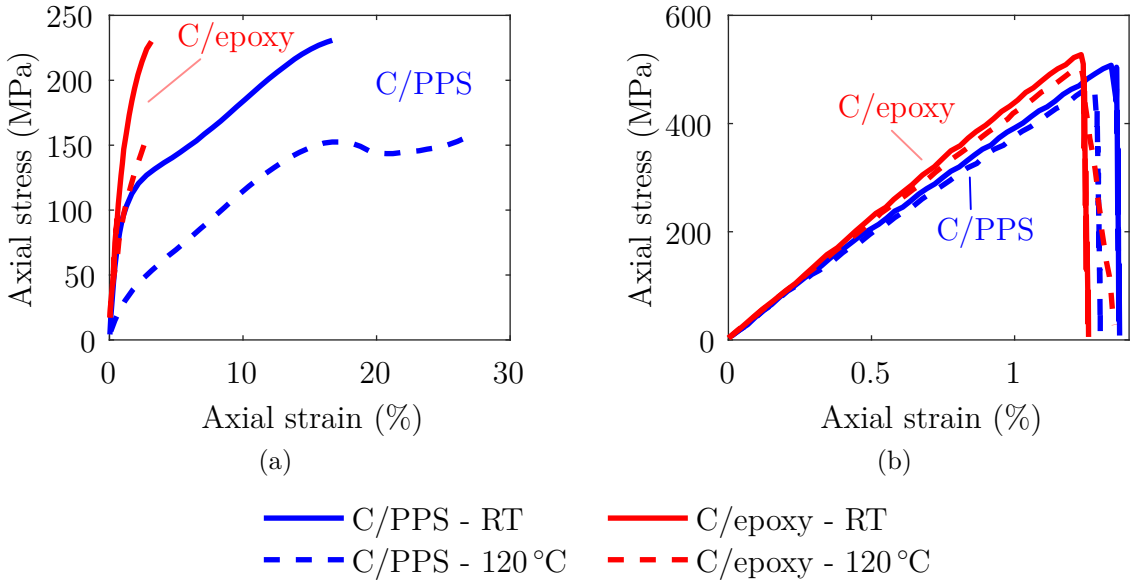

Figure 2.6 Influence of temperature on the (a) off-axis ([(±45)]) and (b) on-axis (here, QI) stress-strain curves for C/epoxy and C/PPS 5HS woven composites [5]. The on-axis mechanical behaviour is generally temperature-independent due the temperature-independent behaviour of the reinforcement, whereas the off-axis behaviour is significantly temperature-dependent because the temperature-dependent matrix is more loaded.

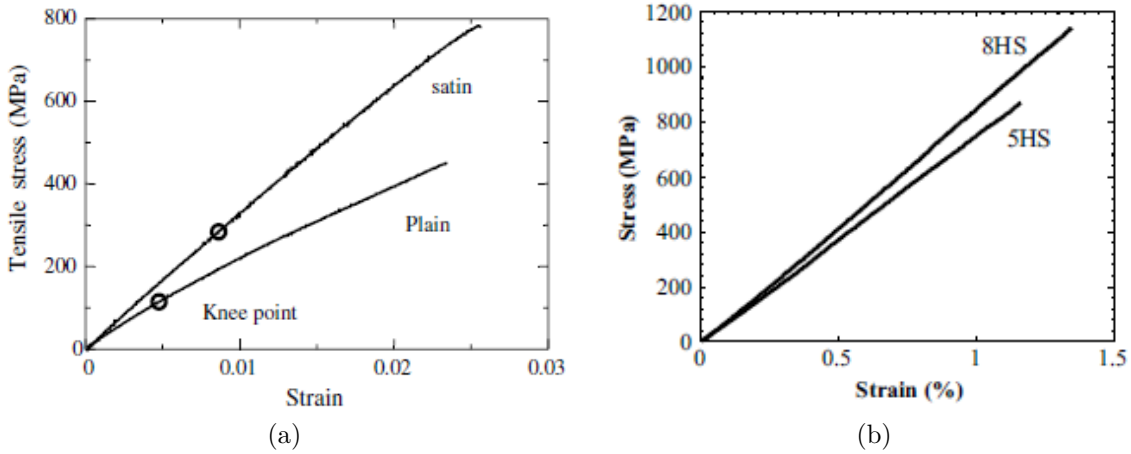

Figure 2.7 On-axis stress-strain curves for woven C/epoxy laminates with different weave patterns (a) [17] and (b) [26]. Less crimping regions results in a larger proportion of initially straight regions, which makes the laminate stiffer. Furthermore, higher ultimate strengths are observed for the weave patterns with less crimping regions.

Table 2.1 Variation of different mechanical properties with temperature for various woven-ply laminates. The influence of temperature on on-axis mechanical behaviour of CF-based composites is relatively insignificant when compared to the off-axis mechanical behaviour [5, 24, 25].

	T (°C)	25/RT	80	100	120	140	160	240
Plain C/epoxy [25]	E_{11} (GPa)	67.5	68.7	-	-	-	60.5	54.0
	σ_{11}^{u} (MPa)	634	775	-	-	-	680	600
	ϵ_{11}^{u} (%)	1.1	1.2	-	-	-	1.1	1.1
	$E_{11}^{45^\circ}$ (GPa)	26.20	19.91	17.14	16.32	12.50	7.60	-
	$\sigma_{11}^{u^{45^\circ}}$ (MPa)	224	211	182	180	155	103	-
	$\epsilon_{11}^{u^{45^\circ}}$ (%)	1.43	4.38	4.39	5.06	5.13	3.72	-
Plain C/epoxy [24]	E_{11} (GPa)	52.9	-	52.1	-	-	-	-
	E_{22} (GPa)	55.6	-	56.9	-	-	-	-
	σ_{11}^{u} (MPa)	599.5	-	637.2	-	-	-	-
	σ_{22}^{u} (MPa)	658.3	-	695.8	-	-	-	-
	G_{12} (GPa)	3.8	-	2.4	-	-	-	-
	τ_{12}^{u} (MPa)	112.0	-	76.1	-	-	-	-
5HS C/epoxy [5]	E_{11} (GPa)	45.22	-	-	43.29	-	-	-
	σ_{11}^{u} (GPa)	532	-	-	505	-	-	-
	ϵ_{11}^{u} (%)	1.23	-	-	1.23	-	-	-
	G_{12} (GPa)	5.29	-	-	4.19	-	-	-
	$\sigma_{11}^{u^{45^\circ}}$ (MPa)	232	-	-	165	-	-	-
	$\epsilon_{11}^{u^{45^\circ}}$ (%)	3.22	-	-	3.19	-	-	-
5HS C/PPS [5]	E_{11} (GPa)	41.95	-	-	40.29	-	-	-
	σ_{11}^{u} (GPa)	514	-	-	472	-	-	-
	ϵ_{11}^{u} (%)	1.35	-	-	1.28	-	-	-
	G_{12} (GPa)	4.08	-	-	1.35	-	-	-
	$\sigma_{11}^{u^{45^\circ}}$ (MPa)	231	-	-	159	-	-	-
	$\epsilon_{11}^{u^{45^\circ}}$ (%)	16.76	-	-	27.34	-	-	-

2.1.2.2 Time-dependent mechanical behaviour

It should be noted that C/epoxy woven composites are usually more prone to creep than their UD-ply counterparts [27]. This conclusion was also reached by Gupta and Raghavan [25] via simulations of creep tensile response of C/epoxy. Both studies explained this difference in creep behaviour through the presence of the crimp regions, which makes woven-ply specimens more compliant. The straightening of fibre bundles may also partially explained the creep response [27]. Gupta and Raghavan also considered that the matrix is more loaded in the crimp regions.

The time-dependent mechanical behaviours (*e.g.*, viscoelasticity and viscoplasticity) of woven composites depend on the same parameters than those influencing the time-independent mechanical behaviour (*e.g.*, geometry features, temperature, etc.).

Effect of the macro-geometry - Direction of solicitation

The stacking sequence and the loading direction influence greatly the time-dependent behaviour of woven-ply composites due to the contribution of the matrix time-dependent behaviour. For example, Gupta and Raghavan investigated experimentally the creep behaviour of $[(0/90)]_6$ and $[(\pm 45)]_6$ plain weave C/epoxy specimens solicited at 20% Ultimate Tensile Strength (UTS) [25]. The creep compliance increase was larger in the off-axis case (about 31%), when compared to the on-axis test (about 1%), as illustrated in Figure 2.8.

Effect of the micro- and meso-geometry

Gupta and Raghavan [28] performed a parametric study by performing simulations on the influence of crimp angle on the creep compliance of plain weave C/epoxy composites subjected to on-axis and off-axis loading. The variation of crimp angle was achieved though the variation of the laminae thickness and the undulation length, while the gap width, the unit cell length and the yarn cross-section were assumed to be constant. The authors highlighted a higher creep compliance and a higher creep rate, especially for higher creep times, with an increasing crimp angle ranging from 15.2° to 19.5°. Furthermore, a higher variation in the creep magnitude with crimp angle was underlined for on-axis loading, when compared to off-axis loading.

Layer nesting (*i.e.*, shift between adjacent woven plies) also seems to influence the laminates time-dependent behaviour. Matsuda et al. [29] used a elasto-visco-plastic model to show that nesting between plies affects the viscoplastic behaviour in comparison with the elastic behaviour observed during on-axis and off-axis solicitations.

Those studies highlighted the possible local variation of time-dependent behaviour due to

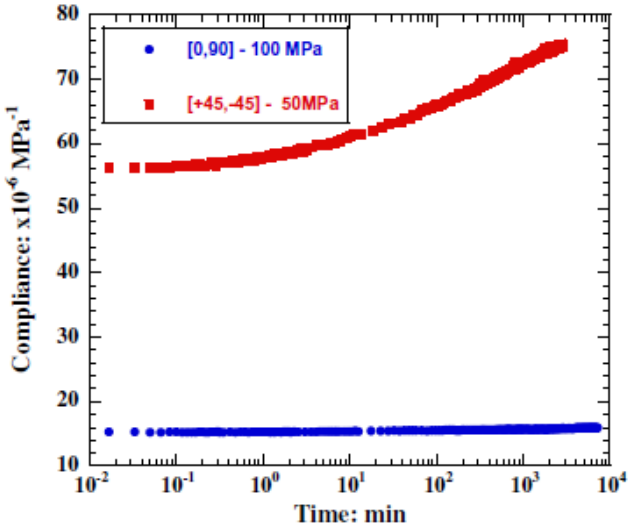

Figure 2.8 Experimental creep compliance of plain weave C/epoxy composites under on-axis (0°) loading and off-axis (45°) loading at 20% UTS and 80 °C [25]. Off-axis loading results in a higher creep compliance with a higher rate, when compared to on-axis loading due to the matrix' time-dependent behaviour.

local heterogeneity of the woven mesostructure.

Effect of temperature and stress level

Gupta and Raghavan [25] also noted that the creep compliance increased with increasing temperature and stress level for on- and off-axis specimens. However, this effect was significantly larger for the off-axis case, whose mechanical response is matrix-dominated.

Time-dependent behaviour of 5HS C/PPS laminates

The time-dependent mechanical behaviour of C/PPS woven laminates has been investigated by Bassery at RT [20] and by Albouy at 120 °C [6]. Bassery concluded that 7-plies 5HS C/PPS specimens solicited along the warp and weft directions have a time-independent behaviour, as illustrated in Figures 2.9a and 2.9b, which show the laminates stiffness for various strain rates [20]. This observation can be easily explained by the time-independent behaviour of carbon fibres, which are predominantly solicited. The fibre-dominated response also justifies the limited creep strain during creep in QI specimens solicited along the fibre bundles even at 80% UTS and 120 °C, as illustrated in Figure 2.10a [6]. The creep strain reached about 0.1% for a total strain of 1.05%, which is about 10% of the total strain. It should be noted that most of the creep strain seems irreversible.

In-plane shear testing of those laminates seems to point out a rate-dependent variation of

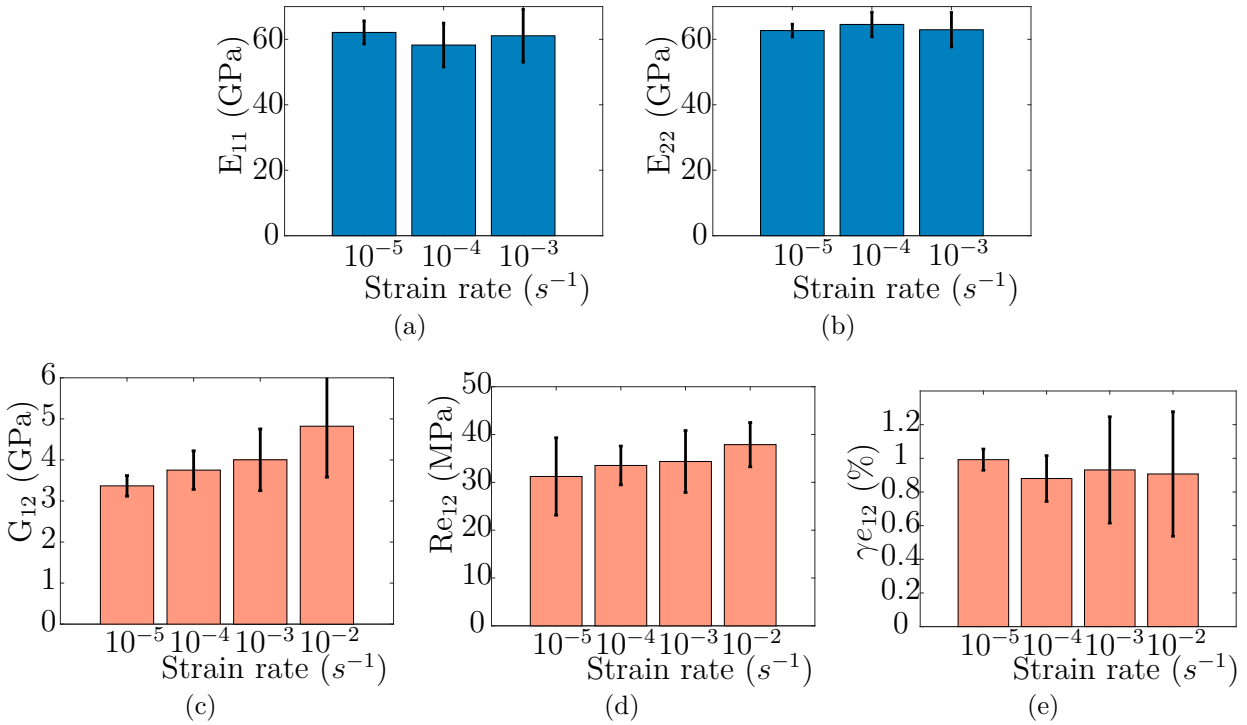

Figure 2.9 Evolution of (a) E_{11}, (b) E_{22}, (c) G_{12}, (e) shear stress at yield and (f) shear strain at yield as a function of strain rate for 5HS C/PPS laminates at RT. The shear properties were determined by means of in-plane shear tests [20]. The mean values of off-axis properties seem to be influenced by the strain rate, when compared to the strain rate-independent properties along the bundle fibre axes. However, the data dispersion is too high for those variations to be significant.

the mean values of several mechanical properties [20]. Figure 2.9c shows an increase in shear modulus with increasing strain rate. Furthermore, yield stress tends to increase with increasing strain rate (Figure 2.9d), whereas yield strain seems to decrease (Figure 2.9e). However, those variations are arguable according to the data dispersion and may not be significant. It should be noted that significant viscoelastic and viscoplastic creep strains are observed in $[(\pm 45)]_7$ laminates solicited at stress levels under a damage threshold of about 80 MPa, as illustrated in Figure 2.10b [6], and those creep strains are higher at 120 °C when compared to creep tests at RT [20]. In addition, the higher the stress level is, the higher the creep rate is. Those observations are consistent with the matrix-dominated mechanical behaviour of laminates subjected to off-axis loading.

Both authors simulated the time-dependent behaviour of $[(\pm 45)]_7$ 5HS C/PPS laminates. An elasto-visco-plastic model with non-linear isotropic hardening (Figure 2.11a) [20] or a visco-elasto-plastic model with a linear kinematic hardening and a non-linear viscoelasticity (Figure

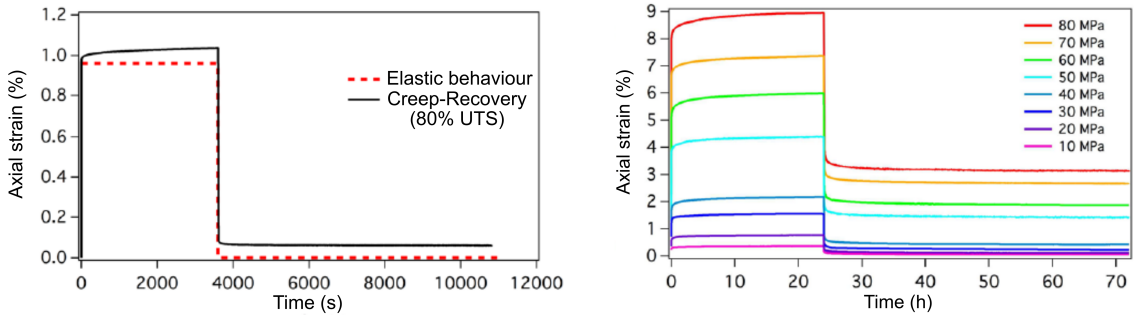

(a) (b)

Figure 2.10 Creep-recovery tests at 120 °C performed on (a) QI and (b) $[(\pm 45)]_7$ 5HS C/PPS laminates [6]. Little viscoplasticity can be observed for the QI specimens, whereas significant viscoelasticity and viscoplasticity are observed for $[(\pm 45)]_7$ laminates.

2.11b) [6] were considered. It appears that both models capability to predict viscoplasticity is relatively good, at least for the first cycles. However, the main difference between those two approaches is that only the visco-elasto-plasticity model enables the representation of the hysteresis cycles, especially the non-linearity during unloading.

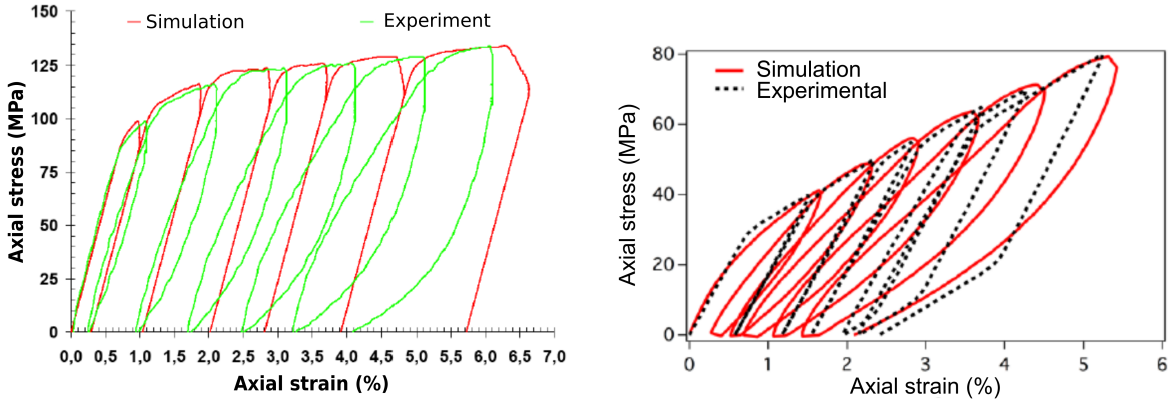

(a) (b)

Figure 2.11 Comparison between experiments and simulations of an incremental load-unload test on $[(\pm 45)]_7$ 5HS C/PPS laminates using (a) an elasto-viscoplastic model [20] and (b) a visco-elasto-plastic model [6]. The visco-elasto-plastic model enables a better representation of the mechanical behaviour.

2.2 Experimental damage monitoring tools

Different techniques have been developed to monitor damage development. These techniques can either be ex-situ or in-situ, destructive or nondestructive, qualitative or quantitative, implicit or explicit. This section presents several tools used for damage monitoring within composites, with a particular emphasis on woven laminates.

2.2.1 Implicit/indirect detection of damage - Damage variable

A way to detect damage and its propagation consists in following the evolution of specific material properties, which can also be used to define a damage variable. The most common properties are stiffness components [18, 20, 21, 30–33], but a few authors also used other properties, as the Poisson's ratio [31, 33] or the residual strain [21, 31]. Residual strains or other strain-based measurements (*e.g.*, mean strain for cyclic loading [6]) may not be suitable for materials characterized by significant plasticity and time-dependent behaviours.

Several authors noticed that the Poisson's ratio reductions with damage is much higher than the reduction in axial stiffness [31, 33]. For example, the overall stiffness reduction reaches 6% at most for two layers thin laminates, while the Poisson's ratio reduction reaches around 20-30% for thicker laminates consisting of (0/90) 8HS C/polyimide plies [31]. Doitrand also observed this trend for glass/epoxy plain weave specimens solicited along the warp and weft bundles [33]. It should be noted that stiffness seems to be a good damage indicator for off-axis loading. The stiffness reduction is about 20% when the specimens are solicited at $\pm 45°$ [33]. Figure 2.12 compares the Young's modulus loss (Figure 2.12a) and the Poisson's ratio reduction (Figure 2.12b) due to damage development as a function of the applied load for on-axis and off-axis loading. Significant stiffness reductions are also observed in $[(\pm 45)]_7$ 5HS C/PPS specimens mechanically loaded at RT (about 30%) [20] and at 120 °C (about 20%) [6]. Carnevale [21] noted that the stiffness reduction for 0° 5HS C/PPS laminates at RT is limited, but also depends on the fibre/matrix interface quality and resulting damage.

Gao et al. [31] also concluded that the residual strain is a good damage indicator, considering the changes in the strain as a release of curing stresses resulting from cracking.

2.2.2 Microscopic/visual observations

The most elementary techniques used for the characterization of damage in textile composites are visual observations. It can either be in-situ or ex-situ, non-destructive or destructive.

Cross-sectioning [8, 19, 34, 35] of specimens enables a good observation of the internal dam-

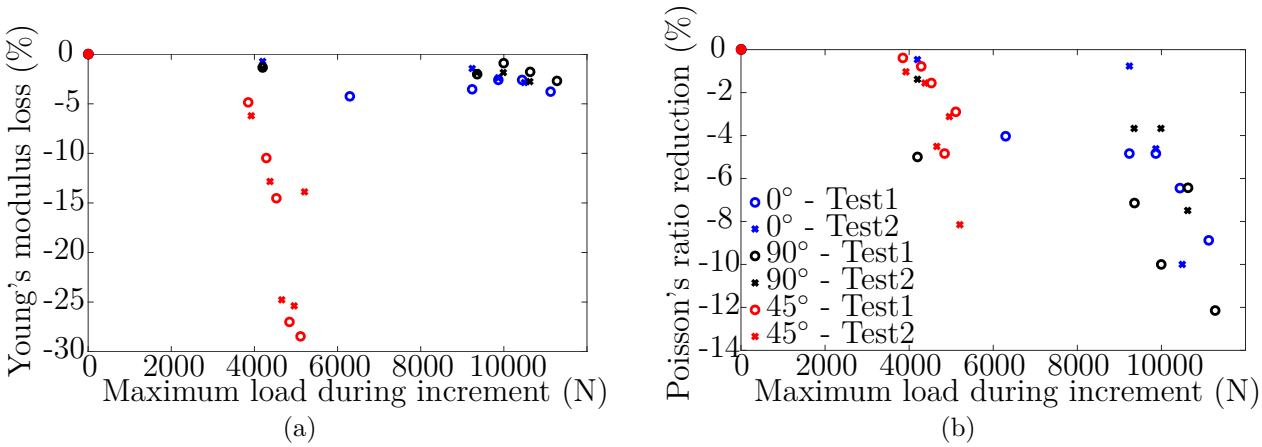

Figure 2.12 Variation of (a) Young's modulus and (b) Poisson's ratio during an incremental loading of plain weave glass/epoxy composites for various solicitation angle [33]. The Poisson's ratio reduction is more sensitive to damage development for on-axis solicitation, when compared to that observed for the Young's modulus. Both parameters are sensitive to damage development in the off-axis case.

age distribution. However, it is a destructive ex-situ technique that is time- and material-expensive to investigate the damage chronology.

The most widespread technique in visual detection of damage is the edge inspection. This method requires a prior polishing of the edge to be inspected. The observations can either be obtained directly from the specimen's edge [31, 33, 36] or from edge replicas [17, 35] using either replicating film or vinylpolysiloxane to create an imprint of the surface. These non-destructive in-situ techniques are generally used to characterize damage scenarios, *i.e.*, the damage mechanisms involved, their locations and their chronology. A problem may arise about the representativeness of the damage state at the edges of woven laminates, when compared to that occurring at the center of the specimens [31,33]. Gao et al. observed similar transverse cracking densities at the edge and at the center of 8HS C/polyimide laminates via cross-sectioning [31]. Doitrand observed by means of transmitted light microscopy that the damage distribution was quite homogeneous within [(0/90)] and [(±45)] glass/epoxy plain weave laminates, and thus concluded that the damage state on the edges was representative [33]. This conclusion was drawn mainly from the observation of transverse cracking, and thus the representativeness of the edges might not be valid for other damage mechanisms. Furthermore, no investigation has been carried out to verify if those cracks span the entire width of the specimens. Ivanov et al. considered that small cracks accumulate within yarns at the free edges of [(±45)] 5HS C/PPS and C/PEEK specimens, but do not propagate to the specimen's centre due to compressive stresses transverse to the yarns arising from bundle rotation [37]. However, this claim is not supported by experimental observations.

Another visual inspection technique is the transmitted light observation [30, 33, 38] based on a back-lighted system. However, this technique is only applicable to non-opaque materials. Therefore, this method is mainly used for glass fibre-reinforced plastics and not for CF-reinforced plastics. Another limitation is that this method does not provide information along the specimen's thickness.

2.2.3 Digital Image Correlation (DIC)

Full-field displacement and strain maps at specimens' surfaces can be obtained using DIC. Several authors deduced possible damage initiation regions within the woven mesostructure from strain localization revealed by DIC strain fields [21, 36]. However, this approach is only qualitative.

DIC can also be used as a quantitative tool. For example, Doitrand compared two DIC approaches to detect cracks on the edges of glass/epoxy plain weave laminates [33]. The first approach is based on local DIC and the resulting decorrelation map. The subsets containing a cracks should not be correlated with any initial subsets resulting in a decorrelation map. However, possible false positives were detected and the detected regions were larger than the actual cracks. The second approach is based on global DIC with a mechanical regularisation and results in a finer detection. This approach results in a finer crack detection.

2.2.4 Infrared (IR) thermography

IR thermography is a way to monitor specimens' surface temperature fields. Thus, it enables the monitoring of heat sources fields associated with dissipative phenomena like cracking. The volume heat sources $\bar{\omega}_{hs}(x, y, t)$ are directly linked to the surface temperature variation through the 2D local heat diffusion equation [39]. Therefore, IR thermography is a powerful damage localization tool. Furthermore, it is possible to estimate the strain energy release rates from experimental heat sources [39, 40]. The use of IR thermography is quite recent in woven laminates [26, 39–41]. This technique was applied to follow damage via the dissipated energy-based damage variable [41], to localize microscopic cracks [26, 39] (Figure 2.13a) and to track the crack length during fracture toughness tests [40] (Figure 2.13b).

2.2.5 X-ray-based techniques

Several authors used X-ray radiography to characterize damage mechanisms within textile composites [30, 31, 34, 42, 43]. However, this technique only gives 2D information about the damage state.

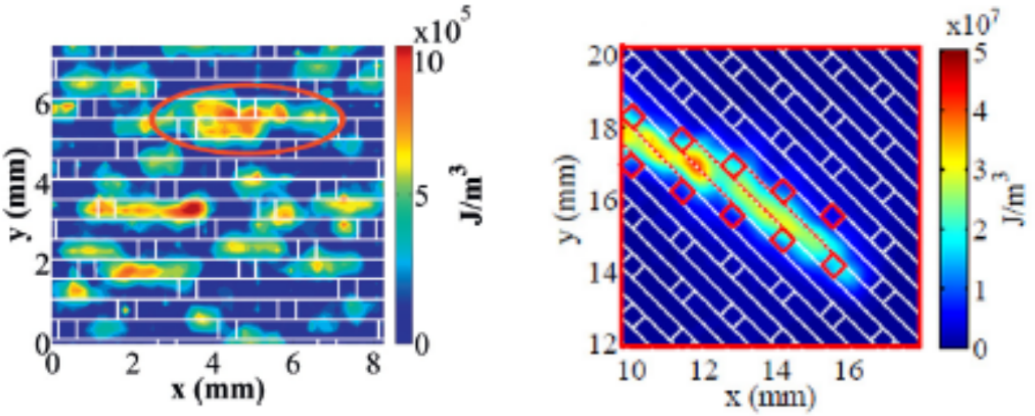

(a) (b)

Figure 2.13 Total cumulative volume energy (*i.e*, temporal accumulation of experimental heat sources $\bar{\omega}_{hs}(x, y, t)$) cartographies enabling (a) damage dectection [39] and (b) crack tip localization [40] in 8HS glass/epoxy laminates. The axes are the Cartesian coordinate system. The white lines represent the woven mesostructure at the specimens' surface. These cartographies depict the cumulative volume energy fields associated with dissipative phenomena like cracking enabling the characterization of damage distribution.

X-ray computed micro-tomography (XμCT) is the ideal solution to obtain the 3D distribution of damage state within a specimen and can be used either ex-situ [44,45] or in-situ [45]. Böhm et al. [45] noticed that the extent of damage was underestimated through ex-situ XμCT, when compared to under load in-situ XμCT.

2.2.6 Acoustic emission

2.2.6.1 General information [46]

Acoustic Emission is "the class of phenomena whereby transient stress/displacement waves are generated by the rapid release of energy from localized sources within a material, or the transient waves so generate" according to the ASTM standard E1316-18a. Figure 2.14 illustrates the AE monitoring system. A damage source (*e.g.*, crack initiation or propagation) occurs within the specimen producing an elastic wave that propagates within the material before reaching the material's surface. The wave is then detected by a piezoelectric sensor, amplified and monitored by a data acquisition system. Damage sources generally result in discrete AE signals (also called bursts/hits) in contrast to continuous AE monitoring. It should be noted that AE monitoring is a nondestructive technique that only detects active flaws (*e.g.*, propagating cracks).

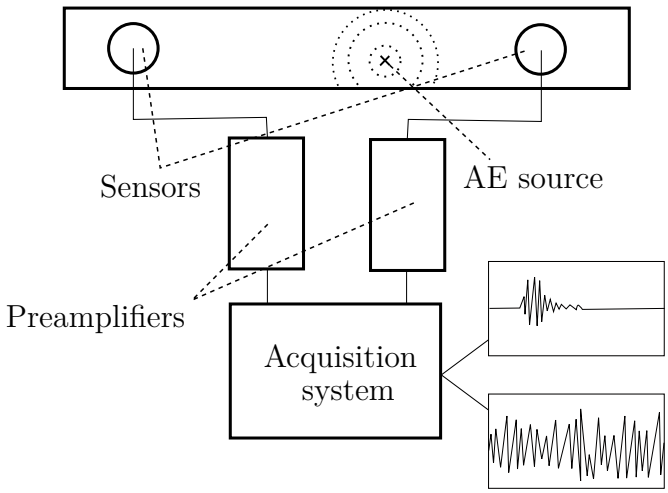

Figure 2.14 Illustration of the AE acquisition setup. A source (*e.g.*, friction, crack propagation, etc.) generates an elastic wave that propagates within the specimen. This elastic wave is detected by a piezoelectric sensor, then amplified by a pre-amplifier before reaching the acquisition card. Finally, several filters can be added during acquisition (inspired from [47]).

Several physical mechanisms can generate AE signals in composites: plastic deformation, damage initiation/propagation, friction, leakage, noise, etc. AE source mechanisms can be subdivided into several groups depending on:

- their nature: material, *e.g.* cracking, plasticity, or mechanical, *e.g.* friction;
- their scale;
- their importance/effect: primary or secondary.

These various sources can generate waves with different AE signatures, *i.e.* with specific temporal and frequency features (Section 2.2.6.2), depending on the source mechanism. Those AE waves are altered before reaching the sensor's surface due to their propagation throughout the material. AE wave attenuation occurs due to several phenomena that are function of the propagation distance (*e.g.*, absorption, scattering diffraction, geometric spreading). AE wave propagation depends on the material properties, and thus depends on the temperature and the damage state [48, 49]. Furthermore, those AE waves are also altered by the sensor and acquisition system characteristics. The monitored AE signals are complex signals resulting from:

- physical and geometric characteristics of the source mechanism,
- propagation medium,

- sensors and acquisition system characteristics.

There are mainly two types of sensors, resonant (*i.e.*, narrowband) and wideband. The resonant sensors have one or more dominant frequency peaks which tends to deform the incoming wave in comparison to wideband sensors. They are, however, generally more sensitive and smaller, therefore more adaptable. Wideband sensors are well suited for modal and frequency analyses, whereas resonant ones are used for more conventional analyses or analyses based on time domain features. The preamplifier's role is to amplify the signal to increase the signal-to-noise ratio. Its gain generally varies between 20, 40 and 60 dB. The preamplifier is also a pass-band filter. The acquisition system manages the configuration of acquisition parameters, signal digitization, signal descriptor extraction, graph visualization and data storage.

2.2.6.2 AE data

Waveform features [50]
Burst emission signals are characterized by waveforms (Figure 2.15) that can be defined by several parameters/features, also called descriptors. These descriptors are calculated either from the time or spectral domains. The main parameters are:

- amplitude A (dB_{AE} or dB): based on the highest voltage in the AE waveform before amplification. $A = 20\log_{10}(V_{max}/1\mu V) - dB_{preamp}$, where V_{max} is the highest voltage of the monitored signal (*i.e.*, after preamplification) and dB_{preamp} is the preamplifiers gain.

- duration d (µs): time between first and last threshold crossing.

- rise time RT (µs): time from first threshold crossing to highest voltage point.

- counts n: number of threshold crossing.

- counts to peak n_{RT}: number of threshold crossing during rise time.

- energy (µV s/count): derived from the integral of the rectified voltage signal over the duration of the AE hit.

- absolute energy E (aJ): time integral of the square of the signal voltage at the sensor before any amplification divided by the reference resistance (10 kΩ).

- average frequency F (kHz): this feature is not a true spectral parameter and is calculated from time domain feature, $F = n/d$.

- reverberation frequency F_{rev} (kHz): this feature is not a true spectral parameter and is calculated from time domain feature, $F_{rev} = (n - n_{RT})/(d - RT)$.

- initiation frequency F_{ini} (kHz): his feature is not a true spectral parameter and is calculated from time domain feature, $F_{ini} = n_{RT}/RT$.

- frequency centroid F_c (kHz): center of mass of the power spectrum.

- peak frequency F_p (kHz): frequency at the highest point of the power spectrum.

Other AE features can be calculated from the previous ones, such as rise angle, fall angle, relative energy, etc. [51].

AE source localisation

AE source localisation is possible based on arrival times if a wave generated by a source mechanism reaches several sensors. The wave's velocity within the specimen should be known beforehand. AE hits from different sensors can result in an AE event, *i.e.* a located AE source. Therefore, spatial filtering can be achieved using several AE sensors enabling to remove AE activity outside the region of interest. Different spatial configurations (*e.g.* linear, planar, etc.) are possible to locate AE events either in 1D, 2D or 3D. It should be noted that AE wave's velocity depends on the propagation medium, therefore it also depends on the damage state [48]. A few authors take this dependence of the wave's velocity on damage state into account during AE source localisation [52, 53].

Kaiser and Felicity effects

The Kaiser effect implies that no significant AE activity should be detected within a specimen at lower load levels than that was previously exerted on it, as illustrated in Figure 2.16. The Kaiser effect can be seen as an irreversible assumption of AE sources, *e.g.* cracks initiated in a material do not propagate before reaching the previous maximum load. This effect is well verified for metallic materials. However, AE activity can resume at lower load than that previously reached, especially for fibre reinforced composites. This phenomenon is quantified using the Felicity Ratio (FR):

$$FR = \frac{F_2^{AE}}{F_1^m} \tag{2.4}$$

where

F_1^m is the previously highest reached load.

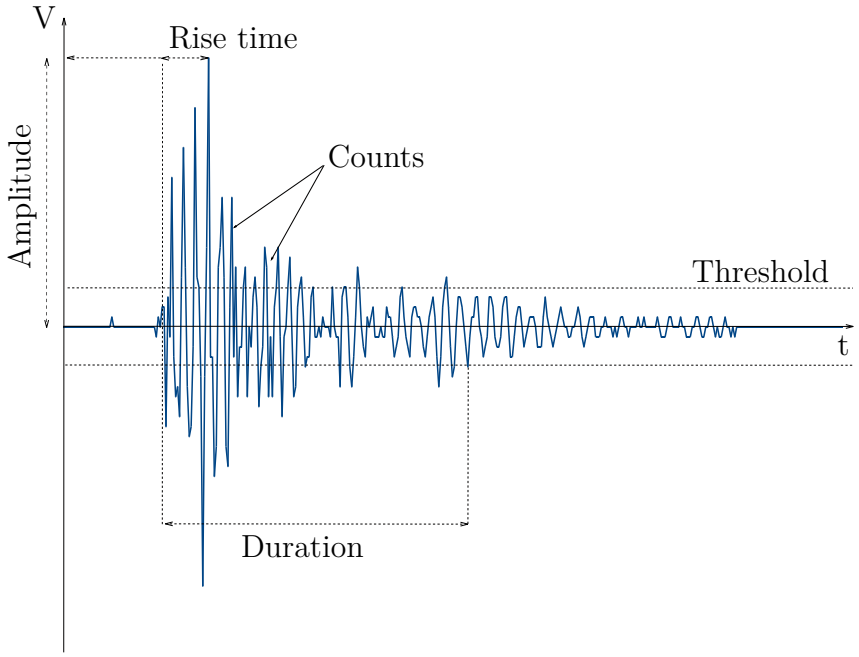

Figure 2.15 An AE waveform is characterized by several acquisition-dependent features, *i.e.* amplitude, duration, counts, rise time, energy and frequencies.

F_2^{AE} is the load when AE activity resumes.

FR can be used as an indicator to detect damage development. Generally, a FR lower than 1 can be observed for damaged structures [47] and a continuous decrease in FR with increased loading is interpreted as an indication of growing damage [46].

AE analysis for damage monitoring

AE data can be analyzed in many ways. The study of AE activity (*e.g.*, cumulative AE events or cumulative AE energy as a function of time/stress/strain) highlights information about damage development and its chronology. The AE events localization, either 1D, 2D or 3D, enables the detection of damaged regions or the tracking of a macro-crack tip. Furthermore, AE monitoring can discriminate different damage mechanisms based on the waves' signatures. This clustering between AE sources can either be done via an elementary statistic approach based on the distribution of one or two AE temporal (*e.g.*, amplitude [54–56]) or frequency features [57] (*e.g.*, peak frequency or frequency centroid), or via a multivariate statistical analysis using clustering algorithms [8, 38, 58–62]. The approach using one or two features is quickly limited. Indeed, this method correctly works only if the features' distribution are multimodal. In addition, there are generally overlaps of a specific feature's distribution (*e.g.*, amplitude) between two different damage mechanisms, as illustrated in Figure 2.17 [47].

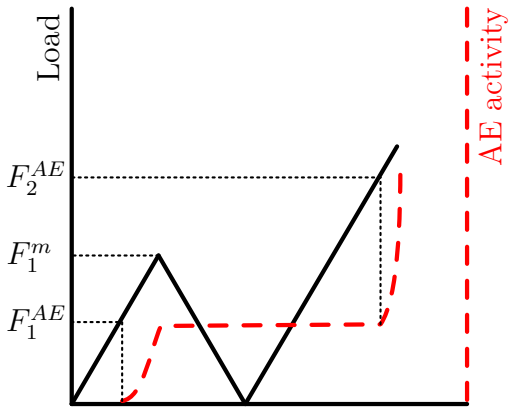

Figure 2.16 Illustration of the Kaiser effect (*i.e.*, AE activity does not resume before the applied stress exceeds the previous stress reached). The violation of the Kaiser effect can be used as a damage indicator in composite materials.

Therefore, the multivariate approach based on clustering algorithms is generally preferred. It should be recalled that AE waves are altered during propagation. Several factors alter the AE signature (*i.e.*, the monitored waveform and correspondant AE features): material properties, distance source-sensor, specimen geometry, sensor, acquisition set-up, etc. Therefore, there is a relatively high dispersion in clustering between different studies in the literature, even for the same damage mechanisms. Most of the classifications of AE events is based on several hypotheses [52, 63]:

- Two distinct damage mechanisms result in distinct energy release. Thus, the associated AE signals are different.
- AE signals are affected by propagation, but they remain distinguishable images of the sources.
- AE signatures do not significantly change during propagation and damage development.

2.2.6.3 AE application for C/PPS woven laminates

A few authors used AE monitoring to get a better insight about damage development within 5HS C/PPS laminates either loaded along the warp direction [36, 37, 62] or in the 45° direction [8, 37]. All of the mentioned authors at least used AE activity to detect damage initiation and other critical point during tensile tests. The analysis method used in [36, 37, 62] are related to a work done by Lomov et al. [64] which used the cumulative AE energy to determine three strain thresholds. Daggumati et al. [36] observed that AE initiation,

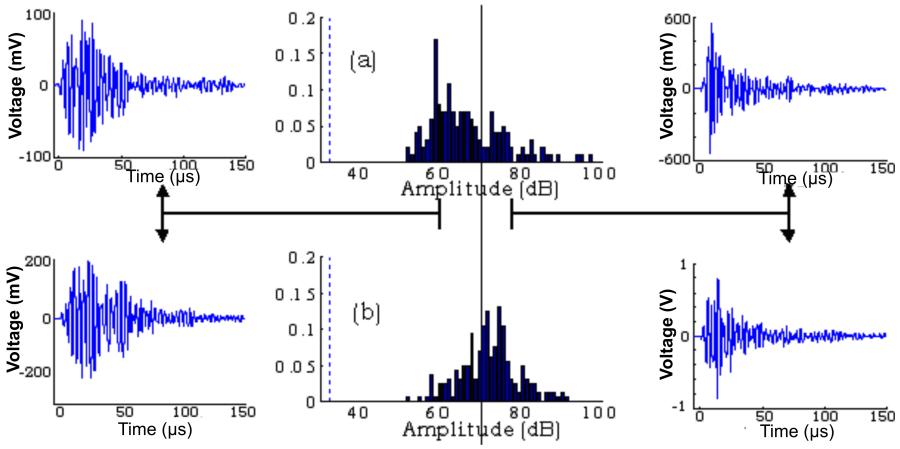

Figure 2.17 Amplitude distributions of AE signals monitored in UD C/polyester composites solicited (a) along the transverse direction and (b) at 45° with respect to fibres [47]. The AE signals on the left represent matrix cracking, whereas those on the right correspond to interfacial damage. An overlap of the amplitude distributions of different damage mechanisms was highlighted in [47]. Discrimination of damage mechanisms with only one AE feature is generally limited.

which reflects damage initiation, is significantly influenced by process-induced variation (*i.e.*, manufacturing-induced inhomogeneities such as fibre spacing, intra-bundle volume fraction and nesting). This threshold is around 0.09-0.2% and is related to sparse cracks with low energies. The next threshold (0.3-0.35%) corresponds to an increase in AE energy with low and middle energy AE events. Finally, the last threshold (0.4-0.45%) is related to critical damage propagation and specimen failure, which generates a continuous activity with high energy AE events. Carvelli et al. [62] underlines that the different AE thresholds are significantly lower than those from [36] and the difference can be explained by the different fibre volume fraction between those two studies. Ivanov et al. [37] compared the cumulative AE energy for 5HS C/PPS laminates solicited in the warp and 45° directions. The cumulative AE energy curves show a saturation in the studied strain range (0-4%) in the 45° direction, whereas no saturation is observed for both cumulative AE energies and crack densities within the studied strain range (0-1%) in the warp direction. Furthermore, they observed that the increase in crack density in weft yarns and the cumulative AE energy followed the same tendency in the case of a solicitation along the warp direction. Carvelli et al. [62] went further through a classification of monitored AE events using a Principal Component Analysis (PCA) followed by the k-means++ algorithm. Four AE features were chosen: amplitude, peak frequency, frequency centroid and rise time divided by amplitude. A good correlation was found between the AE events of one of the classes and transverse cracking within weft bundles, as illustrated in Figure 2.18. Albouy and Vieille [8] compared the damage initiation threshold

detected through AE initiation with that identified from the axial stiffness loss. It appears that the latter was far greater (about 80 MPa) than the first one (about 35 MPa).

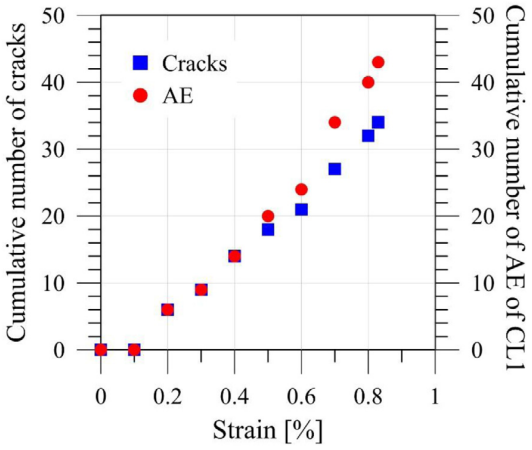

Figure 2.18 Comparison of the cumulative AE events associated with intra-bundle cracking (cluster 1) and the cumulative number of intra-bundle cracks as a function of strain in a 5 mm central portion within 5HS C/PPS laminates at RT [62]. The AE events were obtained after a k-means++ algorithm, whereas the number of intra-bundle cracks were monitored through edge observations. A very good correlation can be observed between AE events and intra-bundle cracks.

2.2.7 Comparison of the different damage monitoring tools

Table 2.2 summarizes the different characteristics (*i.e.*, in-situ/ex-situ, real-time monitoring, resolution, etc.) and purposes of several monitoring tools, as well as the different damage mechanisms that can be detected by each technique.

Most of the presented techniques are non-destructive and can be used in-situ, except cross-sectioning. However, only a few enables real-time damage monitoring, such as AE, DIC and IR thermography. Others techniques, such as XμCT, edge and transmission observations, can rather be seen as "incremental real-time" monitoring. The monitoring tools enabling a finer direct damage characterization (*e.g.*, damage localisation, quantification and chronology) are the different visual techniques and XμCT. Only XμCT and AE give volume information about damage, whereas the other tools result in surface information. The use of a damage variable is great to know if damage influence the material's mechanical behaviour, however it does not enable the differentiation of damage mechanisms. Concerning visual observations, cross-sectioning enables a better damage characterization through damage spatial distribution within the laminates, but it is material-consuming. Transmitted light observations are limited to non-opaque material. Edge observations are great for in-situ monitoring, however a strong assumption is made about the damage state representativeness at the edges.

The most versatile techniques seem to be XμCT, AE, DIC, IR thermography and edge observations. The AE technique seems to be the most complete real-time monitoring tool to track damage thanks to its volume information. However, the interpretation of AE data can be challenging and the damage localisation is less accurate, when compared to DIC or IR thermography. Furthermore, AE generally needs an additional monitoring tool in order to differentiate and to classify the AE sources. XμCT and edge observations are great monitoring tools to be coupled with AE to help with the interpretation of AE data.

Table 2.2 Pros and cons of different damage monitoring techniques.

	Damage variable	Visual observation Cross-sectioning	Visual observation Edge	DIC	IR	XμCT	AE
In-situ/Ex-situ	In-situ	Ex-situ	Both	In-situ	In-situ	Both	In-situ
NDT/DT[1]	NDT	DT	NDT	NDT	NDT	NDT	NDT
Passive[2]/active flaws	Active	Passive	Both	Active	Active	Both	Active
Real-time	No	No	No	Yes	Yes	No	Yes
Damage phenomenology	Hard	Expensive	Yes	Yes	Yes	Yes	Yes
Damage localisation	No	Yes	Yes	Yes	Yes	Yes	Yes
Damage quantification	No	Yes	Yes	Possible	Challenging	Yes	Challenging
Data dimensions	"2D"	2D	2D	2D	2D	3D	3D
Resolution	/	Micro	Micro	Micro/Meso	Micro/Meso	Micro	Micro
Main objectives as a damage monitoring tool	Effect of damage	Distribution	Chronology	Localisation	Localisation	Distribution Chronology Quantification	Chronology Classification
Damage: Microcracking	/	+	+	~	~	+	+
Damage: Fibre breakage	/	~	~	~	~	+	+
Damage: Intra-bundle crack	/	+	+	+	+	+	+
Damage: Inter-bundle crack	/	+	+	+	+	+	+
Damage: Delamination	/	+	~	~	+	+	+

[1] Non-destructive testing/Destructive testing

[2] Existing flaws

-: not relevant | ~: difficult / moderately relevant | +: relevant

2.3 Damage in composites

Before discussing the interaction between damage and time-dependent behaviours in Polymer Matrix Composites (PMCs), it is relevant to recall the main damage mechanisms at different scales in composite laminates. Damage is defined as an irreversible deterioration more or less extensive within the material. Damage generally causes a degradation of the material's mechanical and/or physical properties long before the ultimate failure. Composites are multiscale materials. Their damage mechanisms can therefore be defined at several observation scales:

The microscopic scale (*i.e.*, fibre's scale) enables the observation of matrix microcracking, fibre failure, as well as interfacial debonding between fibres and matrix.

The mesoscopic scale (*i.e.*, ply's scale) enables the observation of intralaminar cracking, either matrix cracking or intrabundle cracking, translaminar cracking (*i.e.*, fibre bundle failure) and interbundle cracking, also called meta-delamination.

The macroscopic scale (*i.e.*, laminate's scale) enables the observation of delamination (*i.e.*, interlaminar cracking).

These damage mechanisms are generally interdependent. Therefore, damage accumulation within woven composites is a complex interaction between these mechanisms. Furthermore, damage development is influenced by other parameters, such as:

- geometrical features:
  - macro-geometry: stacking sequence and layer nesting.
  - micro- and meso-geometry (*i.e.*, bundle and weave geometrical features): bundle twist, local fibre volume fraction, bundle crimp from weave pattern, etc.
- intrinsic material properties: behaviour of each constituent, as well as the quality of the fibre/matrix interface [21].
- experimental conditions: temperature, solicitation rate, direction of solicitation, hygrothermal environment, etc.

2.3.1 Chronology of damage in woven laminates

As introduced in section 2.1.2, the mechanical response of PMCs and therefore damage mechanisms depend on the loading conditions.

2.3.1.1 On-axis loading

Damage development in woven-ply laminates under on-axis tensile loading (*i.e.*, solicitation direction is parallel to the warp or weft bundles) has been investigated by many researchers in composites consisting of TS and TP matrices. A general damage scenario can be established in woven composites subjected to on-axis solicitations, though damage development depends on several parameters, as it will be pointed out.

The first observable damage mechanisms at the mesoscale is generally intra-bundle cracking (Figure 2.19b) within transverse bundles (*i.e.*, bundles perpendicular to solicitation direction), also called transverse cracking, which results from the coalescence of several fibre-matrix microdebondings (Figure 2.19a). Those transverse cracks generally grow instantaneously across the bundle thickness and may span two bundles through the thickness if those are side-by-side and have the same orientation [31]. Tranverse intra-bundle cracking generally initiates at the overlapping areas [17,26,36]. An increasing load results in the accumulation of intra-bundle cracks and their propagation along the bundle length [31]. Intra-bundle cracking leads to metadelamination (*i.e.*, inter-bundle cracking) at the "interface" between bundles with different orientations (Figure 2.19b) and may result in local fibre breakage within the longitudinal bundles (Figure 2.19c). Those inter-bundle cracks especially occur at the crimp regions [31]. Upon further loading, resulting in the spread of the previous damage mechanisms, the laminate fails due to cascade failure of longitudinal bundles owing to local fibre breakage and stress redistribution. More or less extensive fibre bundle pull-out may occur depending on the fibre-matrix interface quality [21].

Some matrix cracking can occur inside resin-rich areas. It is however usually intra-bundle cracks that propagate into those resin pockets [36]. Intra-bundle cracking are sometimes observed within longitudinal bundles (*i.e.*, splitting) [17] due to the combined effect of Poisson contraction of the longitudinal bundles under tension and the constraint imposed by the presence of transverse bundles [62].

2.3.1.2 Off-axis loading

Under off-axis solicitations (*e.g.*, at 45°), the matrix and fibre-matrix interface behaviours are prevailing. Many researchers studied the damage occurring in TS [19, 33, 65, 66] and TP [20, 21, 37] woven composites subjected to off-axis solicitations.

The usual chronology of damage mechanisms in woven composites under quasi-static tensile loading is described as follows:

- Onset of inter- and/or intra-bundle cracking depending on the interface quality. The

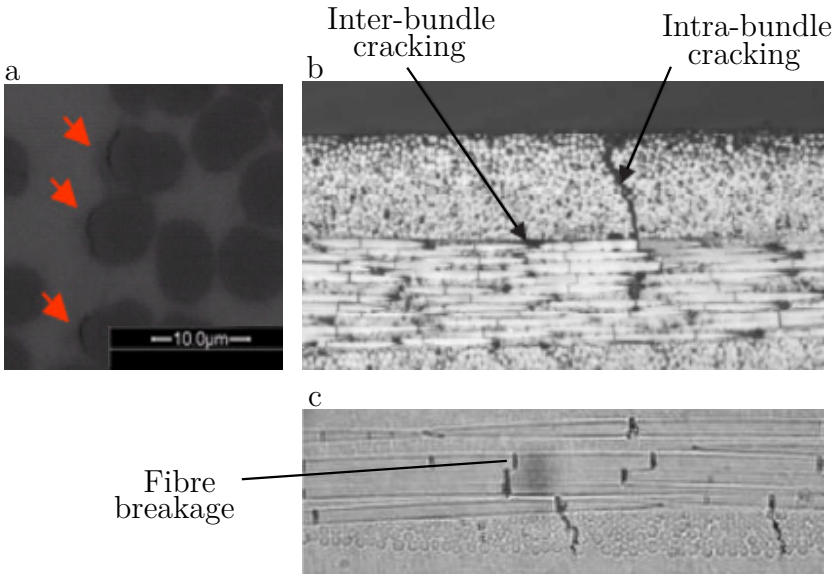

Figure 2.19 Damage mechanisms within woven-ply laminates during an on-axis solicitation: (a) fibre/matrix debonding [36], (b) transverse cracking resulting in inter-bundle cracking [33] and (c) local fibre breakage [17].

initial damage mechanism is not really clear in the literature. Intra-bundle cracking occurs within the weft and warp bundles for [(±45)] specimens. Intra-bundle cracks propagate through the thickness of one or two bundles, but generally stop at the inter-ply or inter-bundle interfaces. It seems that the cracking density in [(±45)] laminates is higher than that observed in [(0/90)] laminates [33].

- Accumulation of the latter mechanisms and development of meta-delamination and delamination from microcracks due to scissoring between warp and weft bundles. According to Karayaka et al. [65] delamination starts at the free edges and propagates along the weave directions.

- The ultimate failure occurs when the bundles near the center fail and pull-out from the matrix.

The damaged area is relatively spread, when compared to that observed in on-axis specimens. Damage accumulation is generally accompanied by matrix plasticity and progressive fibre bundle rotation [6, 18, 19, 21, 23] with a possible necking of the specimen [6].

2.3.1.3 Micro-, meso- and macro-geometry features

Damage development can be influenced by several geometry features at different scales. For example, Daggumati et al. [36] explained the difference in AE onset, which is associated with inhomogeneities-based damage initiation, of two different batches of the same 5HS C/PPS composite through variations at the microscale (*e.g.*, fibre spacing and intra-yarn volume fraction) and at the laminate scale (*e.g.*, ply nesting). However, the rise in events due to accumulation of intra-yarn cracks occurred at the same load around 200 MPa. Osada et al. [17] and Montesano et al. [26] highlighted that damage onset was delayed for weave patterns with less crimp regions. Osada et al. observed tranverse cracking onset for strains of 0.4% and 0.8% for plain weave and satin weave, respectively. Furthermore, fibre fracture onset occurred simultaneously for the satin laminate, whereas fibre breakage started later for the plain weave composite (about 0.8%). Montesano et al. observed that the transverse cracking onset were 140 MPa and 200 MPa for 5HS and 8HS woven composites, respectively, through IR thermography. This delay in crack initiation was explained through difference in crimp angle resulting in a different flexural state in the bundles.

2.3.1.4 Effect of temperature

It was previously shown that temperature has more impact on the mechanical behaviour in the case of an off-axis solicitation, when compared to an on-axis one. Thus, it is expected to be the same for damage development. Kawai et al. [24] highlighted this statement in the case of a plain woven C/epoxy under quasi-static tensile loading. The failure morphologies of [(0/90)] specimens solicited along the warp and weft directions were similar between RT and 100 °C. However, an increase in temperature resulted in more delamination and pull-out in off-axis samples. This conclusion has been also drawn by Selezneva et al. [66] in off-axis 8HS woven C/Bismaleimide (BMI) under fatigue for temperatures ranging from 25 °C to 205 °C, for which the authors observed a larger zone affected by necking and delamination. The driving factors behind those variations with temperature are the decrease of shear strength and shear deformation resistance of the matrix, as well as the strength of fibre/matrix interface [19, 24, 66]. Montesano et al. [19] assumed that such temperature-dependent behaviour results from the characteristic viscoelastic and/or viscoplastic behaviour of the matrix. Furthermore, it seems that the cracks observed at higher testing tempeatures are “smoother”, when compared to the “brittle” ones observed at RT, and are accompanied by local matrix deformation [19, 66].

A few authors also studied the effect of a thermal loading on damage within woven ply composites. Ahci et al. [67] underlined that thermal strains could initiate crack growth on the

outer edges and voids in the mid-section in a 8HS woven C/polyimide thermally loaded to 700 °F, but it seems they have a negligible effect on existing damage. Gupta and Raghavan [25] noted longitudinal edge cracks within transverse bundles in a [(0/90)] plain weave C/epoxy laminates after conditioning to erase physical aging. The cracks develop due to process-induced residual stresses resulting from the mismatch in cure shrinkage and thermal expansion between the warp and weft bundles. There are internal residual thermal and moisture absorption stresses due to the dissimilarity in properties between embedded fibers and polymer matrices. This phenomenon is far more pronounced in TS-based composites, when compared to TP-based laminates [68].

2.3.2 Damage and time-independent behaviour

As discussed in Section 2.2.1, damage accumulation generally results in a decrease in the macroscopic homogeneous equivalent material's stiffness due to the reduction of the surface that bears the applied load. It is usually observed through a knee-point in the stress-strain curves [17, 18] which seems to correspond to the accumulation of transverse cracking. This non-linearity is more or less pronounced depending on several parameters (*e.g.*, solicitation, material properties, etc.).

Many authors studied the effect of damage development on 5HS C/PPS laminates' stiffness [6, 20,21]. Carnevale [21] estimated the axial stiffness of two 5HS C/PPS laminates with different fibre sizing at RT solicited along the warp direction during load-unload tests. A decrease in stiffness occurred in specimens with poor interfacial properties, whereas no significant reduction was observed in specimens with a good interface quality. Figure 2.20 shows the variation in axial stiffness for the specimen with low interfacial properties. The small decrease between 200 and 400 MPa is due to transverse cracking development, whereas the steep reduction around 400 MPa is attributed to rapid growth of weft bundle debonding. This stiffness loss may result from the increase in longitudinal strain because the warp bundles are less constraint by the weft ones.

Bassery [20] and Albouy [6] also evaluated the axial stiffness in [(±45)] 5HS C/PPS specimens during load-unload tests at RT and 120 °C, respectively. Both authors noted a decrease of 5% in stiffness around 80 MPa due to damage development. An increase in stiffness was then noted at about 175 MPa (RT) [20] and at 150 MPa (120 °C) [6]. Damage development and fibre rotation are two competitive phenomena influencing the specimen stiffness. This

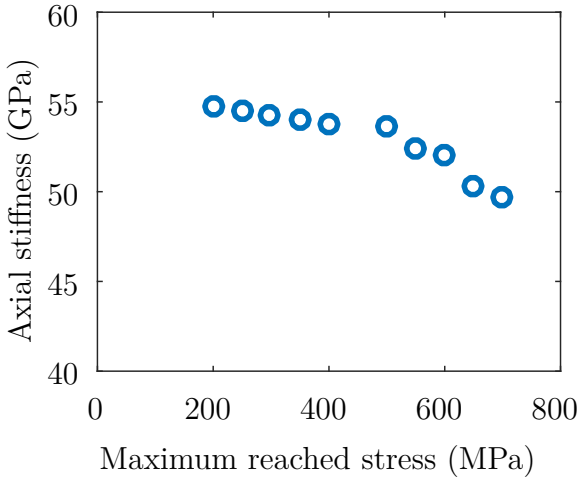

Figure 2.20 Axial stiffness reduction for a 5HS C/PPS specimen with a low interfacial quality (*i.e.*, as received) solicited along the warp direction at RT. The first decrease in stiffness results from intra-bundle cracking, whereas the second decrease results from inter-bundle cracking [21].

competition is illustrated in Figure 2.21 through a stiffness-based damage variable [6]:

$$d = 1 - \frac{E_i}{E_0}, \tag{2.5}$$

with E_i being the axial stiffness of the i^{th} load and E_0 being the initial stiffness.

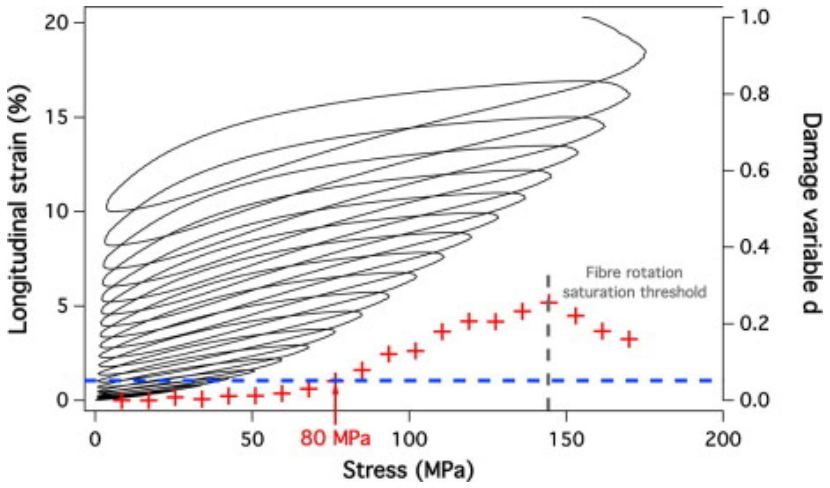

Figure 2.21 Variation of a stiffness-based damage variable (Equation 2.5) as a function of the applied stress for a [(±45)] 5HS C/PPS specimen during a load-unload test at 120 °C [8]. The onset of damage, which is defined at $d = 5\%$, is detected at about 80 MPa. Irreversible fibre bundle rotation can be observed through a stiffening (*i.e.*, a reduction in d) around 150 MPa.

2.3.3 Interaction between damage and time-dependent phenomena

Damage develoment and time-dependent behaviours (*i.e.*, viscoelasticity and viscoplasticity) occur in most woven PMCs, as highlighted in the previous sections. Those two phenomena may interact with each other in a complex fashion. Indeed, time-dependent phenomena may induce damage. Conversly, the damage state of a laminate may modify its time-dependent behaviour in the same manner that damage influences its macroscopic elastic properties. "Mechanical softening may include inherent viscoelastic [and/or viscoplastic] behaviour of the undamaged material, the growth of damage, and time-dependent opening and slidind of the crack faces that have formed", as stated by Bocchieri and Schapery [69]. Raghavan et al. [70] differentiate Time-dependent damage (TDD) and Time-independent damage (TID). TDD mainly occurs jointly with creep deformation and TID develops during transient quasi-static loading [71]. The separation of each softening or hardening effect are necessary to predict reliable long-term behaviour for arbitrary loading histories.

Most of the experimental investigations studying the interaction between damage and time-dependent behaviours in the literature deal with UD-based multidirectional laminates. Very few authors focused on this interaction in woven laminates.

2.3.3.1 Influence of time-dependent phenomena on damage - TDD

Time-dependent damage in multidirectional non-woven laminates

On the one hand, most researchers studied the time-dependency of transverse cracking in multidirectional composites by means of creep tests [70, 72, 73]. Moore et al. [72] highlighted that the matrix cracking process is time-dependent by experimentally estimating the increase in transverse crack density within 90°-plies as a function of time for Kevlar/epoxy and C/epoxy cross-ply laminates. Ogi and Takao [73] observed an increase in transverse crack density along with a significant amount of viscoelastic strain and concluded that most of those transverse cracks were generated by the increase in strain due to viscoelasticity. Then, crack density kept increasing, though the creep strain increase was very small. This second cracking process is called "delayed fracture". Those previous studies only focused on one damage mode, i.e. transverse cracking in 90° layers. Thus, Birur et al. [74, 75] studied the development of various damage mechanisms over time in C/epoxy multidirectional laminates subjected to creep loading for different stacking sequences. They showed that the applied stress, the temperature and the stacking sequence influenced damage development and thus the creep rupture time.

On the other hand, many researchers studied the time-dependent damage in multidirectional composites by means of different loading rates [70, 72, 76]. Raghavan and Meshii [70] highlighted that First-Ply-Failure (FPF) stress and strain, as well as progressive cracking, are strain rate-dependent due to viscoelasticity of 90°-plies and resin-rich interlaminar layer for C/epoxy cross-ply laminates. Lafarie-Frenot et al. [76] showed that the higher the loading rate is, the higher the FPF stress and the faster the increase in crack density are. The nonlinear viscoleastic behaviour of the undamaged material cannot explain alone the rate sensitivity of the damaging process [77]. However, a rate-dependent failure criterion representative of the viscoelastic behaviour of the failing material around crack fronts gives a good agreement between experiments and simulations.

The previous studies are mainly based on optical observations. Bocchieri et al. [69, 78] studied time-dependent damage development through AE monitoring. Significant AE events are observed during dwell stages of ramp-hold tests (Figure 2.22a). These events are related to time-dependent damage. Furthermore, no AE events are detected until the stress is significantly higher than the dwell stress for subsequent ramps, suggesting possible microstructural stress relaxations. However, the loading rate does not seem to influence cumulative AE events during monotonic tensile tests (Figure 2.22b).

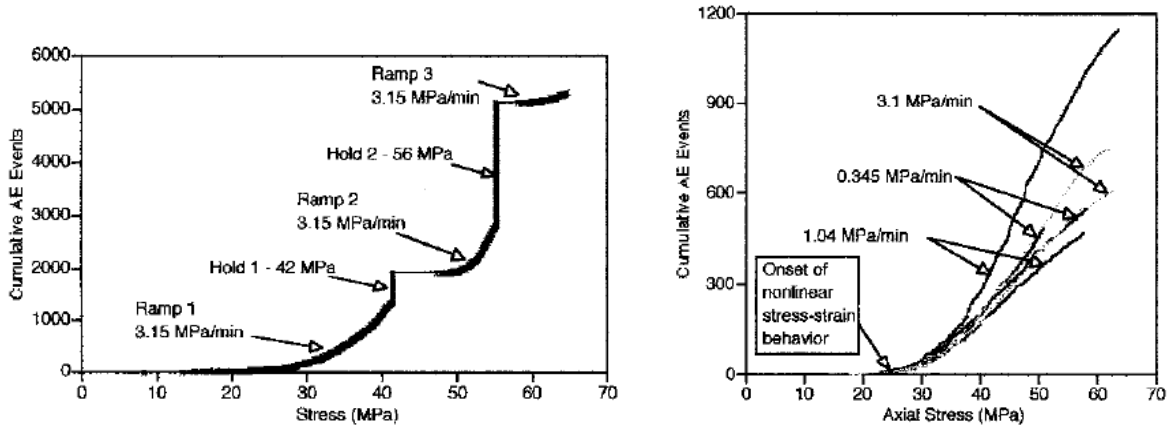

(a) (b)

Figure 2.22 AE monitoring for time-dependent damage investigations [69, 78]. (a) Time-dependent AE event accumulation during hold stages and (b) rate-independent AE event accumulation. Significant AE events are observed during dwell stages of ramp-hold tests, especially during the second one. This AE activity is related to TDD. However, no influence of the loading rate on the AE activity is observed.

Time-dependent damage in woven laminates

There are only few works highlighting time-dependent damage occurring in woven PMCs [20, 79], and these references do not specifically focus on time-dependent damage accumulation. Bassery [20] observed transverse cracking during creep and load-relaxation tests in $[(\pm 45)]_7$ 5HS C/PPS laminates at RT. However, based on those tests, one cannot really tell if those cracks are formed due to time-dependent phenomena or to transient loading. Gupta [79] noticed an increase in the number of longitudinal, transverse and delamination cracks during creep tests at different temperatures and stresses in $[(0/90)]_6$ plain weave C/epoxy composites. At a constant temperature, TDD is more likely to occur for higher stress level, and at a constant stress level, TDD is more likely to occur for higher temperature. Gupta also investigated time-dependent damage in $[(\pm 45)]_6$ plain weave laminates, but no crack accumulation could be observed from X-ray scans due to resolution issues. Still, time-dependent damage occurred during creep at certain stress levels and temperatures because the residual strain after creep increased, when compared to the residual strain after loading-unloading under the same experimental conditions. Furthermore, the creep compliances were compared for a given experimental condition (7 MPa and 80 °C) with a master curve obtained through time-temperature superposition (7 MPa and 80-160 °C). The master curve exhibited an increase in creep rate after 1000 minutes, corresponding to the data obtained at 160 °C, when compared to the single specimen test. This observation possibly underlines time-dependent damage development. However, this work did not take into account possible visco-plasticity.

The influence of loading rate on damage in $[(\pm 45)]_7$ 5HS C/PPS laminates [20] was investigated using the change in axial stiffness during loading-unloading tests at RT, as illustrated in Figure 2.23. It appears that the variation in axial stiffness due to damage and the loading rate are not monotonically correlated at RT. The influence of strain rate on the mechanical properties at failure (*i.e.*, stress and strain at break) was also investigated in specimens solicited monotonically along the warp, weft and 45° directions at RT, as illustrated in Figure 2.24. As a result, it seems that there is no influence in specimens solicited along the warp and weft directions, and the influence might not be significant in $[(\pm 45)]$ laminates due to the data dispersion.

Cyclic creep test - Mechanical conditioning

Composite materials may be damaged upon loading to creep stress. Considering a viscoelasto-plastic matrix, damage can develop during creep alongside viscoelastic and viscoplastic strains. Upon unloading, damage growth and viscoplastic strain stop. Upon another cycle, damage and viscoplastic strain can increase, even if the material is loaded at the same creep stress during the same time due to the nature of the material. However, this phenomenon tends to become negligible as the number of cycles increases, at least for a short number of cycles. A few authors underlined this mechanical conditioning effect on composites' creep and recovery compliances, which reflects either damage growth and/or viscoplastic strains [69, 80]. Lou and Schapery [80] observed that the creep strain of successive creep/recovery tests becomes smaller until a stable state for each successive cycle for off-axis UD glass/epoxy laminates is reached. A reduction in creep strain representing 3% of total strain or 20% of transient strain took place between the first and the tenth cycles. This decrease in creep strain is probably due to a decrease in crack growth rate as the damage state reaches a saturation level, which should depend on the stress state as well as the internal length of the microstructure. According to Lou and Schapery, such crack initiation and crack growth may have an effect on the transient creep compliance depending on several factors like temperature, loading and material features. Bocchieri and Schapery [69] studied the cyclic effect on creep and recovery compliances on UD C/rubber-toughened epoxy laminates. The creep and recovery behaviour could differ from a cycle to another depending on the fibre orientation, as well as the stress level. Damage development and viscoplastic strain may explain these differences.

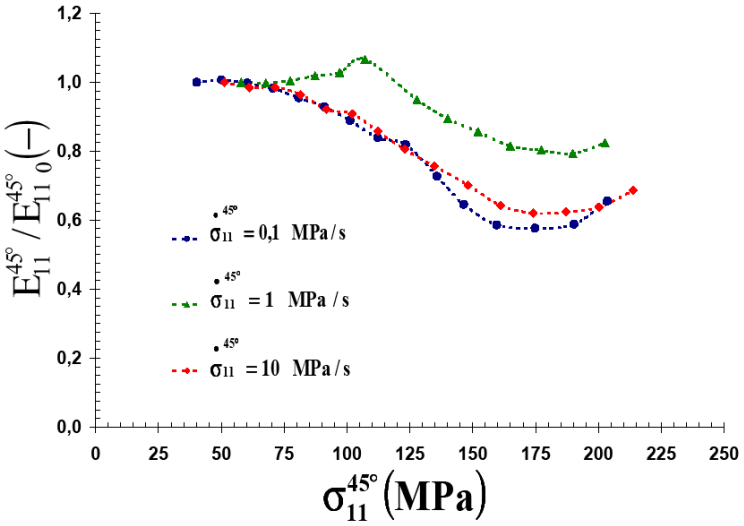

Figure 2.23 Evaluation of damage development based on the change in axial stiffness during load-unload tests at different loading rates in $[(\pm 45)]_7$ 5HS C/PPS specimens at RT [20]. It appears that the loading rate and the stiffness reduction related to damage development are not monotonically correlated at RT.

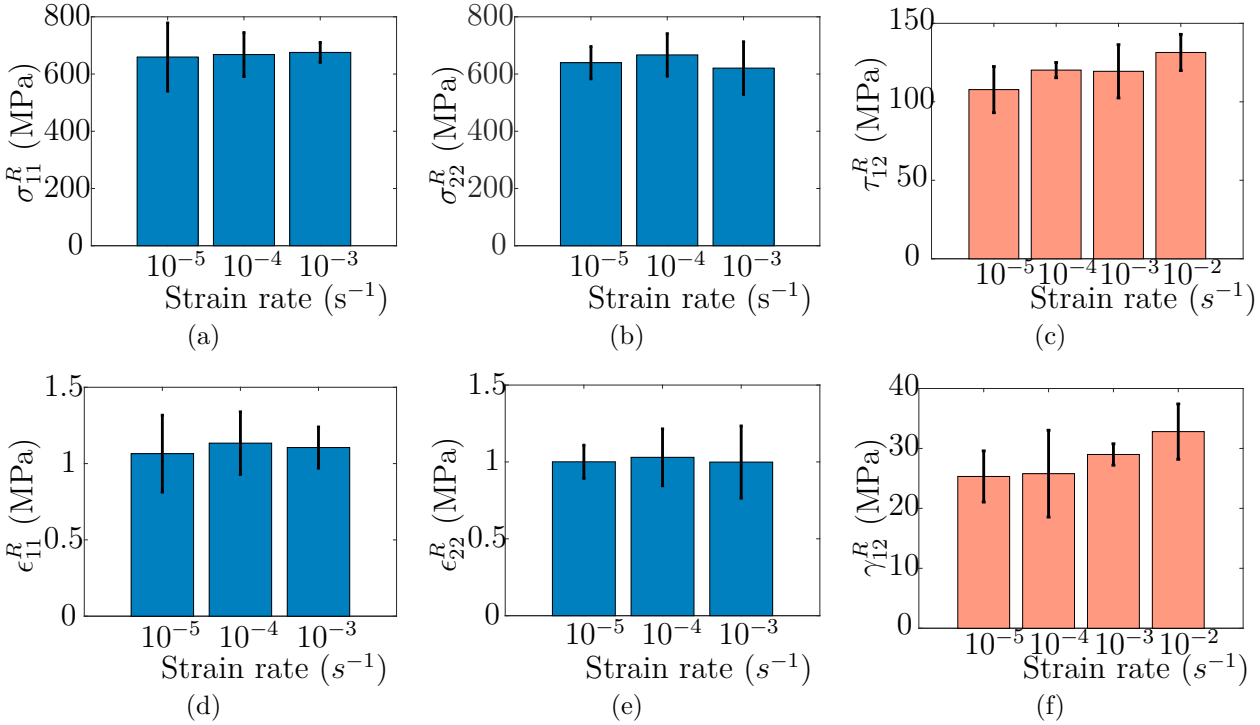

Figure 2.24 Stress and strain to failure in 5HS C/PPS laminates solicited along (a)(d) the warp bundles, (b)(e) the weft bundles and (c)(f) the 45° direction at RT [20]. Those two properties are strain rate-independent for on-axis loading. The trend observed in the off-axis case seems to be insignificant based on the data dispersion.

2.3.3.2 Influence of damage on time-dependent behaviour

The literature about the influence of damage on the elastic properties of composites is rich for UD-based multidirectional and woven laminates. However, when it comes to investigate the influence of damage on the time-dependent behaviour of composites, the literature is scarce, especially in terms of experimental investigations.

A few researchers studied the creep response of mechanically pre-conditioned materials [67, 69, 81] in order to improve the test repeatability and characterize the visco-elasto-plastic behaviour by reducing the effects of growing damage. Pre-conditioning generally consists in pre-loading the sample, either at a higher load or by cyclic loading, in order to reach a damage state that will stay constant during the subsequent steps to characterize the time-dependent behaviour. Plastic strains occur alongside damage during preconditioning. The effect of damage on the nonlinear viscoelastic parameters (*i.e.*,, a_σ, g_0, g_1 and g_2) of 30°, 45° and 90° UD C/rubber-toughened epoxy laminates was investigated by preconditioning the material at several stress levels leading to different damage states [69]. First, the authors noted that a_σ was not influenced by damage because the recovery curves could be vertically shifted to the lowest damage state. Secondly, they observed that damage influences shear viscoelastic behaviour through g_1^c and g_2^c, whereas damage modifies the transverse viscoelastic behaviour only through g_2^c. Zaoutsos and Papanicolaou [81] investigated the effect of preloading on the visco-elasto-plastic behaviour of 90° C/epoxy UD laminates. The creep strains of classical creep tests were compared to the ones of creep tests preceded by cyclic loading. An increase in creep strain was observed in the case of combined preloading-static loading compared to the creep tests, especially for the higher stress levels. They concluded that preloading mainly influences the viscoplastic behaviour of the material because the nonlinear parameters g_0, g_1, g_2 and a_σ were not affected.

2.4 Fracture toughness in woven composites

The identification of several fracture parameters (*e.g.*, critical strain energy release rate, critical stress intensity factor, etc.) are necessary to predict the crack propagation within a composite, due to its inhomogeneous and anisotropic behaviour. The strain energy release rate depends on several factors, such as the failure mode (*e.g.*, mode I, II, II) and corresponding failure mechanisms (*e.g.*, intra-, trans- and inter-laminar). Furthermore, most of the failure mechanisms occur concurrently, which makes the investigation of one failure type relatively difficult. Therefore, very few tests are standardized in the case of fracture in composites.

2.4.1 Fracture mechanics overview [82]

Locally, fracture is the irreversible separation of a continuous medium into two distinct parts, which results in a discontinuity of the displacement field. Three different rupture mode exist according to the relative displacement of the two surfaces: opening (I), sliding (II) and tearing (III) modes.

There are different ways to consider fracture mechanics: (i) locally through stress and displacement fields around the crack tip which are uniquely characterized by a fracture parameter such as the Stress Intensity Factor (SIF) K, and (ii) more globally with an energy criterion like the Strain Energy Release Rate (SERR) G. The energy criterion approach states that crack extension occurs when the available energy is greater than or equal to a critical value, which represents the material resistance to crack propagation. This value includes any energy dissipation associated with crack propagation, *e.g.* surface energy, plastic work, secondary cracks, etc. Finally, different fracture mechanics frameworks and fracture toughness parameters are used depending on the material behaviour (*e.g.*, linear elasticity or elasto-plasticity).

2.4.1.1 Linear Elastic Fracture Mechanics (LEFM) framework

Assumptions

The LEFM framework relies on the assumption that only Small Scale Yielding (SSY) occurs. In other words, when the plastic deformation extent is very small when compared to the Singularity Dominated Zone (SDZ) (*i.e.*, the zone where the crack-tip fields are affected by the presence of a crack) [82].

Local approach - SIF

The stress intensity factor characterizes the amplitude of the crack-tip singularity and completely defines the stress, strain and displacement fields in the SDZ (Figure 2.25b), *i.e.*, near the crack tip. For example, the stress field in a linearly elastic body can be written in mode I [82] as:

$$\sigma_{ij}^{(I)}(r,\theta) = \frac{K_I}{\sqrt{2\pi r}} f_{ij}^{(I)}(\theta) + \sum_{m=0}^{\infty} A_m r^{\frac{m}{2}} g_{ij}^{(m)}(\theta), \tag{2.6}$$

where

σ_{ij}: stress tensor

K_I: stress intensity factor in mode I

$f_{ij}^{(I)}$: dimensionless factor function of θ

A_m and $g_{ij}^{(m)}$ are the amplitude and a dimensionless function, respectively, for the mth term

r and θ are the polar coordinates as defined in 2.25a.

Closed-form solutions for K can be found for simple configurations (*e.g.*, simple shape crack in an infinite medium). However, closed-form solutions are not valid for cracks whose size is no longer small, when compared to the specimen size because boundary conditions influence the crack tip fields. K can be written as follows [83]

$$K = \sigma\sqrt{\pi a} f(a/W), \tag{2.7}$$

where

σ: remote stress is the stress far from the crack

a: crack dimension

W: specimen width

$f(a/W)$: finite-width correction factor (dimensionless constant depending on the geometry and loading mode)

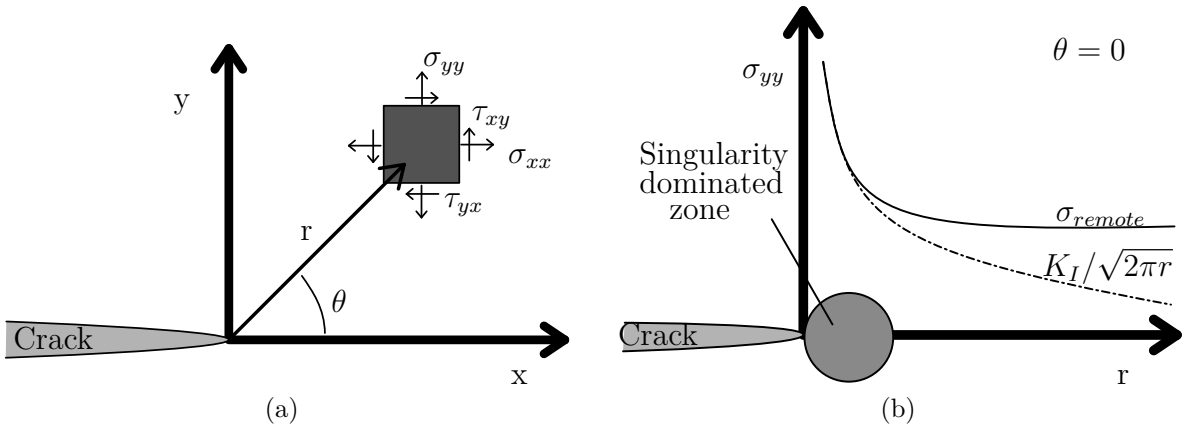

Figure 2.25 (a) Definition of the coordinate axis at the crack tip and (b) stress normal to the crack surface ahead of a crack tip (inspired from [82]). The SDZ is the zone where the crack-tip fields are affected by the presence of the crack.

Energy approach - SERR

An energy criterion approach was initially proposed by Griffith. The cracking process (*i.e.*, either initiation or propagation) is possible only if this process causes the total energy of the system to decrease or remain constant. Therefore, a critical condition can be defined as the point where crack grows under equilibrium conditions (*i.e.*, with no net change in the total energy) [82]. Thus, the Griffith energy balance for an incremental increase in the crack area dA under equilibrium can be written as

$$\frac{\mathrm{d}E}{\mathrm{d}A} = \frac{\mathrm{d}\Pi}{\mathrm{d}A} + \frac{\mathrm{d}W_s}{\mathrm{d}A} = 0, \tag{2.8}$$

where

E: total energy

$\Pi = U - F$: potential energy of an elastic body, where U is the strain energy stored and F the work done by the external forces

W_s: work necessary to create new surfaces

The SERR G was proposed by Irwin based on Griffith's approach and is defined as the variation of potential energy for an incremental increase in the crack area dA in a linearly elastic material:

$$G = -\frac{\mathrm{d}\Pi}{\mathrm{d}A}. \tag{2.9}$$

The SERR is also called the crack driving force because G is obtained from the derivative of a potential. The material fracture toughness is defined by G_c corresponding to the critical value for which crack extension occurs, and can be written as:

$$G_c = \frac{\mathrm{d}W_s}{\mathrm{d}A} = 2w_f, \tag{2.10}$$

where w_f is the fracture energy including surface energy and possible local nonlinear effects.

Resistance curve (R-curve) and instability

The R-curve is the change in critical strain energy release rate with increasing damage (*i.e.*, crack growth). Figure 2.26 illustrates different R-curves. R represents $2w_f$ (*i.e.*, material resistance to crack extension), whereas the plot of G as a function of crack extension is the driving force curve. Those plots illustrate the conditions for a stable crack growth, which can be expressed as:

$$G = R \tag{2.11}$$

and

$$\frac{\mathrm{d}G}{\mathrm{d}a} \leq \frac{\mathrm{d}R}{\mathrm{d}a}, \tag{2.12}$$

whereas instability occurs when

$$\frac{\mathrm{d}G}{\mathrm{d}a} > \frac{\mathrm{d}R}{\mathrm{d}a}. \tag{2.13}$$

The shape of the R-curve mainly depends on the material behaviour and, to a lesser extent, on the testing configuration [82]. Ideally, the R-curve or other fracture toughness measurements should be material dependent only. However, configurational effects exists (*e.g.*, edge effect, thickness, etc.). An ideally brittle material should have a flat R-curve, as illustrated in Figure 2.26a, because the surface energy is an invariant material property. A critical value G_c can be defined unambiguously in that case. Ductile failure generally leads to a rising R-curve (Figure 2.26b), which reflects the increasing size of a plastic zone at the crack tip. Therefore, the driving force must increase to propagate the crack.

The rate of change in the driving force G depends on the testing configuration. For example, though G is the same in load-controlled and displacement-controlled conditions, the slope of the driving force curve is different in both cases. A displacement-controlled mode generally results in a more stable crack growth than a load-controlled one [82].

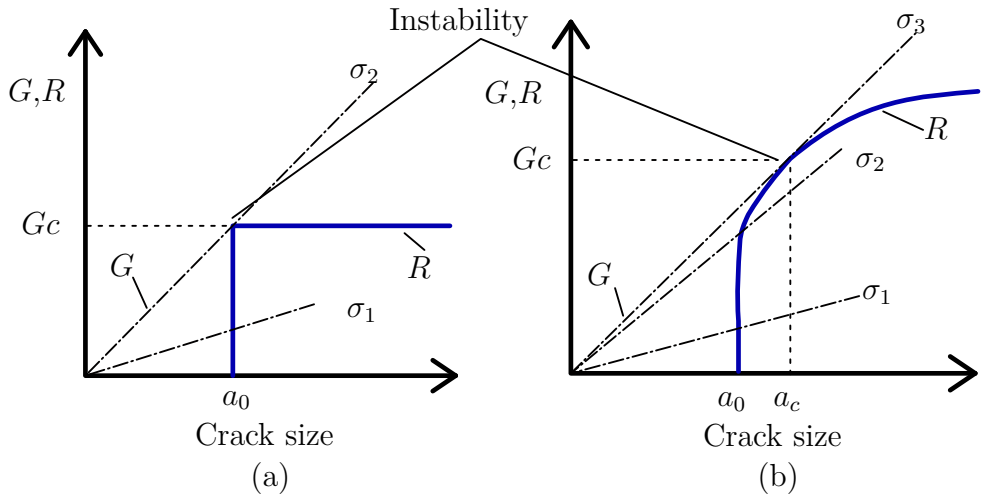

Figure 2.26 Illustration of R-curve and driving force as a function of crack length: (a) flat R-curve and (b) rising R-curve (inspired from [82]). A R-curve is the change in critical strain energy release rate with increasing crack length. The shape of the R-curve mainly depends on the material behaviour.

Relation between K and G

The SERR for orthotropic materials can be calculated from the SIF using the following equation [83]:

$$G_I = \frac{K_I^2}{\sqrt{2E_{11}E_{22}}}\sqrt{\sqrt{\frac{E_{11}}{E_{22}}} + \frac{E_{11}}{2G_{12}} - \nu_{12}}, \tag{2.14}$$

where E_{11} and E_{22} are the elastic moduli in the 1 and 2 directions, G_{12} the shear modulus and ν_{12} the in-plane Poisson's ratio.

2.4.1.2 Elastic-Plastic Fracture Mechanics (EPFM) framework

LEFM-based fracture toughness parameters, K and G, rely on the assumption that nonlinear material deformation is confined to a small region surrounding the crack tip. When the plastic zone expands to a larger zone, EPFM is required. This situation is either dealt with plastic zone corrections or with a nonlinear elastic analysis. The latter handles plasticity as nonlinear elasticity and uses the J contour integral to characterize fracture toughness.

J contour integral

The J-integral is a path-independent contour integral introduced by Rice [84] and is defined

as:

$$J = \int_{\Gamma} (w \mathrm{d}y - T_i \frac{\partial u_i}{\partial x} \mathrm{d}s), \tag{2.15}$$

where

Γ: arbitrary counterclockwise path around the crack tip (Figure 2.27)

T: traction vector

u: displacement vector

$\mathrm{d}s$: length increment along Γ

w: strain energy density defined as

$$w = \int_0^{\epsilon_{ij}} \sigma_{ij} \mathrm{d}\epsilon_{ij} \tag{2.16}$$

J-integral as a fracture toughness parameter

Rice [84] stipulated that J had a similar mathematical definition as the SERR G, but for a nonlinearly elastic material. J can be expressed as

$$J = -\frac{\mathrm{d}\Pi}{\mathrm{d}A}. \tag{2.17}$$

J can be seen as a more general version of G and in the case of a linearly elastic material $J = G$. However, the physical interpretation is different. G is defined as the potential

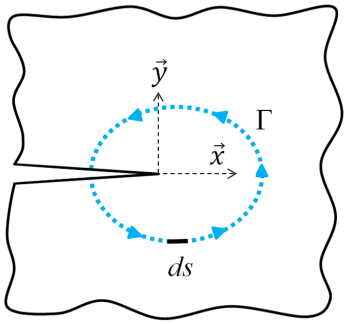

Figure 2.27 Illustration of the J contour integral.

energy required for an increment of crack extension within an elastic body, whereas J rather characterizes the difference in elastic-plastic work for specimens with different crack sizes [85]. However, J can still characterize the crack-tip stresses and strains fields. J can be seen as an energy parameter as well as a stress intensity parameter [82].

Experimental evaluation of J

There are many methods to measure J experimentally. Landes and Begley proposed an approach based on the strain energy release rate definition of J, using multiple test specimens with various crack lengths [86,87]. However, this method is material-consuming as it requires lots of specimens.

Rice et al. [88] proposed the first single-specimen method from the strain energy release rate formulation of J (Eq. 2.17) by separating it into elastic, J_{el}, and plastic, J_{pl}, components, as:

$$J = J_{el} + J_{pl} = G + J_{pl}. \tag{2.18}$$

Sumpter and Turner [89] generalized this expression of J as:

$$J = \eta_{el}\frac{A_{el}}{Bb} + \eta_{pl}\frac{A_{pl}}{Bb} = G + \eta_{pl}\frac{A_{pl}}{Bb}, \tag{2.19}$$

where A_{el} and A_{pl} are the elastic and plastic works done, respectively. η_{el} and η_{pl} are parameters that depend on the specimen's geometry and loading conditions. B and b are the specimen's thickness and the uncracked ligament length, respectively. A_{el} and A_{pl} are calculated from the load-Load Line Displacement (LLD) curves, as schematized in Figure 2.28.

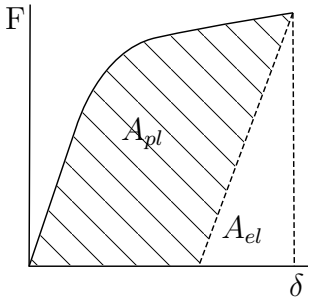

Figure 2.28 A typical load-LLD curve for an elasto-plastic material. A_{el} and A_{pl} are the elastic and plastic works done, respectively.

2.4.1.3 Fracture mechanics parameters for cyclic loading

Since the J-integral was developed under the nonlinear elasticity assumption, analyses based on this assumption should not be valid for elastic-plastic materials if unloading occurs. Dowling and Begley [85, 90] were the firsts to apply the J-integral concept to cyclic loading to predict fatigue crack growth and introduced the ΔJ concept, also called the J-integral range.

Under cyclic loading the material ahead of a crack tip experiences a cyclic elastic-plastic behaviour, as illustrated in Figure 2.29a. The material behaviour can be characterized by the stress range $\Delta\sigma_{ij}$ and the strain range $\Delta\epsilon_{ij}$ for a given cycle. Considering the loading part of a cycle, ΔJ can be written as

$$\Delta J = \int_{\Gamma}(\Psi(\Delta\epsilon_{ij})\mathrm{d}y - \Delta T_i \frac{\partial \Delta u_i}{\partial x}\mathrm{d}s), \tag{2.20}$$

where

Γ: arbitrary counterclockwise path around the crack tip (Figure 2.27)

ΔT: change in traction vector

Δu: change in displacement vector

$\mathrm{d}s$: length increment along Γ

Ψ: a quantity analogous to the strain energy density defined as

$$\Psi(\Delta\epsilon_{kl}) = \int_0^{\Delta\epsilon_{kl}} \Delta\sigma_{ij}\mathrm{d}(\Delta\epsilon_{ij}) = \int_{\epsilon_{kl}^{(1)}}^{\epsilon_{kl}^{(2)}} (\sigma_{ij} - \sigma_{ij}^{(1)})\mathrm{d}\epsilon_{ij} \tag{2.21}$$

The ΔJ concept is based on changes in quantities (*e.g.*, displacement, strain, etc.) from a reference state. The onset of crack opening/closure is generally defined as the reference state. It can be noted that in the case where $\sigma_{ij}^{(1)} = \epsilon_{ij}^{(1)} = 0$, $\Delta J = J$. Therefore, ΔJ can be seen as a generalization of the J-integral.

Similarly to J, ΔJ can be estimated experimentally using the load-LLD curve and separating the elastic and plastic components. Dowling [90] proposed an estimation method similar to Equation 2.19 using the hysteresis loops of the load-LLD cycles to compute the plastic component ΔJ_{pl}, as illustrated in Figure 2.29b, while the elastic component was evaluated using ΔK, which is the equivalent of ΔJ for elastic materials.

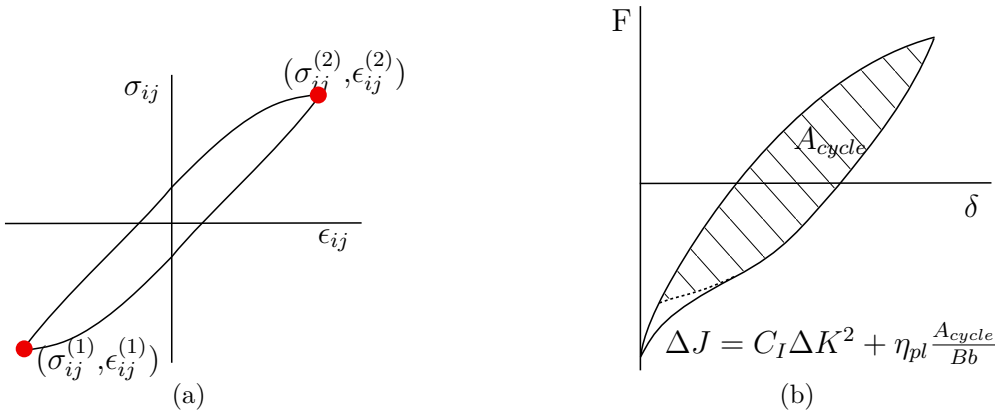

Figure 2.29 (a) Illustration of the cyclic stress-strain behaviour ahead of a crack tip and (b) definition of cyclic J based on [90].

The applicability of the ΔJ concept as a fracture toughness parameter for cyclic loading is still controversial from a theoretical standpoint. However, a good correlation between ΔJ and fatigue crack growth rates is observed [90].

2.4.2 Fracture in composites

Several damage mechanisms coexists within composite laminates, as presented in Section 2.3.1, which result in complex failure scenarios. The laminated nature of composite materials enables to categorize fracture in composites into three different basic failure modes at the mesoscale: interlaminar, translaminar and intralaminar failures, as illustrated in Figure 2.30 [91]. Crack formation and propagation within a laminate depend on both the stacking sequence and the boundary conditions. Thus, laminates failure is driven by one or a combination of the aforementioned mesoscopic failure modes. The failure mechanisms occurring during an in-plane tensile loading are mainly translaminar fibre tensile failure and intralaminar matrix failure [91].

2.4.2.1 Interlaminar failure

The interlaminar fracture toughness of UD- and woven-ply composites has been widely investigated in the literature to characterize delamination, which is a critical failure mode, especially during impact. Furthermore, the massive literature on that subject results from the ease of use of fracture mechanics tools (initially developed for metals) to a propagating crack within the inter-ply region, *i.e.*, the matrix, which is an homogeneous isotropic material.

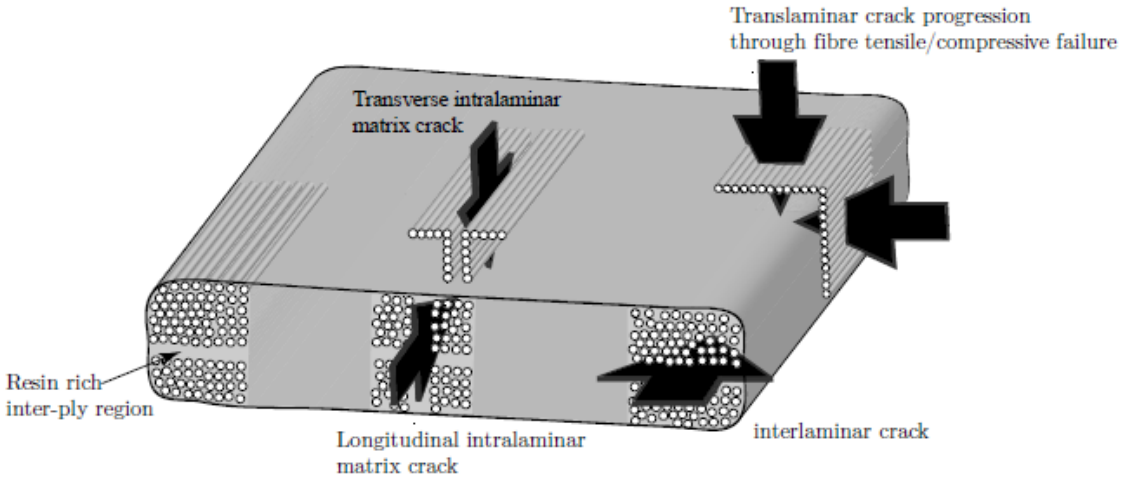

Figure 2.30 Overview of failure modes at the ply-level in laminated composites [91].

A few references focused on the rate-dependency of interlaminar fracture toughness of woven composites since the matrix plays an important role in interlaminar failure. Zabala et al. [92] underlined a decrease in fracture energy release rate with an increase in loading rate for an UD and a plain weave C/epoxy laminates. A reduction of 19% (from $8.3 \times 10^{-5}\,\mathrm{m\,s^{-1}}$ to $0.190\,\mathrm{m\,s^{-1}}$) for the woven case, and a reduction of 32% (from $8.3 \times 10^{-5}\,\mathrm{m\,s^{-1}}$ to $0.048\,\mathrm{m\,s^{-1}}$) in the UD case. Mall et al. [93] also underlined a decrease of 65% in interlaminar fracture toughness when crosshead speed increases from 0.05 cm/min to 100 cm/min in plain weave graphite/PEEK composites.

2.4.2.2 Intralaminar failure

The intralaminar fracture toughness is comparable to the interlaminar fracture toughness because the fracture processes are similar [94]. Both are characterized by the formation/propagation of a matrix crack.

2.4.2.3 Translaminar failure

The literature about translaminar fracture toughness in composites is scarce. Most of the studies are still based on tools developed for metallic materials and are limited to the LEFM framework, even though the crack propagates through an heterogeneous and anisotropic medium in composites. A good review on translaminar fracture toughness of UD ply-based laminates is given in [91]. A stable crack growth is required to evaluate the changes in the critical strain energy release rate with increasing damage (*i.e.*, crack length), resulting in

a R-curve. The specimen geometries used in the literature to investigate the translaminar fracture are summarized in Figure 2.31 [91]. Only the Compact Tension (CT), three- and four-point bends and Extended Compact Tension (ECT) specimens result in a stable crack growth, according to Laffan et al. [91]. It also appears that ECT geometry is preferable to avoid any undesirable failure modes. This geometry is the only one that is standardized [95]. However, this standard is limited to the determination of the SIF at initiation.

A few authors experimentally investigated the translaminar failure in woven-ply laminates, either in the LEFM framework [40, 96–100] or the EPFM one [99, 101]. Some conclusions made for UD-based laminates are also observed in woven-ply composites. It appears that CT specimens may lead to undesired failure mechanisms [100], but this is not always the case [96, 100]. In addition, a specimen geometry close to ECT seems to results in a stable crack growth [40]. Other geometries have also been used, such as Single Edge Notched Tension (SENT) [97–99, 101]. Finally, several methods are used to determine the fracture toughness: ASTM E1820-based method [96–101], area method [100], compliance method [100] and IR thermography-based method [40]. It appears that the translaminar fracture investigation is a relatively recent issue.

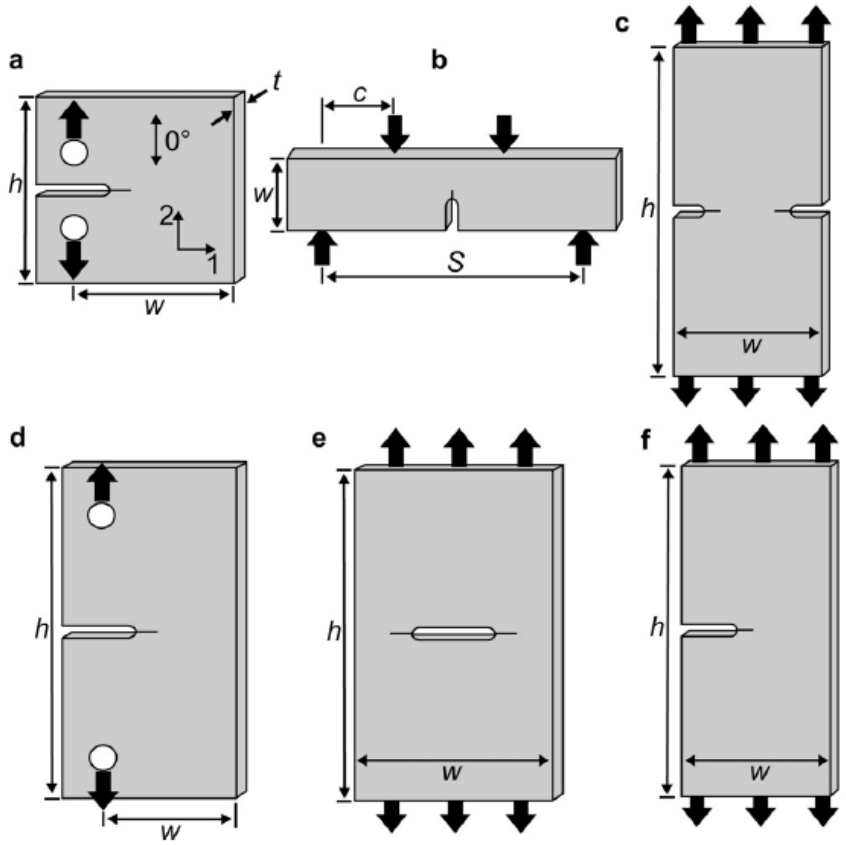

Figure 2.31 Specimen geometries used for translaminar fracture investigations: (a) compact tension or compression, (b) three- and four-point bend, (c) double edge notched tension, (d) extended compact tension, (e) centre notched tension and (f) single edge notched tension [91].

CHAPTER 3 OBJECTIVES

3.1 Summary and analysis of the literature

The literature review herein reveals that woven PMCs are prone to time-dependent phenomena during tensile in-plane solicitations, especially due to the time-dependent behaviour of the polymer matrix. Most factors influencing the macroscopic behaviour of woven composites are more or less closely related to the matrix' time-dependent thermomechanical behaviour. Woven laminates are more likely to have a time-dependent mechanical behaviour than UD-based laminated counterparts due to the presence of crimp regions [27, 28]. However, most experimental studies dealing with time-dependent behaviour of composites focus on UD-based laminates. Most experimental works about woven laminates in the literature investigate their elastic behaviour, very few studies deal with their viscoelastic and viscoplastic behaviours, especially when the temperature is above their glass transition temperature. According to the previous chapter, Angle-Ply (AP) 5HS C/PPS laminates display a time-dependent behaviour (*i.e.*, visco-elasto-plasticity) at RT and 120 °C, whereas QI C/PPS laminates have a limited time-dependent behaviour.

The literature concerning damage within woven laminates is quite rich for monotonic tensile tests and fatigue loading. Damage within woven-ply laminates is characterized by different mechanisms operating at different scales: (i) matrix microcraking, fibre/matrix debonding and fibre breakage at the microscopic scale, (ii) transverse cracking and metadelamination (*i.e.*, inter-bundle cracking) at the mesoscale and (iii) delamination at the macroscopic scale. Researchers have a good knowledge on damage chronology and its effect on the elastic behaviour of woven laminates. Damage generally starts as intra-bundle cracks from the coalescence of fibre-matrix microdebondings. These cracks mainly initiate at the crimp regions and generally lead to inter-bundle cracking. Then, the spread of intra- and inter-bundle cracking results in a combination of bundles failures and delaminations depending on the reinforcement orientation with respect to loading. Several parameters can influence damage development. One of them is the temperature which seems to decrease shear strength and shear deformation resistance of the matrix, as well as the strength of fibre-matrix interface [19, 24, 66].

Time-dependent phenomena are an important durability issue in composite materials. Time-dependent mechanical softening in polymer composites may include viscoelasticity and/or viscoplasticity of the polymer matrix, as well as damage development (*i.e.*, crack growth and opening/sliding of the crack faces) which can be time-dependent due to the surrounding visco-elasto-platic matrix [69]. Furthermore, a few other time-dependent phenomena can occur

simultaneously to the time-dependent mechanisms described above. This includes physico-chemical phenomena, such as aging of the polymer matrix (*e.g.*, physical aging, thermal aging, etc.), or structural ones (*e.g.*, rotation of the fibre bundle during off-axis solicitations). Several authors worked on the interaction between damage and visco-elasto-plasticity in PMCs. This interaction turns out to be a complex mechanism involving the visco-elasto-plasticity of the "undamaged" polymer matrix and the time-dependent behaviour of the failing material around the crack fronts (*i.e.*, surrounding visco-elasto-platic matrix). Most of those studies focus on UD-based laminates, but very few for woven laminates. Besides, no experimental studies focusing specifically on time-dependent damage development within woven laminates are available in the literature to the best author's knowledge. It should be noted that a few studies highlighted a rate-dependency of the interlaminar failure of woven laminates [92, 93]. A decrease in the interlaminar fracture toughness was observed with an increasing loading rate. This observation seems to concur with rate-dependent behaviour of polymers. Indeed, interlaminar failure is mainly characterized by the propagation of a crack within the matrix inter-ply region. No studies about the time-dependency of translamainar failure in woven laminates are available in the literature to the best author's knowledge.

A separation and an identification of each mechanisms are necessary to produce reliable long-term predictions. However, the experimental separation of each time-dependent softening effect, including the effect of damage growth, based on stress-strain data is relatively difficult. It is especially complicated for the whole loading histories since damage development may depend on it in complex ways [69]. Furthermore, damage qualification and quantification is quite challenging. One technique is generally not enough to fully characterize damage and its effects. Many authors generally recommend to couple several damage monitoring tools [34, 102]. It appears that the most versatile techniques are XμCT and AE monitoring (Section 2.2.7). One advantage of AE over XμCT is that AE is a real-time monitoring tool. However, AE monitoring generally needs to be coupled with another characterization tool, especially when the damage chronology is not known a priori.

3.2 Objectives

The understanding of the interaction between damage development and time-dependent mechanical behaviour in woven composites is necessary. The study of such an interaction must be ideally carried out via two primary stages: (i) the influence of matrix time-dependent behaviour on damage, *i.e.* TDD development, and (ii) the influence of damage on the macroscopic visco-elasto-plastic behaviour.

The present work focused on the first stage: the influence of matrix time-dependent behaviour

on damage, *i.e.* the investigation of TDD, within woven PMCs above their glass transition temperature. Two main sub-objectives were investigated:

- **Verify the influence of time-dependent phenomena on translaminar fracture of woven-ply C/PPS laminates above the glass transition temperature.** This study enables to check how the matrix' time-dependent behaviour influences the translaminar failure of woven laminates through AE monitoring and a fracture mechanics approach using computations of the translaminar fracture toughness. Furthermore, two stacking sequences are used: AP laminates displaying a time-dependent mechanical behaviour and QI laminates having a limited time-dependent behaviour.

- **Track time-dependent damage development during creep in woven-ply C/PPS laminates above the glass transition temperature.** This study focuses on the detection of time-dependent damage development during creep tests within AP laminates by proposing a coupled characterization method. The main purposes are to verify if TDD occurs within the composite, to identify the different mechanisms involved and to characterize their evolution in real-time along with other time-dependent phenomena (*i.e.*, visco-elasto-plasticity and fibre bundle rotation). This study also enables to compare the relevance of the different monitoring tools in damage tracking.

CHAPTER 4 METHODOLOGY

This chapter details the strategy adopted to answer the main problem of this work, *i.e.* how does the matrix time-dependent behaviour influence the damage development within woven PMCs? The first section presents the studied material. The second section details the experimental set-up. Finally, the third section proposes two protocols to investigate time-dependent damage.

4.1 Material

The studied material is a 5-harness balanced satin weave (Figure 4.1) carbon fabric reinforced PPS. The 3K fibre bundles were made from T300 carbon fibres supplied by the company Toray. The fibre's features and properties are summarized in Table 4.1. The fibre and fabric mechanical properties are assumed to be elastic and temperature independent. Indeed, similar elastic moduli and strengths were evaluated between RT and 120 °C [5]. The PPS matrix used in this study (Fortron 0214) was supplied by the Ticona company. A few properties of the PPS matrix are summarized in Table 4.2. Those properties were determined by Aucher on the same material [5]. It should be noted that the glass transition temperatures T_g, the melting temperatures T_m and the degrees of cristallinity χ_c of PPS and 5HS C/PPS is about the same (Table 4.3). In this work, the tests are performed at 120 °C which is above the glass transition temperature of PPS in order to exacerbate the time-dependent behaviours.

Two stacking sequences are considered (Figure 4.2) in this study: a QI laminate (Figure 4.2a), whose thermo-mechanical behaviour is fibre-dominated; and an AP laminate (Figure 4.2b), whose response is matrix-dominated. The QI and AP laminated plates were manufactured by hot press consolidation (Dedienne Multiplasturgy) of 0.317 mm thick prepregs with a

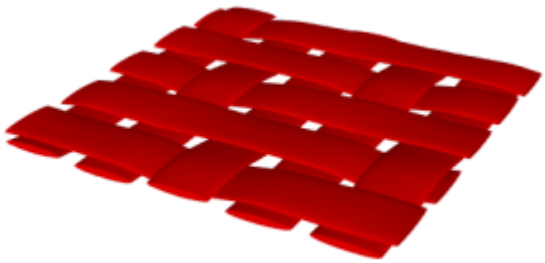

Figure 4.1 Illustration of a 5-harness satin weave (generated with TexGen).

Table 4.1 CF' features and mechanical properties [20, 103]

Properties	Value
Diameter (µm)	7
Density ($\mathrm{g\,cm^{-1}}$)	1.77
E (GPa)	230
$\sigma_r^{tension}$ (MPa)	3530
$\epsilon_r^{tension}$ (%)	1.5

Table 4.2 PPS matrix properties

	Properties	Value range	Ref.
Physico-chemical	T_g (°C)	90-97	[5, 104, 105]
	T_m (°C)	280-282	[5, 104, 105]
Mechanical at RT	E (GPa)	2.3-3.8	[5, 105]
	ν	0.36-0.38	[104, 105]
	$\sigma_r^{tension}$ (MPa)	90.3-93	[5, 105]
	$\epsilon_r^{tension}$ (%)	15	[5]
Mechanical at 120 °C	E (GPa)	0.34	[5]
	ν	-	-
	$\sigma_r^{tension}$ (MPa)	67	[5]
	$\epsilon_r^{tension}$ (%)	79	[5]

volume fraction of CF equal to 50%. The consolidation process was achieved at $310 \pm 15\,^{\circ}\mathrm{C}$ and 10 bars, as schematically shown in Figure 4.3.

200 mm long specimens were waterjet-cut from 600×600 mm^2 plates. The adopted specimen geometry is similar to the one proposed in [106, 107], as illustrated in Figure 4.4.

Table 4.3 Comparison of a few physico-chemical properties of PPS and 5HS C/PPS [5]

Properties	PPS	5HS C/PPS
T_g (°C)	97.1	95.4
T_m (°C)	279.5	279.7
χ_c (%)	26.8	26.7

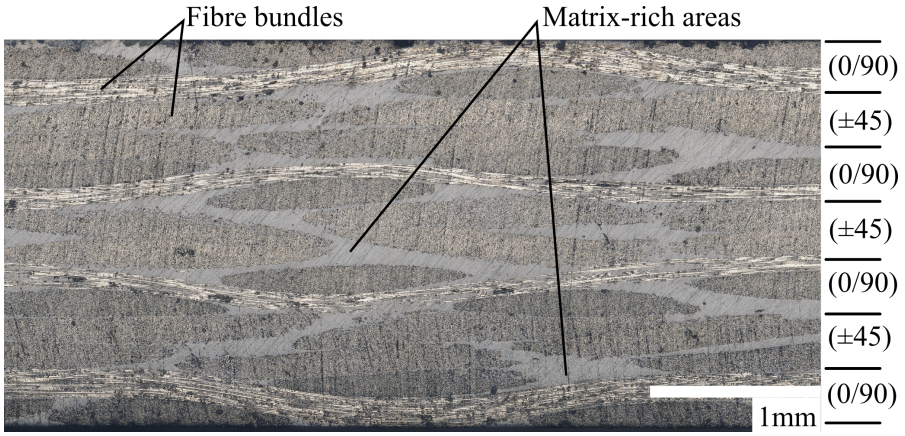

(a)

(b)

Figure 4.2 Edge observations of (a) QI and (b) AP laminates. Several matrix-rich areas are observed for both stacking sequences.

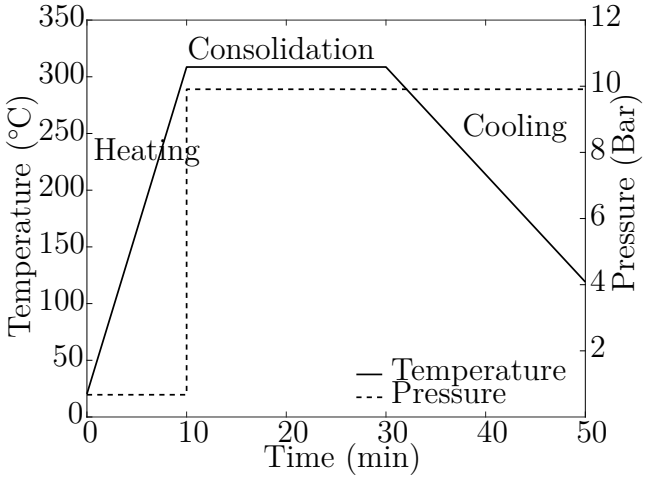

Figure 4.3 Manufacturing cycle for hot press C/PPS consolidated plates carried out by Dedienne Multiplasturgy. The consolidation process of seven 0.317 mm thick C/PPS prepregs was achieved at $310 \pm 15\,°C$ and 10 bars.

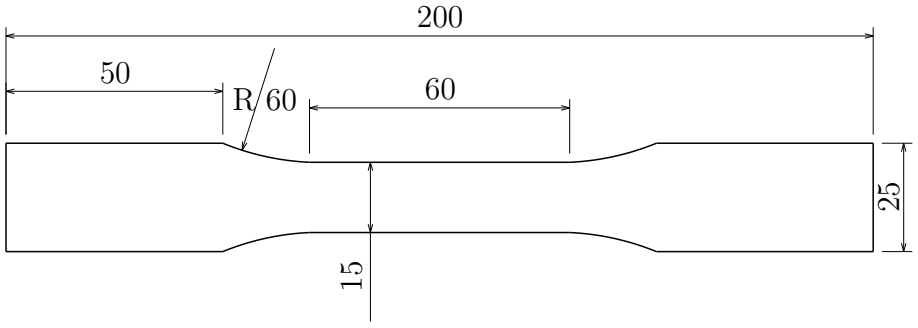

Figure 4.4 Specimen geometry. The dogbone specimens were waterjet-cut from plates. The specimen length, width and thickness were around 200, 15 and 2.3 mm, respectively.

4.2 Experimental setup

4.2.1 Mechanical testing

The mechanical tests were performed on a MTS 810 servo-hydraulic testing machine with a 100 kN load cell. Longitudinal strains were measured by means of a MTS 634.11F-25 blade-extensometer having a gauge length l_0 equal to 25 mm and a temperature range of -100–$175\,°C$.

The specimens were heated in a MTS 651 environmental chamber at $120\,°C$. The temperature sensor was near the gauge length but it was not in contact with the specimens. The temperature was hold during at least 30 minutes before each tests to obtain a homogeneous temperature within the gauge length. Figure 4.5 shows the variation of axial strain at 0 N during a temperature ramp for an AP specimen. The strain peaked and decreased after 5 minutes. The decrease was not explained. A longer heating time should result in a better stabilisation, but it would be time-consuming.

4.2.2 Acoustic emission monitoring

4.2.2.1 AE hardware - setup

Sensors

Micro80 (μ80) sensors were used in this study. μ80 are resonant sensors. Table 4.4 summarizes some of the characteristics of these sensors.

Two sensors were mounted to the specimens using PVC clamps (Wolfcraft microfix) and silicone grease (KF silicon grease 500). The distance between sensors d_{1-2} is set to 60 mm for all tests. This distance is a compromise between minimizing the AE waves attenuation and clutter.

Pre-amplifiers

The signal from sensors was amplified by 20 dB using 2/4/6 pre-amplifiers which include a

Table 4.4 Summary of μ80 sensor characteristics

Sensor	Frequency range (kHz)	Temperature range (°C)	Diameter x Height (mm x mm)
μ80	200-900	-65 to 177	10 x 12

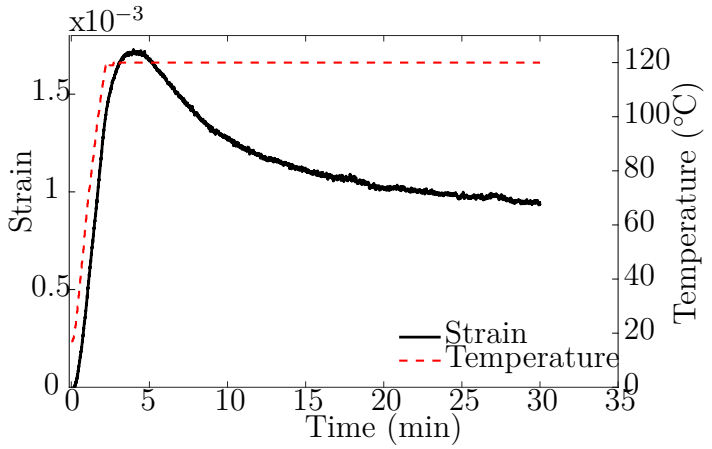

Figure 4.5 Axial strain variation at 0 N with an increasing temperature (20-120 °C) for AP 5HS C/PPS laminates. A 30 minutes heating time seems necessary before any test to reach a homogeneous temperature within the gauge length.

20-1200 kHz band-pass filter. The pre-amplifier gain was set to 20 dB to avoid any saturation of the sensors, though a 40 dB gain may have been better to increase the signal-to-noise ratio during the signal transport.

Acquisition card

A PCI-2 acquisition card was used for the simultaneous acquisition of two AE channels and two parametric channels.

4.2.2.2 AE acquisition parameters

The acquisition was done through the software AEwin vE4.70. The acquisition threshold was determined as the one for which no acoustic hit was detected during a 5-minute time period. Then, 3 dB were added to this threshold to obtain the acquisition threshold. This protocol was applied to AP and QI stacking sequences at ambient temperature and 120 °C. The higher threshold was considered for all configurations.

The set Peak Definition Time (PDT)/Hit Definition Time (HDT)/Hit Lockout Time (HLT) used in this study is the same as that used by Albouy et al [8] and was verified by visualizing a waveform obtained through Hsu-Nielsen pencil lead break source as a generation of an acoustic wave. The acquisition parameters are summarized in Table 4.5.

Table 4.5 Summary of the AE acquisition settings

Threshold		Analog filter		Waveform setup			Timing parameters		
Type	Value (dB)	Lower (kHz)	Upper (kHz)	Sample rate (MHz)	Pre-trigger (µs)	Length (k)	PDT (µs)	HDT (µs)	HLT (µs)
Fixed	45	100	1000	2-5	25-125	6	30	100	300

4.2.2.3 Location of events

Spatial filtering was achieved using a linear arrangement with two sensors. If a source mechanism generates a wave that reaches both sensors, the location of the AE source can be computed using the time between those two hits and the wave's velocity within the material. The wave's velocity is estimated beforehand using Hsu-Nielsen pencil lead break sources as a generation of repeatable acoustic waves following the protocol illustrated in Figure 4.6. The pencil lead breaks at 120 °C are performed while the temperature is greater than 100 °C after the opening of the thermal chamber. The wave's velocities for QI and AP specimens at 120 °C are summarized in Table 4.6. Those velocities are considered constant even when damage accumulates within the tested specimens.

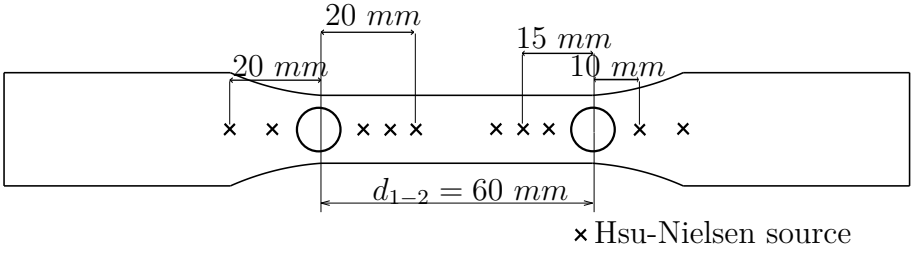

Figure 4.6 AE wave's velocity protocol. Hsu-Nielsen lead breaks are carried out at several locations to simulate AE waves. The velocity of the those waves are then determined based on the arrival times and the distances traveled.

Table 4.6 Wave's velocities within QI and AP 5HS C/PPS specimens at 120 °C

	QI	AP
AE wave's velocity ($\mathrm{m\,s^{-1}}$)	5000	3230

4.3 Experimental protocol

The main objective of this work was to investigate possible time-dependent damage (*i.e.*, influence of time-dependent behaviour on damage accumulation) within 5HS C/PPS laminates at 120 °C.

4.3.1 Fracture mechanics approach - Load-unload tests

Experimental set-up and conditions

The following test was developed to determine if the matrix time-dependent behaviour influences the translaminar failure of 5HS C/PPS laminates at 120 °C. Several tools and parameters were considered to investigate such time-dependency:

- strain and remote stress at break to investigate the time-dependency at the macroscopic scale,
- analyses of the fracture morphology to identify the different failure mechanisms,
- fracture toughness to study its possible time-dependency,
- AE monitoring as an in-situ damage monitoring tool. AE activity, via the cumulative AE absolute energy, was used as a substitute for DIC to track damage state within the laminates. The DIC set-up was not suitable to track the crack propagation (*e.g.*, low luminosity, low frame rate coupled with a mechanical test procedure resulting in a mainly unstable crack propagation). The AE analysis was based on spatially filtered AE events (*i.e.*, inside the 60 mm inter-sensor region as illustrated in Figure 4.7). The monitored AE hits at the origin of those AE events were not feature-based filtered.

The following tests were performed on Single Edge Notched (SEN) specimens. The specimen geometry is that introduced in Figure 4.4 with an additional notch, as illustrated in Figure 4.7. The SEN specimens were obtained by machining a side notch with a precision endless diamond wire saw having a radius of 0.11 mm. The notch length was chosen to obtain a ratio $\frac{a_0}{W} \approx 0.3$, a_0 being the initial notch length and W the specimen's width. Ratios ranged from 0.25 to 0.32 due to variability in the cutting process. The initial notch length was verified post-mortem using a caliper. Both QI and AP laminates are investigated.

The SEN specimens were subjected to different incremental force-controlled loading configurations, as shown in Figure 4.8:

- Load-unload (LU) at 5-50-500 N/s

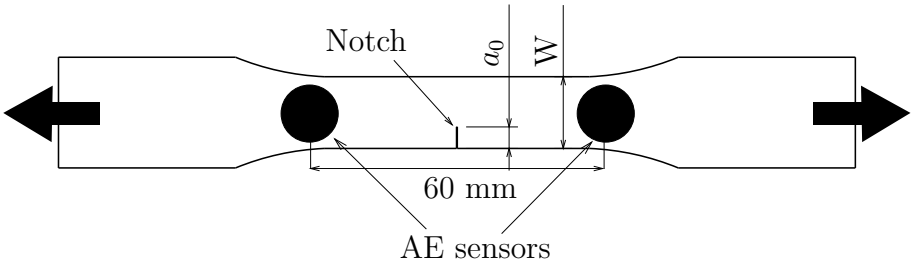

Figure 4.7 SEN specimen geometry. The notches were manufactured with a precision endless diamond wire saw. The notch length to width ratio was about 0.3. The specimen length, width and thickness were around 200, 15 and 2.3 mm, respectively. The two AE sensors were PAC μ80 sensors and were used to spatially filter the AE events.

- Load at 50 N/s - 15 minutes creep - unload at 50 N/s (LcU)
- Load at 50 N/s - 15 minutes creep - unload at 50 N/s - 15 minutes recovery (LcUr)

The LU condition was used to study the influence of loading rate on damage while the LcU and LcUr conditions were used to investigate the influence of creep periods on fracture mechanisms. The solicitation rate for LcU and LcUr configurations was fixed to 50 N/s for both stacking sequences. It was a compromise between minimizing the machine overshoot and minimizing creep effects during the loading phase. Creep times of 15 minutes were a good compromise between test duration and the representativeness of the influence of the viscoelastic behavior on crack growth. Albouy [32] observed that 90 to 95% of the full creep strain occurred within 15 minutes in the case of 24 h creep tests for unnotched specimens of the same material under the same temperature. As a result, a creep time of 15 minutes was assumed long enough to make a significant difference on the influence of time-dependent effects on damage in the fracture process zone around the crack tip. The load levels were computed based on the ultimate load determined from force-controlled monotonic tensile tests. The ultimate loads are about 5400 N and 3400 N for QI and AP specimens, respectively. Table 4.7 summarizes the testing configurations for AP and QI stacking sequences.

Determination of fracture toughness

G_I can be evaluated from Equation (2.14) using Equations (2.7) and a function $f(a/W)$ proposed by Gross and Brown [108, 109] for SENT specimens:

$$f(a/W) = 1.122 - 0.231(a/W) + 10.550(a/W)^2 \\ -21.710(a/W)^3 + 30.382(a/W)^4. \tag{4.1}$$

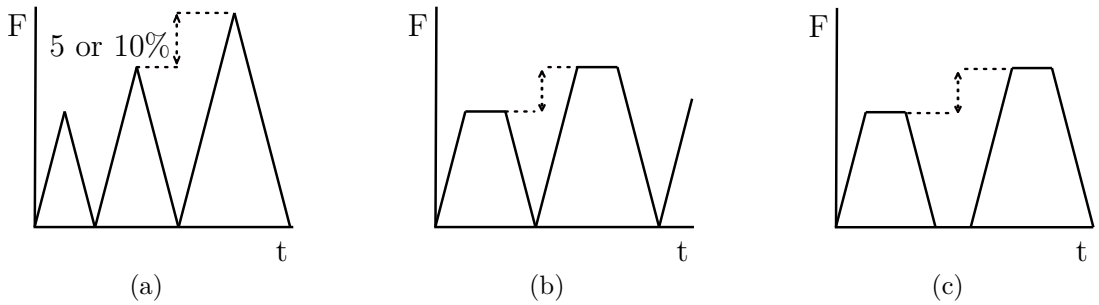

Figure 4.8 Illustration of the different incremental tensile loading conditions: (a) Load-unload at 5/50/500 N/s, (b) Load at 50 N/s - 15 minutes creep - unload at 50 N/s and (c) Load at 50 N/s - 15 minutes creep - unload at 50 N/s - 15 minutes recovery.

Table 4.7 Summary of tests carried out on QI and AP laminates for each loading configuration

	Loading	# of specimens	B[1] (mm)	W[1] (mm)	Notch ratio[2]	Load increment
QI	LU5	3	2.26	16.27	0.292-0.313	10%
	LU50	3	2.31	16.27	0.289-0.317	10%
	LU500	3	2.25	16.27	0.288-0.305	10%
	LcU50	-	-	-	-	-
	LcUr50	3	2.16	16.27	0.245-0.258	5%
AP	LU5	-	-	-	-	-
	LU50	2	2.33	14.81	0.307-0.317	5%
	LU500	-	-	-	-	-
	LcU50	3	2.36	14.79	0.309-0.318	5%
	LcUr50	3	2.34	14.85	0.304-0.309	5%

[1] Mean values
[2] Min-max values

Its critical value, G_{Ic}, can be obtained from the critical stress causing crack extension, σ_c^{remote}. This method was used as a first approximation.

Though the method to determine ΔJ was developed for elastic-plastic materials under cyclic loading, a similar approach was used in this work to evaluate the ΔJ-like integral for visco-elasto-plastic materials under incremental load-unload solicitations. Thus, for a visco-elastic-plastic material subjected to a cyclic loading, Equation (2.19) becomes:

$$\Delta J = \Delta J_{rev} + \Delta J_{irrev} = \eta_{rev} \frac{\Delta A_{rev}}{Bb} + \eta_{irrev} \frac{\Delta A_{irrev}}{Bb}, \tag{4.2}$$

where ΔA_{rev} and ΔA_{irrev} can be evaluated from the load-LLD curves, as illustrated in Figure 4.9. It should be noted that no crack closure phenomena, as illustred in Figure 2.29b, were observed during the tests. Furthermore, only the irreversible component was investigated because the component J_{el} is only significant at the onset of mechanical loading, whereas the component J_{pl} becomes prominent throughout the test, according to Chabchoub et al. [101]. As a first approximation, η_{irrev} was considered to be equal to η_{pl} (Table 4.8). This value was determined by Chabchoub et al. [101] for the same material, the same geometry and for identical loading conditions.

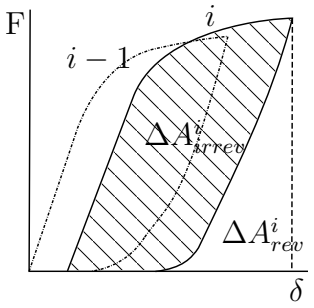

Figure 4.9 Typical load-LLD curve for a visco-elasto-plastic material subjected to an incremental load-unload test with no crack closure effect. ΔA_{irrev} is the energy dissipated during a cycle, while ΔA_{rev} is the reversible work.

Table 4.8 Values of η_{el} and η_{pl} evaluated for C/PPS AP SEN dogbone specimens subjected to tensile loading at 120 °C [101].

η_{el}	η_{pl}
0.8674	0.7718

4.3.2 Damage mechanics approach - Cyclic Creep (CC) tests

Experimental set-up and conditions

The following test was developed to monitor any possible time-dependent damage occurring within the laminates at 120 °C, as well as to investigate other phenomena such as viscoelasticity, viscoplasticity and fibre bundle rotation. The purpose of this test is to provide a better insight into the time-dependent damage accumulation via the investigation of the conjoint development of all the phenomena stated above. Ultimately, the purpose is to separate/identify each mechanism. Several tools were used conjointly in order to qualify and quantify in-situ damage accumulation:

- AE monitoring as an in-situ tracking of damage events during creep stages. The AE analysis was based on spatially filtered AE events inside a 15 mm centered region between the two sensors. The monitored AE hits used for this analysis were filtered during the acquisition based on the counts $n > 3$,
- edge replica as a quantification of damage within the specimens and comparison with AE events. The edge replicas were conducted on polished edges of the specimen at different times during the test. The area covered by the edge replication was about 2×15 mm^2,
- stiffness-based damage variable as a detection of macroscopic damage and its effect on elastic properties,
- ex-situ XμCT to observe the final damage state within the specimens and verify the assumption of the representativeness of the damage state analyzed on the specimens' edge from edge replications.

CC tests were prioritized on AP C/PPS laminates at 120 °C due to its highly time-dependent behaviour at macroscopic scale compared to the one observed in QI laminates, as stated by Albouy [6]. Therefore, AP specimens are expected to display time-dependent damage development. However, CC tests should be performed on other stacking sequences (*e.g.*, QI) in the future to verify any possible time-dependent damage development. The CC test set-up is illustrated in Figure 4.10.

The thermo-mechanical test procedure is illustrated in Figure 4.11. The temperature was increased from RT to 120 °C at zero load and held during 30 min to obtain a homogeneous temperature within the specimen before mechanical load was applied. First of all, the specimen was subjected to a LU cycle at the desired stress σ_0 in order to have a reference damage

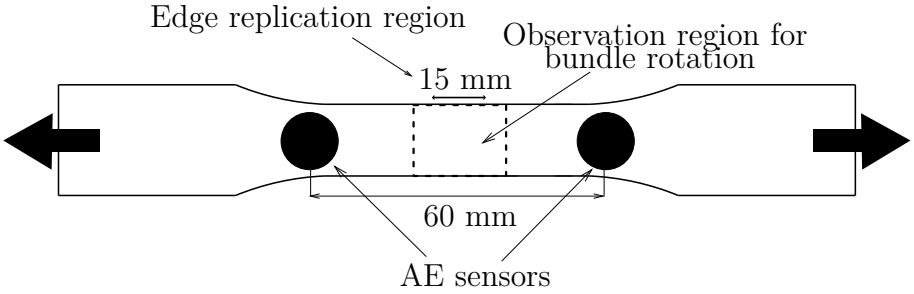

Figure 4.10 Illustration of the monitoring set-up during the CC tests. Two μ80 sensors were used to monitor AE events inside a 15 mm centered region. Cracking was characterized at the edges of this region through edge replications using vinylpolysiloxane. Damage development was also monitored using a stiffness-based damage variable. Finally, fibre bundle rotation was tracked at the surface of this region using a camera.

state $D(\sigma_0, t)|_{t=0}$. The first cycle was followed by five creep cycles with increasing holding time summarized in Table 4.9 and a last LU cycle. Each cycle was separated by a recovery step. The recovery holding time was either equal to 1 h or three times the duration of the previous creep step. In addition, half of the tested specimens were held at 100 N (around 3 MPa) during 1 h between the unloading and recovery steps in order to carry out edge replications. Edge replications were performed at a non-zero force to avoid complete crack closures. Before applying vinylpolysiloxane on one edge of the specimens, the temperature was decreased to $\sim$50 °C with the thermal chamber open. The temperature was then increased to 120 °C at the beginning of the recovery step. Finally, fibre bundle rotation was estimated from pictures taken at the end of creep and recovery stages. The loading rate of the different loading and unloading steps was set to 50 N/s. It was a compromise between the minimization of time-dependent phenomena and minimization of potential overshot during the loading steps.

Three stress levels were investigated: 40, 60 and 100 MPa. The determination of these stress levels is described in Section 6.1. Two specimens were tested for each stress level: one using the edge replications technique and the other without edge replications.

Table 4.9 Creep time and recovery time for each cycle during a CC test.

cycle #	0	1	2	3	4	5	6
t_{creep} (h)	0	0.25	0.5	0.75	1	8	0
$t_{recovery}$ (h)	1	1	1.5	2.25	3	24	1

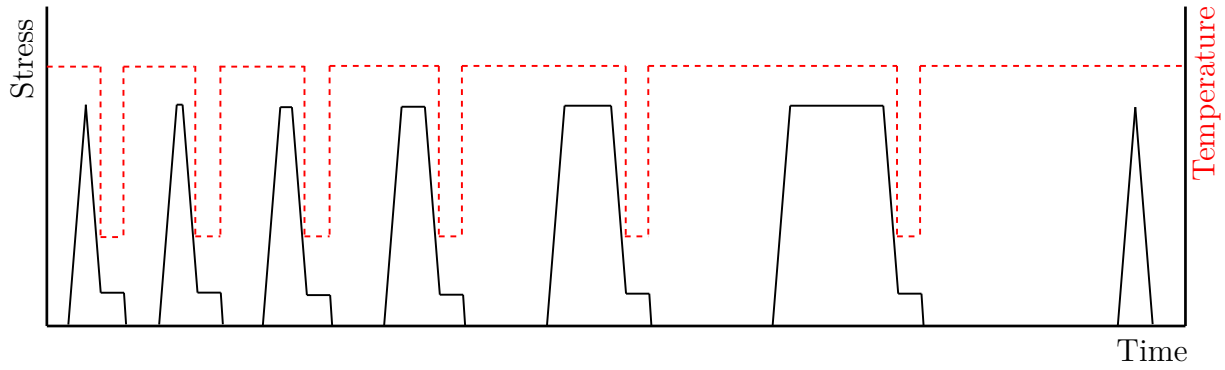

Figure 4.11 Test procedure for CC tests. The temperature was held at 120 °C during 30 minutes before the first cycle. The loading rate was 50 N/s. The first cycle was supposed to result in a damage state $D(\sigma_0, t)|_{t=0}$, so damage occurring during further cycles with creep steps should be time-dependent damage. Recovery steps lasted at least three times longer then creep steps. Half of the specimens were subjected to a hold stages at 100 N during 1 h between creep and recovery steps to carry out edge replications at 50 °C before re-heating the specimens at 120 °C. The other half was subjected to a constant temperature at 120 °C.

Edge crack density determination

Specimens edges were manually polished before the tests. The sequence of polishing papers was conventional (*i.e.*, P400/P800/P1200/P2500/P4000) and water was used regularly to remove residues. The microscopic observations were obtained with a Keyence VHX-5000 optical microscope. The edge replications were carried out using vinylpolysiloxane on a 15 mm centered area at one edge of the specimens with a load at 100 N and temperature ∼50 °C.

Two methods were used to determine the edge crack density from edge replica:

- crack count density method: the microscopic observation of the edge is sliced into 7 parts along the thickness, which represents about a ply by slice. Then, two lines are drawn per slice to obtain cracks from weft and warp bundles. Each intra-bundle crack intersecting a line is used to compute the crack count density over the replica's length. Figure 4.12 illustrates the slicing of a microscopic observation of a edge replica.

- cracked surface density method: the microscopic observation is binarized and subjected to a morphological image process, which consists of an erosion followed by a dilation using the same structuring element (rectangle [4px 2px]). Figure 4.13 shows the input (Figure 4.13a) and the output (Figure 4.13b) of a small area. Then, the cracked surface density is computed as the ratio of pixels from cracked region to total pixels. The software used was Matlab.

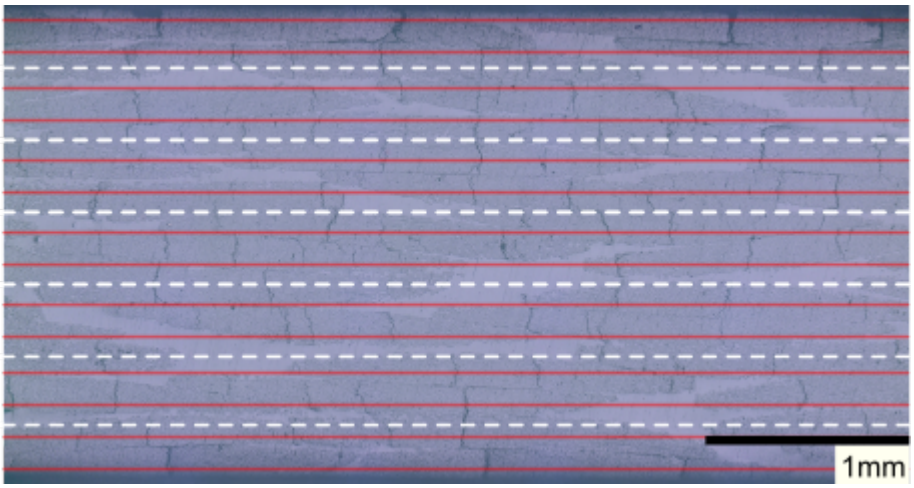

Figure 4.12 Illustration of the crack count density method. This method is based on a ply-level separation of the microscopic observations followed by a manual counting of the intersection of two lines per ply with intra-bundle cracks.

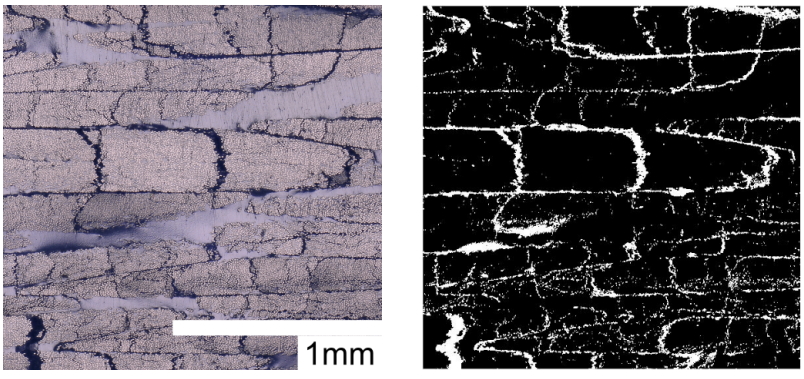

(a) (b)

Figure 4.13 Illustration of the cracked surface density method: (a) input and (b) output. This method is an automatic method based on thresholding and morphological image process. The density is then computed as a pixel ratio. This method detects intra- and inter-bundle cracking.

Stiffness and macroscopic damage variable determination

A macroscopic damage variable d was computed using the specimen's axial stiffness as per [110]:

$$d = 1 - \frac{E_i}{E_0}, \tag{4.3}$$

with E_i being the axial stiffness of the i^{th} load and E_0 being the initial stiffness.

The axial stiffness was determined by the same method as that of Bassery [20]. This method consists in finding the elastic domain by means of the maximum of the coefficient of determination R^2 (Figure 4.14a) of a linear regression intersecting with the origin (Figure 4.14b).

Evaluation of fibre bundle rotation

The fibre bundle rotation was determined using the angle tool of ImageJ applied to different images of the centered region of the specimen's surface. Several lines were drawn using a permanent marker to facilitate the measurements. The rotation angles were then evaluated based on the initial bundle orientation (*i.e.*, the bundle orientation after heating but before loading) as illustrated in Figure 4.15. The images were taken using a 2.3 Mpixels FLIR Grasshopper3 (GS3-U3-23S6M-C) camera including a Sony IMX174 CMOS sensor.

XμCT

The ex-situ XμCT (RX solutions EasyTom130 microtomograph) observations were performed by Institut Clément Ader on the specimens that were used for the edge replications. The XμCT system was a RX solutions EasyTom130 microtomograph and the software was X-Act CT. A continuous rotation with reference images and two main settings were used. The first one consisted in having the entire specimen width in the field of view during the rotation, which resulted in a resolution $\sim$16 µm. This setting was applied to each stress level. The second setting consisted in having half of the specimen width in the field of view, which resulted in a resolution around 7 µm. This configuration was only used for the 100 MPa stress level. Therefore, the comparison focuses on the observations from the first setting. Table 4.10 summarizes a few parameters regarding each XμCT observation.

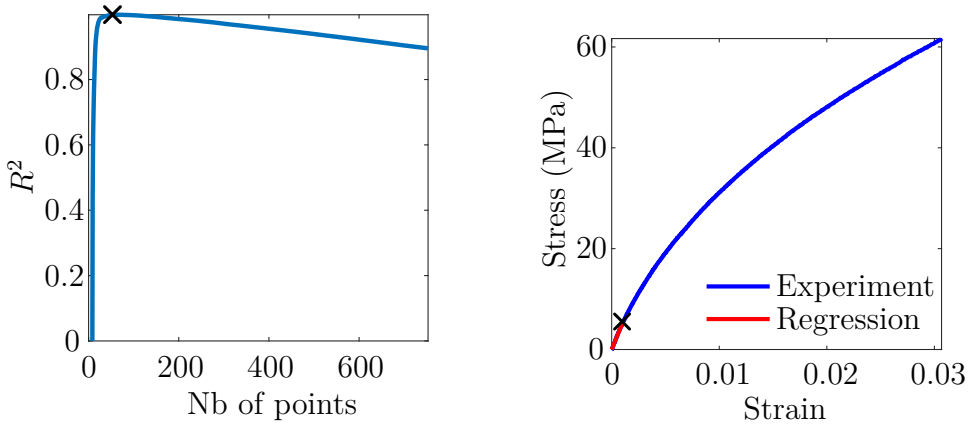

(a) (b)

Figure 4.14 Determination of the elastic domain based on (a) the variation of R^2 with the number of points used for the linear regression intercepting the origin and (b) illustration of the resulting elastic domain on a stress-strain curve

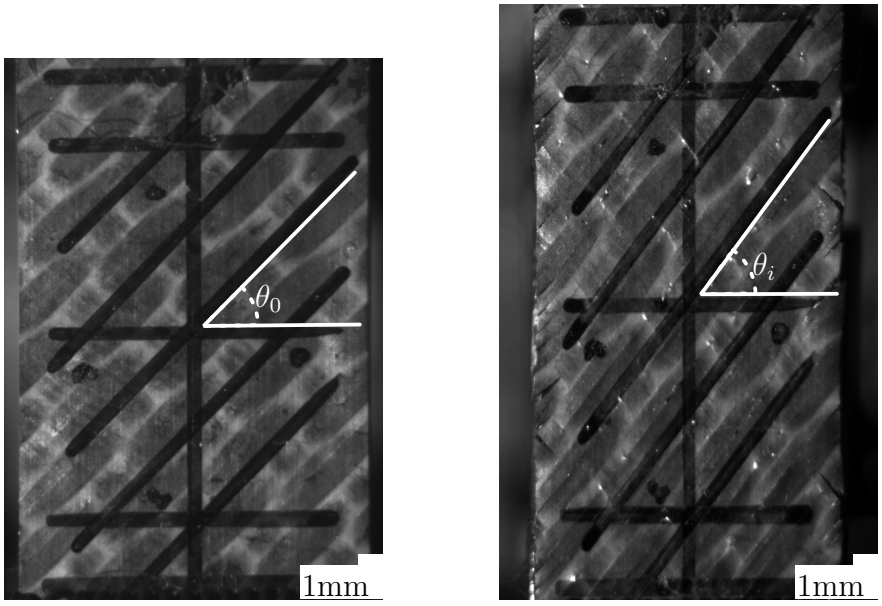

(a) (b)

Figure 4.15 Illustration of the fibre bundle rotation determination: (a) initial image and (b) image taken during loading.

Table 4.10 Settings of XμCT observations (RX solutions EasyTom130 microtomograph)

Stress level	40 MPa	60 MPa	100 MPa	
	Setting 1	Setting 1	Setting 1	Setting 2
# of revolutions (width)	1	1	1	2
# of revolutions (height)	4	2	4	1
Total # of images	3072	2400	3072	3296
Volume height (mm)	∼60	∼30	∼60	∼13
Volume diameter (mm)	∼16	∼16	∼16	∼15
Voxel size (µm)	∼16	∼16	∼16	∼7
Tube voltage (kV)	70	70	70	70
Tube current (µA)	228	228	228	114

CHAPTER 5 Influence of time-dependent phenomena on translaminar fracture of woven-ply C/PPS laminates above the glass transition temperature

This chapter presents and discusses the results of the first experimental campaign, which is based on the study of possible influence of the matrix time-dependent behaviour on the translaminar fracture in tension of AP and QI 5HS C/PPS laminates at 120 °C. The experimental protocol was detailed in Section 4.3.1.

5.1 Results

5.1.1 Quasi-isotropic laminates

5.1.1.1 Stress-strain macroscopic response

Figure 5.1 shows the stress-strain curves for SEN QI specimens subjected to LU (5-50-500 N/s) and LcUr (50 N/s) loadings. This figure shows that QI laminates exhibit a slightly non-linear behaviour, probably due to slight plasticity and progressive damage development as the applied stress approaches the ultimate strength [98]. Furthermore, it appears that QI specimens submitted to the LcUr condition undergo some viscoelastic, viscoplastic and/or time-dependent damage phenomena.

Figure 5.2 shows the remote stress and strain at failure, σ_r^{remote} and ϵ_r respectively, for the LU (5-50-500 N/s) and LcUr (50 N/s) loading conditions. Figure 5.2a suggests that σ_r^{remote} for specimens subjected to loading LU500 is slightly higher than those obtained for specimens subjected to loadings LU5 and LU50. In addition, σ_r^{remote} obtained for loading LcUr50 might be higher than those resulting from other loadings due to its slightly lower notch ratio. On the contrary, Figure 5.2b shows that ϵ_r is insensitive to both loading rate and creep stages.

Table 5.1 summarizes the number of cycles to failure of all tested specimens for the different loading conditions in the case of QI specimens. It can be seen that the loading configuration does not influence significantly the number of cycles to failure, even for different load increments.

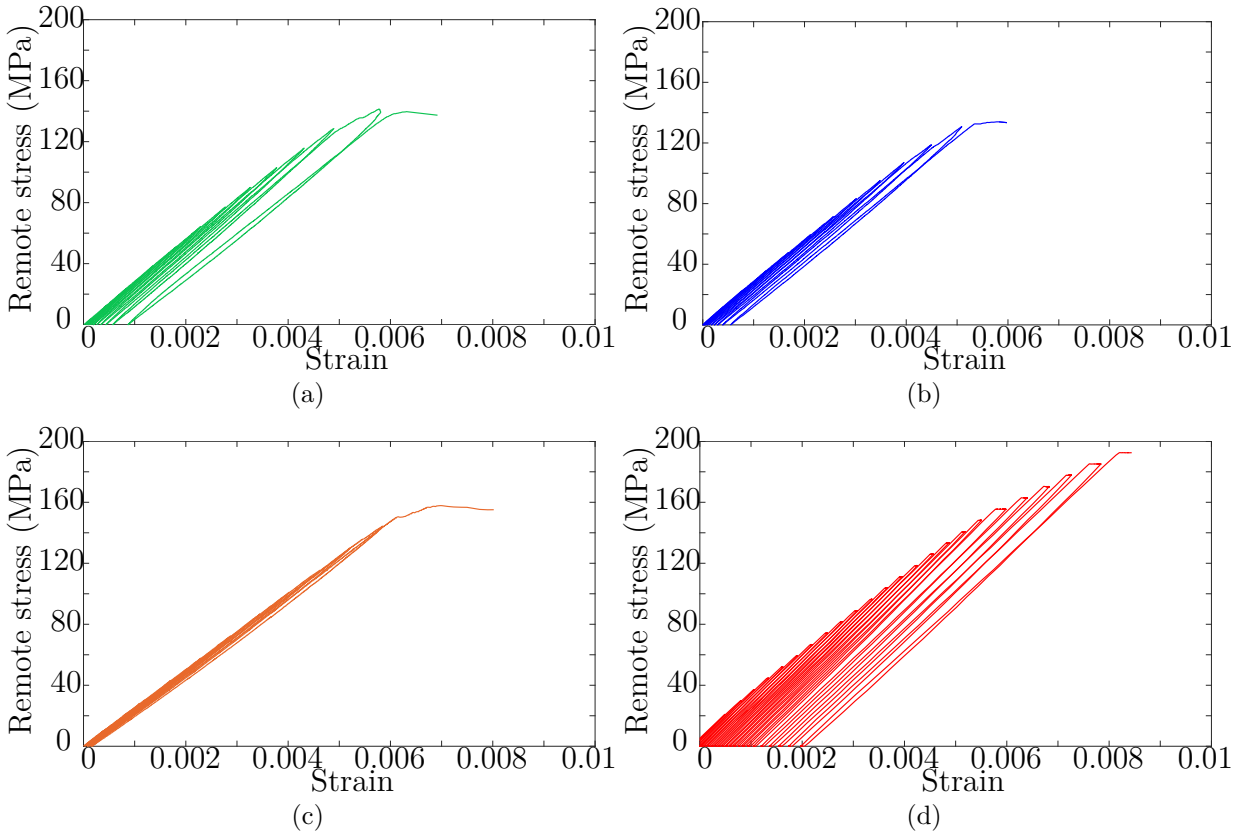

Figure 5.1 Typical stress-strain curves for QI SEN specimens subjected to various test conditions at 120 °C: (a) LU5, (b) LU50, (c) LU500 and (d) LcUr50. QI specimens display a slightly non-linear behaviour. However, the inelastic strains remain relatively small. The LcUr50 tests exhibit creep strain and some recovered strain. Those specimens might undergo some viscoelastic, viscoplastic and/or time-dependent damage phenomena.

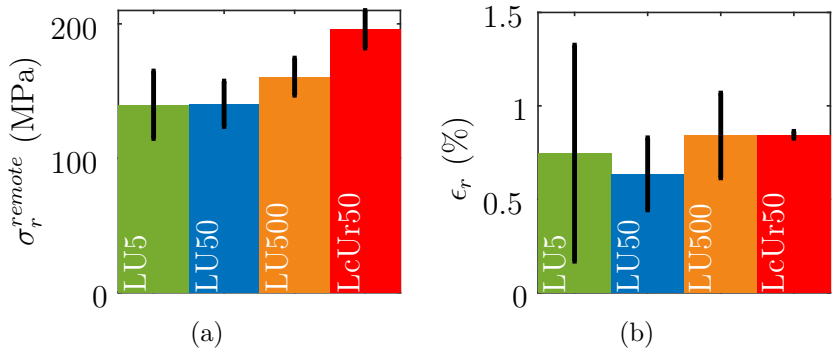

Figure 5.2 (a) Remote stress and (b) strain at failure of QI SEN specimens subjected to LU5/50/500 and LcUr50 test conditions at 120 °C (the error bars represent the 95% confidence interval). The LU500 test configuration has a slightly higher σ_r^{remote} than those from the LU5 and LU50 test conditions. The higher σ_r^{remote} for the LcUr50 loading might be due to the lower notch ratio more than a time-dependent effect. ϵ_r is not time-dependent.

5.1.1.2 Fracture morphology and strain energy release rate

Figure 5.3 shows the failure surface of a representative QI specimen. This crack grows self-similarly (*i.e.*, crack propagation occurs in the plane of the initial notch), resulting in an opening mode failure, as illustrated in Figure 5.3a. The main damage mechanisms involved by this configuration are intra-bundle transverse cracking and breakage of 0° and ±45° bundles. Intra-bundle cracking is not limited to the crack path vicinity, as shown in Figure 5.3b. Furthermore, it seems that no extensive delamination can be observed while some fibre bundle pull-out can be observed in Figure 5.3c, especially at the edges of ±45° oriented plies due to edge effects. The main fracture mode is therefore translaminar. It also seems that there is no visible qualitative difference in the fracture morphology between the different loading conditions, suggesting no significant influence of time-dependent phenomena on failure mechanisms.

Figure 5.4 displays the critical strain energy release rate, G_c for each configuration. The LEFM framework was considered here as a first approximation. These values were computed following Section 4.3.1 and using the maximum stress for each test by assuming: *i*) that no prior crack extension occurred and *ii*) that the QI specimens had a macroscopically quasi-isotropic behavior. Figure 5.4 shows that G_c values exhibit no significant difference between the loading conditions. These results suggest that the influence of time-dependent phenomena on G_c is negligible in QI specimens, whose macroscopic failure mode is fibre-dominated.

Table 5.1 Number of cycles to failure for the different loading configurations in the case of QI specimens

Configuration	Load increment	Number of cycles to failure		
		# 1	# 2	# 3
LU5	10%	11	12	11
LU50	10%	10	12	12
LU500	10%	12	11	12
LcUr50	5%	26	25	26

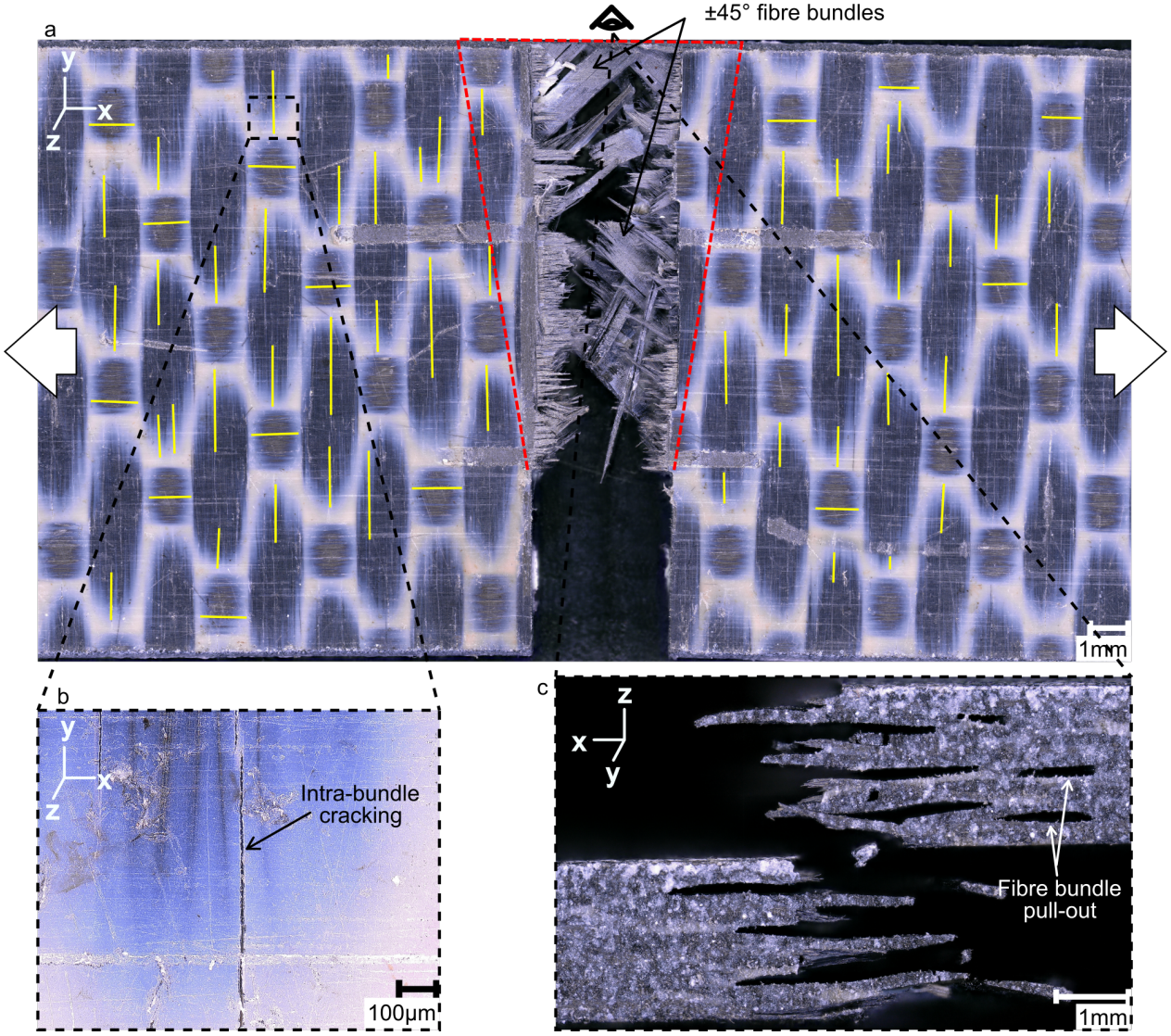

Figure 5.3 Microscopic observations of (a) the top view, (b) a secondary intra-bundle cracking and (c) the edges of a QI SEN C/PPS specimen subjected to LU500 at 120 °C (the red dot line is an indication of the extent of the fracture process zone and the solid yellow lines indicate secondary intra-bundle cracking). The crack grew in a self-similar manner resulting in a mode I failure. The main damage mechanisms involved are intra-bundle cracking and breakage of bundles. The failure is translaminar at the macroscopic scale. No difference in fracture morphology was observed between the different loading conditions.

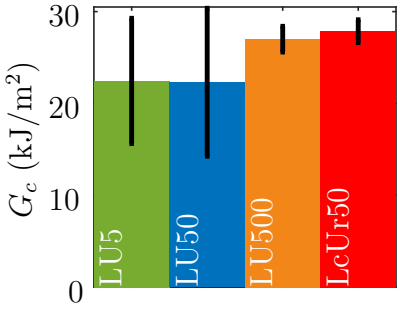

Figure 5.4 Approximation of the critical strain energy release rate G_c for QI SEN specimens subjected to LU5/50/500 and LcUr50 test conditions at 120 °C (the error bars represent the 95% confidence interval). Those values were computed assuming that no prior crack extension occurred before maximum stress, and that the QI specimens exhibited a macroscopically isotropic behaviour with limited inelastic deformation. The figure shows that G_c is not statistically affected by the loading conditions. This observation suggests that the influence of time-dependent phenomena on G_c is negligible in QI specimens.

5.1.1.3 AE activity

Figure 5.5 shows the cumulative events per loading cycle as a function of the maximal remote stress reached during each cycle for the LU5, LU50 and LU500 test configurations. The discontinuous symbols correspond to whole sets of experimental data points, while the continuous lines are exponential regressions. This figure suggests that the higher the solicitation rate, the slower the AE activity as a function of the remote stress is. However, this trend is not that obvious between the LU5 and LU50 configurations due to data dispersion in the LU5 data set. This tendency should be confirmed by additional tests with complementary techniques.

Figure 5.6 reports the AE activity for the LcUr test configuration for QI laminates. This figure shows that a significant amount of AE events appeared during the high stress level creep stages.

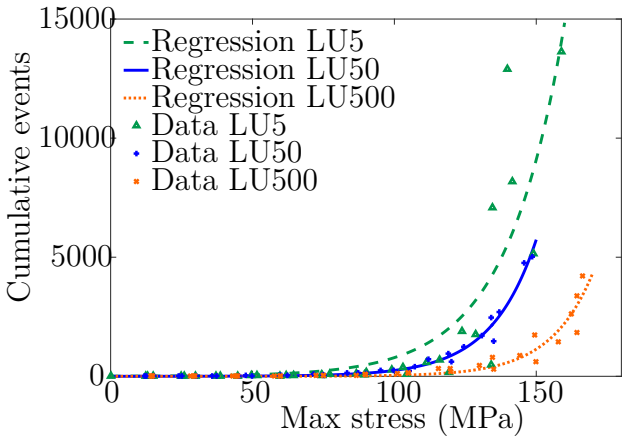

Figure 5.5 Cumulative events for QI SEN specimens subjected to LU5/50/500 test conditions at 120 °C. The symbols correspond to whole sets of experimental data points, while the continuous lines are exponential regressions. It appears that higher solicitation rates lead to slower AE activity as a function of the remote stress. This tendency is less obvious between the LU5 and LU50 test conditions.

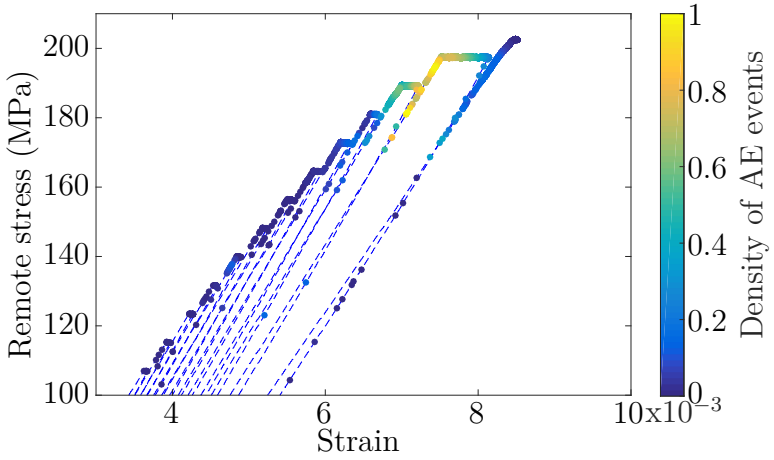

Figure 5.6 Density of AE events occurring during a LcUr50 test at 120 °C. It appears that a significant amount of AE events occurred during the creep steps for high stresses. These events might result from time-dependent damage.

5.1.2 Angle-ply laminates

5.1.2.1 Stress-strain macroscopic response

Figure 5.7 reports the stress-strain curves for SEN AP specimens subjected to LU50, LcU50 and LcUr50 loading conditions. AP laminates exhibit a visco-elasto-plastic behaviour promoted by the time-dependent behaviour of the PPS matrix at temperatures higher than its T_g, similarly to what was observed by Albouy [32] in unnotched specimens.

Figure 5.8 shows the influence of loading conditions on both the remote stress and strain at failure. The figure suggests that σ_r^{remote} and ϵ_r do not seem to be significantly influenced by time-dependent phenomena.

Table 5.2 summarizes the number of cycles to failure of all AP specimens for the different loading conditions. It appears that the loading configuration does not influence significantly the number of cycles to failure.

5.1.2.2 Fracture morphology and strain energy release rate

Figure 5.9 illustrates the fracture and damage mechanisms occurring within SEN AP specimens. As shown in Figure 5.9a, it appears that the crack does not grow self-similarly, contrary to what was observed in QI specimens. The crack seems to propagate along the ($\pm 45°$) bundles leading to a mixed-mode I-II (opening-shear) failure, as already observed in the same material [99, 101]. Figures 5.9a and 5.9d show that failure occurred after an extensive delamination and meta-delamination leading to fibre bundles pull-outs. Thus, this experimental configuration does not lead to a pure translaminar failure, which is accompanied by damage mechanisms associated with interlaminar failure. Many secondary intra-bundle cracks (Figure 5.9b), as well as some inter-bundle/interfacial cracks (Figure 5.9c) away from the main crack's vicinity, are observed, hence revealing a large damaged zone around the

Table 5.2 Number of cycles to failure for the different loading configurations in the case of AP specimens

Configuration	Load increment	Number of cycles to failure		
		# 1	# 2	# 3
LU50	5%	23	22	-
LcU50	5%	20	23	21
LcUr50	5%	21	22	22

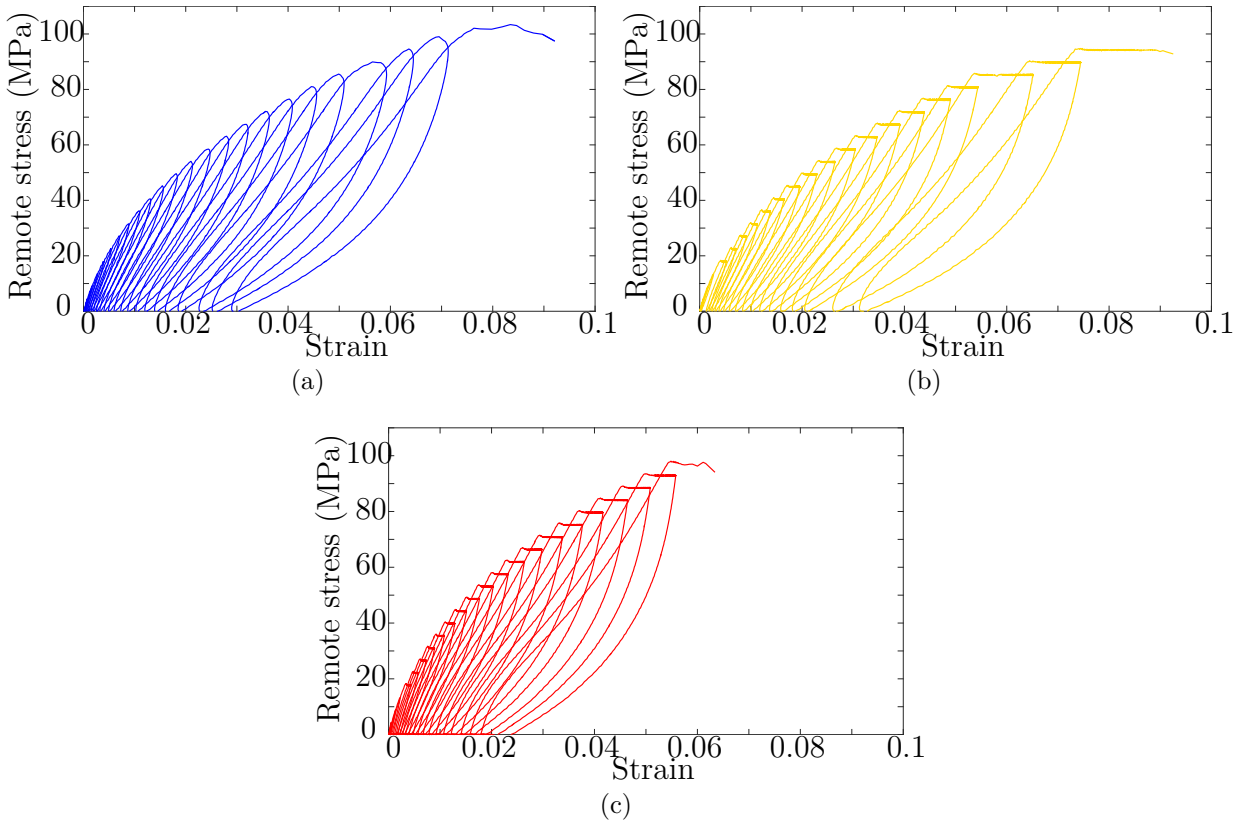

Figure 5.7 Typical stress-strain behaviour for AP SEN specimens subjected to various test conditions at 120 °C: (a) LU50, (b) LcU50 and (c) LcUr50. AP specimens display a highly visco-elasto-plastic behaviour.

crack. Furthermore, no significant difference was observed on the fracture morphology between the different loading conditions, suggesting no substantial influence of time-dependent phenomena on the failure mechanisms at the macroscopic scale.

Figure 5.10 represents the cumulative ΔJ_{irrev} evolution as a function of the cumulative AE absolute energy, for the different loading conditions. The symbols correspond to the whole experimental data sets, for each test, while the continuous lines are exponential regressions. The irreversible component ΔJ_{irrev} was determined at the end of each cycle (excluding the last cycle) using the method defined in Section 4.3.1 and a corrected uncracked ligament length b' to account for the crack 45° orientation, such as $b' = \frac{b}{cos(\frac{\pi}{4})}$. Complete self-similarity of a fracture process is hardly ever found experimentally in fiber-reinforced polymer laminates. Equation 2.19 was already used to compute the fracture toughness during non-self-similar propagation [99, 111]. Therefore, Equation 4.2 is assumed valid to calculate a J-like parameter as a first approximation in order to compare the different loading configurations, regardless the crack propagation path (self-similar or not self-similar). In the present work,

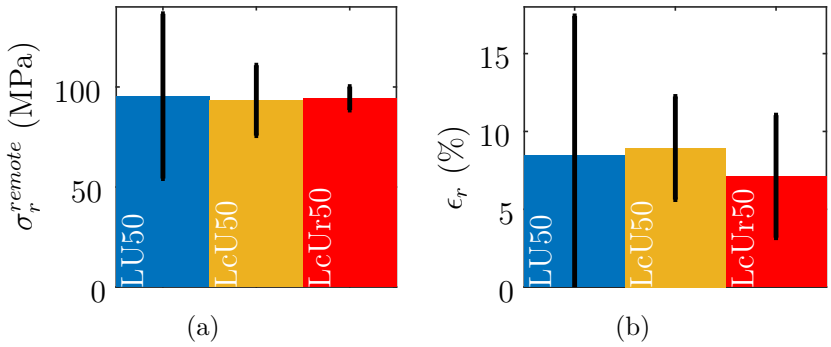

Figure 5.8 (a) Remote stress and (b) strain at failure of AP SEN specimens subjected to various test conditions at 120 °C (the error bars represent the 95% confidence interval). This figure suggests that the ultimate failure is not influenced by time-dependent phenomena.

the computation of ΔJ is based on the computation of the energy dissipated during a cycle. However, the theoretical validity of this approach should be confirmed. Figure 5.10 suggests that the data dispersion is quite significant, especially for LcU tests, hence hindering the time-dependent phenomena influence on ΔJ_{irrev}. However, an emerging trend can be guessed from the early stage of the test. ΔJ_{irrev} values computed from the LcUr configuration are higher than those extracted from the LU configurations, while ΔJ_{irrev} values computed from the LcU configurations are positioned between those extracted from LU and LcUr loading cases.

5.1.2.3 AE activity

Figure 5.11 shows the cumulative events and cumulative absolute energy per cycle as a function of the maximal remote stress during each cycle. Figure 5.11a shows that the LU load configuration results in lower amount of AE events than that of the LcU and LcUr loading conditions for stresses higher than 60 MPa. However, the same conclusion is not immediate for stresses close to ultimate failure due to data dispersion. This dispersion could result from a failure mechanism that is not purely translaminar (see Section 5.1.2.2). These results suggest that there is more damage accumulation in specimens subjected to creep stages. However, conclusions can hardly be drawn about the criticality of damage depending on the loading conditions because there is no significant difference in the evolution of the cumulative absolute energies (see Figure 5.11b).

Figure 5.12 shows a similar approach except that the AE activities were separated during the loading and creep phases. A larger number of events are involved during the creep stages, when compared to the amount of events appearing during the loading phases (Figure 5.12a). This observation suggests that significant time-dependent damage appears during

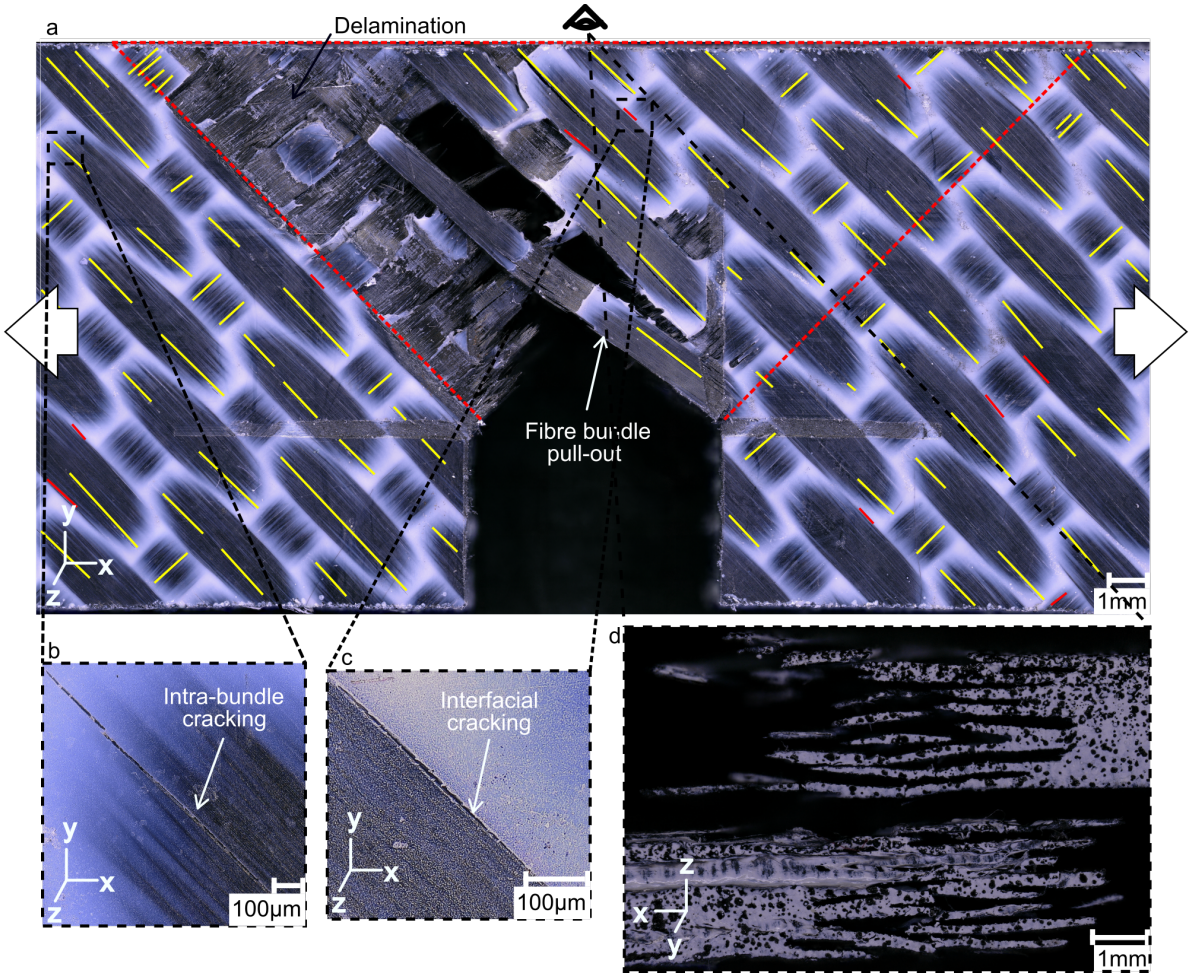

Figure 5.9 Microscopic observation of (a) the top view, (b) a secondary intra-bundle (continuous yellow line) and (c) secondary inter-bundle/interfacial cracking (continuous red line), as well as (d) the edges of an AP SEN C/PPS specimen subjected to LU50 at 120 °C (the red dot line is an indication of the extent of the fracture process zone). The crack path seems to follow the ±45°) bundles leading to a mixed-mode I-II. An extensive delamination appeared during failure resulting in mixed translaminar-interlaminar failure. No difference in fracture morphology were observed between the different loading conditions.

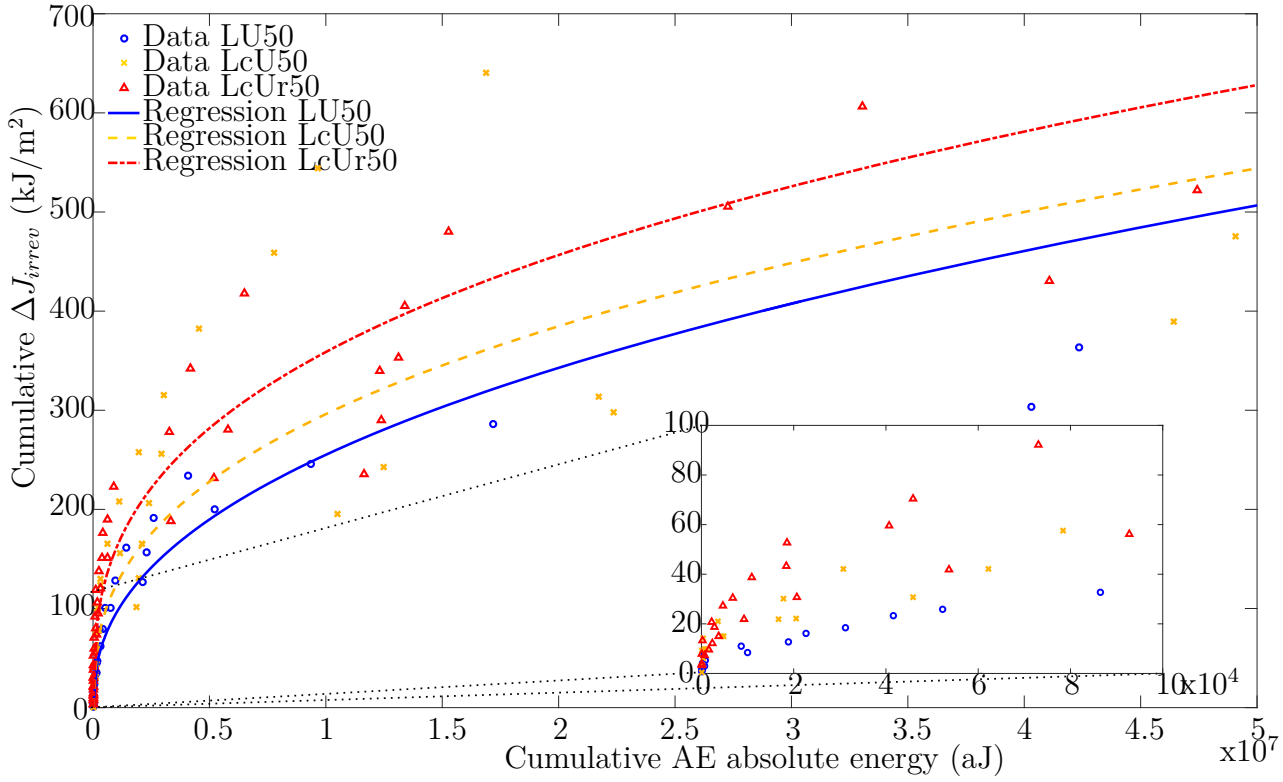

Figure 5.10 Cumulative ΔJ_{irrev} as a function of the cumulative AE absolute energy for AP SEN specimens subjected to various test conditions at 120 °C. Here, the cumulative AE absolute energy is used as a damage propagation indicator instead of crack extension. The ΔJ_{irrev} are quite scattered, especially in the last cycles. However, an emerging trend can be guessed for the early stage of the tests: $\Delta J_{irrev}^{LU} \leq \Delta J_{irrev}^{LcU} \leq \Delta J_{irrev}^{LcUr}$.

creep stages. However, the influence of time-dependent damage on the ultimate failure seems insignificant at this stage due to the lack of differences in the cumulative absolute energies, as shown in Figure 5.12b.

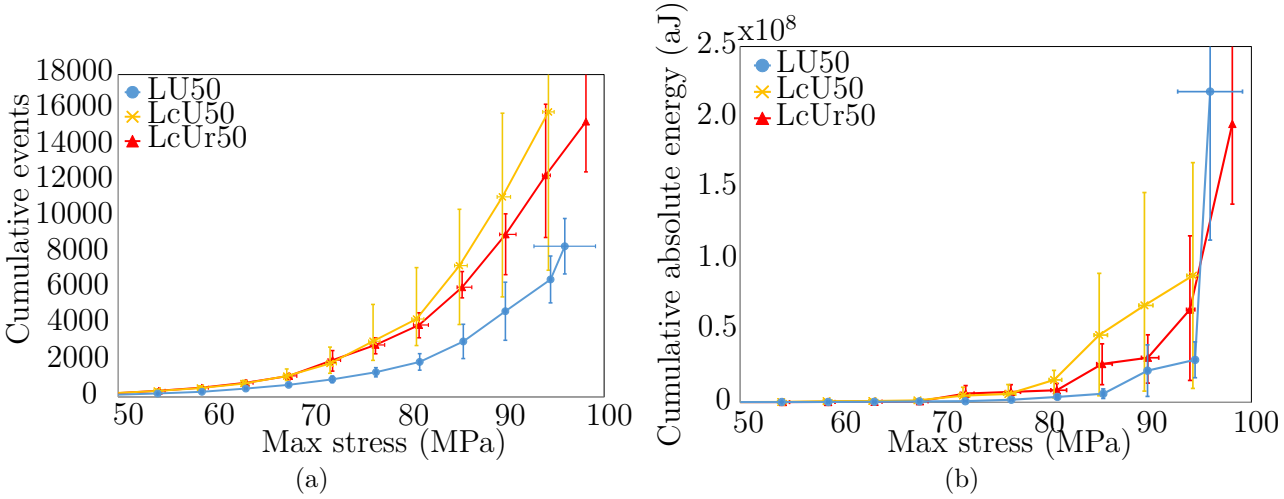

Figure 5.11 (a) Mean cumulative AE events and (b) Mean cumulative AE absolute energy per cycle for AP SEN specimens subjected to various test conditions at 120 °C (the "error" bars represent the min and max values for each cycle). The LU test condition triggered a lower amount of AE events than the LcU and LcUr load configurations, indicating less damage accumulation. However, the evolution of the cumulative AE absolute energy indicates that the criticality of damage is the same for all the test configurations.

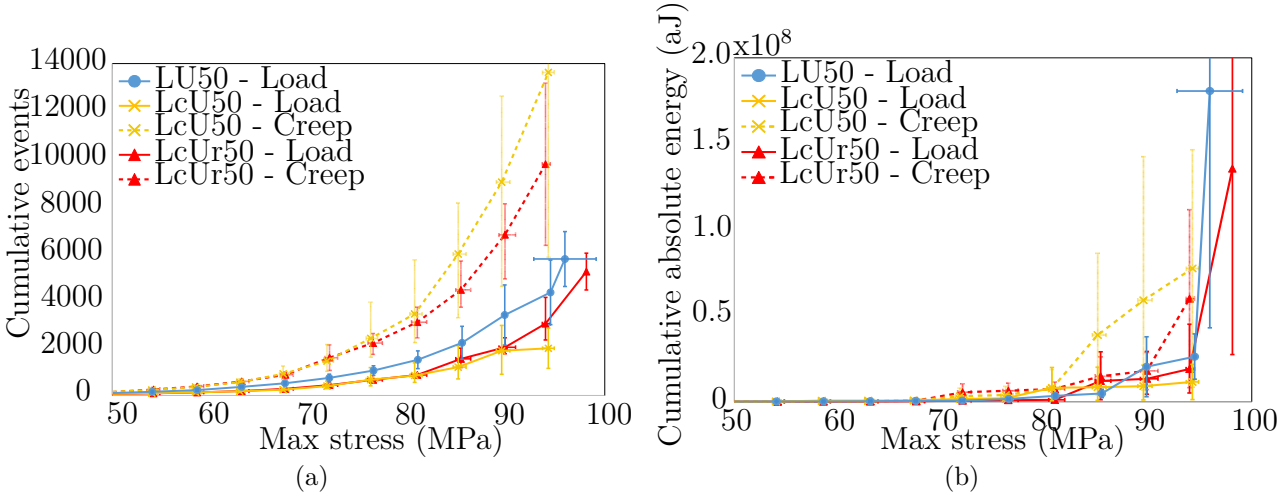

Figure 5.12 (a) Mean cumulative AE events and (b) Mean cumulative AE absolute energy during loading and creep for AP SEN specimens subjected to various test conditions at 120 °C (the "error" bars represent the min and max values for each cycle). More events appear during the creep stages indicating possible time-dependent damage. However, no significant difference can be observed in the evolution of the cumulative AE absolute energies between the loading and creep phases.

5.2 Discussion

5.2.1 QI stacking sequence

The experimental results presented in Figures 5.1 to 5.6 suggest that potential time-dependent phenomena have little influence on QI specimens fracture mechanisms, at the macroscopic scale. Though it appears that the LcUr50 configuration has a higher σ_r^{remote} (Figure 5.2a), this difference can be explained by the shorter crack length. Indeed, the LcUr50 configuration presents a notch ratio significantly different (about -17%) from the other ones. As time-dependent effects are limited in QI specimens, and assuming that QI specimens display linearly elastic and brittle fracture without prior crack propagation, the critical energy release rate G_c should be material-dependent and not dependent on the crack length. Therefore, G_c is a more relevant parameter than the σ_r^{remote} to compare the influence of loading configurations on translaminar failure. This is confirmed in Figure 5.4 as no significant differences in G_c are observed for the different loading configurations. Furthermore, no significant difference was observed in terms of fracture morphology (Figure 5.3) and number of cycles to failure (Table 5.1).

However, AE seems to indicate that the higher the solicitation rate, the slower the evolution of cumulative events as a function of the remote stress is (Figure 5.5). In addition, the tests conducted with creep and recovery stages show that creep stages may induce some time-dependent damage, as suggested from the AE activity (Figure 5.6). However, the influence of creep should be further investigated by means of longer creep steps to exacerbate time-dependent damage.

Those observations suggest that translaminar failure mechanisms are not influenced by time-dependent phenomena and possible subcritical (*i.e.*, that does not significantly influence the macroscopic behaviour) time-dependent damage for QI laminates.

5.2.2 AP stacking sequence

LU tests at 5 and 500 N/s were not conducted for AP specimens because the number of specimens was limited. However, rate effects are expected to be more significant in AP specimens and should be further investigated. After noticing that (i) the loading rate does not influence the fracture behavior for QI specimens and that (ii) AE events were recorded during creep stages for those specimens, the investigations focused on AP specimens subjected to gradual tensile loading with creep stages at $T > T_g$. The purpose of the present work being to specifically understand the influence of time-dependent effects on translaminar fracture, both viscoelastic and viscoplastic behaviors are exacerbated in such testing conditions.

Both ϵ_r and σ_r^{remote} are not significantly influenced by the loading conditions, which seems to indicate that the critical failure mechanisms are similar, as highlighted by the fractographic analysis (see Section 5.1.2.2). Those failure mechanisms are mainly bundle/matrix debonding, fibre bundles breakage and meta-delamination. The critical failure mechanisms do not seem to be significantly influenced by time-dependent behaviors involved during creep stages. This could either mean that the creep steps only affect subcritical damage or that the macro-crack propagation is mainly unstable after its initiation, thus leading to similar fracture surfaces. The first observation is supported by the AE activity analysis that suggests an influence of time-dependent phenomena on the onset of damage accumulation and subcritical damage accumulation. Indeed, damage development globally occurs earlier for the LcU and LcUr tests, when compared to what happens during the LU tests, based on the evolution of the cumulative AE events (Figure 5.11). This observation becomes less obvious close to ultimate failure. This could underline that critical damage accumulation is virtually not influenced by time-dependent phenomena for the studied time scale and that subcritical damage does not influence the ultimate failure of the specimens, as highlighted by the number of cycles to failure in Table 5.2. This analysis also points out significant events, and thus probably damage, involved during creep stages, when compared to the events occurring during loading phases (Figure 5.12).

The analysis of ΔJ_{irrev} as a function of the cumulative AE absolute energy (Figure 5.10) yields curves whose shape is similar to the conventional J-R curves. However, no definitive conclusion about the influence of the time-dependent phenomena on the fracture toughness can be drawn without a reliable AE criteria for the macro-crack initiation detection. If one considers that a given AE energy reflects a similar damage state between the different configurations, the specimens subjected to the LcUr and LcU loading conditions result in slightly higher values of ΔJ_{irrev} in the early stages of the test due to the visco-elasto-plasticity involved during the creep stages. Such an effect is less obvious after the early stages probably due to the accumulation of more critical damage mechanisms resulting in an extensive and complex fracture process zone mixing translaminar and interlaminar failure mechanisms, as observed in Figure 5.9. Furthermore, existing or evolutive critical damage, especially interlaminar cracks, could generate some noise signals during the cycles due to friction, which results in potential scatter in the cumulative AE absolute energy. Thus, AE absolute energy might not be the best macro-crack initiation/propagation in this case. Further investigations are necessary to clarify this point.

For now, the influence of time-dependent behaviours involved by 15-minute creep stages does not seem significant on critical damage propagation at the macroscopic scale. The influence of time-dependent phenomena is rather expected to be observed on both micro- or mesoscopic

damage initiation and early accumulation due to the presence of matrix-rich areas within the laminates. Indeed, these areas are characterized by locally time-dependent behaviours.

5.2.3 Comparison between QI and AP laminates

AP specimens exhibited a highly time-dependent behaviour, when compared to QI specimens (see Figures 5.1 and 5.7). Furthermore, the AP specimens exhibited a strain at failure 10 times higher than that of the QI specimens. However, the stress at failure is about twice as low as in AP specimens, resulting in greater computed ΔJ_{irrev} in AP laminates, when compared to the values of G_c in QI laminates. This difference is primarily due to different failure mechanisms resulting from specific microstructures. On the one hand, AP specimens display a highly visco-elasto-plastic behaviour that could slow down the propagation of the macro-crack through stress redistribution leading to more extensive secondary damage development around the notch, as observed in Figure 5.9. Furthermore, AP specimens are characterized by extensive delamination, fibre bundle/matrix debonding and pull-out, leading to higher computed ΔJ_{irrev}, when compared to the strain energy release rate of QI specimens, for which interfacial failure is limited. On the other hand, QI specimens, whose macroscopic behaviour is fibre-dominated, are characterized by less plasticity, less secondary damage and a smaller Fracture Process Zone (FPZ). This observation is also supported by the AE analysis of the LU50 configuration. Indeed, the failure of AP samples generates slightly more AE events than their QI counterparts, suggesting that more extensive damage develops in AP laminates.

It should be recalled that this fracture mechanics-based analysis is a qualitative comparison. This approach only provides rough estimations of the translaminar fracture toughness of the studied specimens. In addition, QI and AP specimens exhibit different fracture mechanisms, and therefore require specific experimental procedures. QI specimens present elastic-brittle behaviour characterized by unstable brittle failure without prior stable growth, therefore a critical value can be defined unambiguously. However, AP specimens exhibit highly elasto-plastic behaviour characterized by little stable crack propagation and ultimately an unstable propagation. Thus, the fracture toughness results are presented in a form equivalent to a J-R curve for AP specimens, what was not possible for QI specimens due to unstable failure.

5.3 Conclusion

An original approach combining AE activity monotoring, fractographic analyses and fracture mechanics was considered to specifically address the influence of PPS matrix time-dependent

behavior at $T > T_g$ on the translaminar failure of woven-ply PPS-based laminates. To the author's best knowledge, there is no study in the literature that deals with the effects of time-dependent phenomena in the case of translaminar fracture of woven composites. Thus, 5HS C/PPS SEN specimens with two stacking sequences subjected to different loading conditions (different solicitation rates or creep and/or recovery stages) were considered. The purpose was to ponderate the contribution of PPS matrix viscoelastic-viscoplastic behavior to the thermo-mechanical response of C/PPS composites.

From a general standpoint, it seems that damage mechanisms causing ultimate failure are not significantly influenced by time-dependent phenomena for both stacking sequences, though both layups exhibit AE events during the creep stages, which could mean that possible time-dependent damage is only subcritical. Those AE events needs to be further investigated through a coupled approach with other monitoring tools, such as digital image correlation, in-situ microscopic observations or thermography, to provide a better insight into the underlying physical phenomena. In addition, the investigation of those AE events and the possible crack length changes along with time-dependent effects for longer creep time may be necessary to get a better insight of the influence of visco-elasto-plasiticity on the translaminar failure.

The QI specimens do not exhibit any significant time-dependency from the macroscopic standpoint, probably due to their fibre-dominated behaviour and a very localized time-dependent behaviour. The time-dependent phenomena may influence the early stage of damage or crack development rather than the latter stage (*i.e.*, macro-crack propagation up to the specimens ultimate failure) for AP specimens. The fact that damage growth in AP laminates consists in multiple failure mechanisms that are not purely translaminar may be the reason for which no definitive conclusions can be drawn during the last stage of loading.

Ultimately, further investigations are required, and the experimental protocol should be improved to obtain more quantitative and accurate results. A few improvements can be considered to enhance the quantitative capabilities of the experimental protocol, namely

- Develop of a stable crack propagation. This problem can be solved by using other specimen geometries. Tests under displacement-controlled conditions should be used as force-controlled tests generally lead to an early crack growth instability.

- Use complementary monitoring tools along with AE to follow the macro-crack initiation and its propagation to obtain more reliable quantitative results from the fracture mechanics analyses. This could be achieved using an additional monitoring technique, as DIC or IR thermography. Though AE data presents a significant scatter in this study, such technique provides real-time and in-situ qualitative information regarding

damage evolution and the interaction between damage and time-dependent effects at the microscopic scale. In addition, AE activity may be correlated with the macro-crack propagation [112, 113]. To reduce data scattering, additional filters (either feature-based or spatial filters) may be needed to specifically work on events, which originate from the FPZ. Furthermore, the optimization proposed in the previous point should result in a crack growth with less unwanted interlaminar failure mechanisms and may result in less scatter in AE data.

This study highlighted AE events during creep steps. Those AE events might represent time-dependent damage development. The next chapter is the investigation of that AE activity.

CHAPTER 6 Time-dependent damage development during creep in woven-ply C/PPS laminates above the glass transition temperature

This chapter presents the results of the second experimental campaign, whose the main purpose is to monitor time-dependent damage development within AP C/PPS laminates at 120 °C during creep tests. Indeed, the previous chapter highlighted AE events during creep stages. However, it was concluded that if those events were damage-related, then those damage sources should be subcritical. Therefore, a better understanding of time-dependent damage accumulation is needed through the investigation of the conjoint development of damage and other mechanisms, such as viscoelasticity, viscoplasticity and fibre bundle rotation. The experimental protocol was detailed in Section 4.3.2.

6.1 Preliminary results - LcUr tests

Several preliminary tests were necessary before performing CC tests to provide answers to two main questions:

- does temperature cycling has an impact on damage within AP 5HS C/PPS specimens?
- what creep stress levels should be considered?

6.1.1 Temperature cycling

One specimen was subjected to temperature cycling while the load was kept at 0 N to verify if cyclic variations in the 50-120 °C temperature range have a significant influence on damage development.

Edge views are presented in Figure 6.1. Figure 6.1a shows a micrography of the specimen edge before testing, whereas Figure 6.1b shows the same area after temperature cycling. No significant cracking was observed on the specimen edges after the test.

AE signals were detected during the test, as illustrated in Figure 6.2 representing the variation of temperature and the cumulative AE hits as a function of time. A total of 155 hits were recorded, but only one event was monitored. Most hits occurred during the temperature decrease or the first increase. Since only one hit was monitored, the rest of the AE activity should either have an energy level too low to be detected by both sensors or occur outside the investigation area. In addition, the event detected does not seem to be originated from a damage source, as illustrated in Figure 6.3 representing the waveform monitored by the

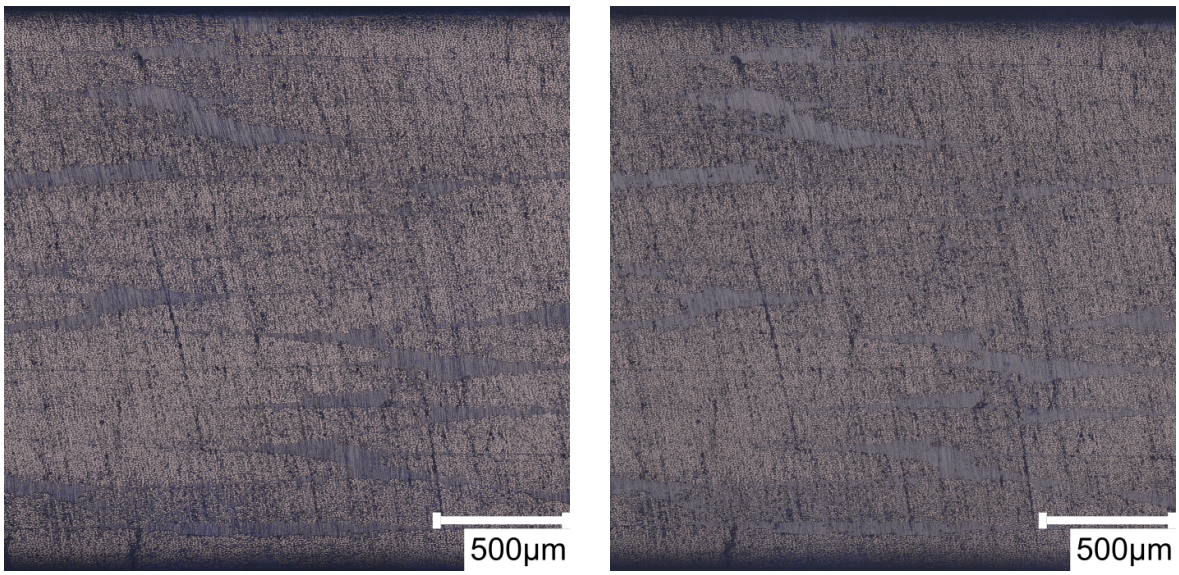

(a) (b)

Figure 6.1 Micrographs of an AP 5HS C/PPS specimen's polished edge (a) before and (b) after temperature cycling between 50-120 °C. No significant temperature-induced cracking can be observed.

nearest sensor. The event seems to come from a noise-based source due to its long duration. In conclusion, these results suggest that temperature cycling in the 50-120 °C range has no significant influence on damage development. However, it may produce a few additional AE signals.

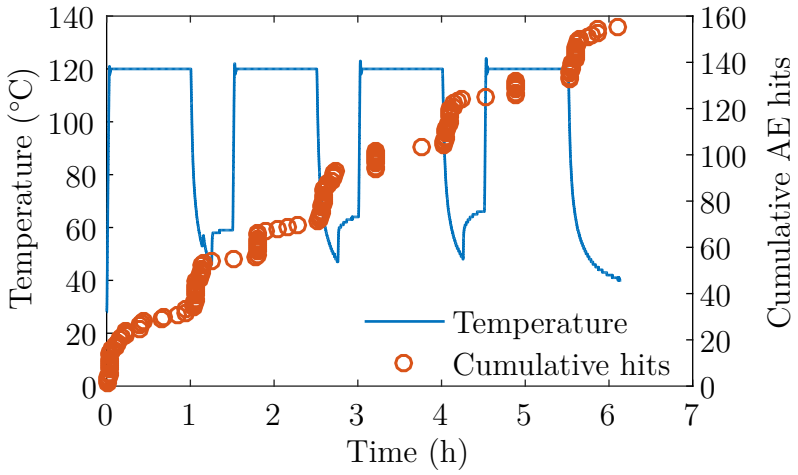

Figure 6.2 Variation of the temperature and the cumulative AE hits as a function of time during the temperature cycling test of an AP 5HS C/PPS. Most of AE hits occur during the first temperature increase or during temperature decreases. AE hits from the first temperature increase may be damage-related (*e.g.*, process-based defects), however AE hits from unloading should be noise-related (*e.g.*, friction-based). Therefore, temperature cycling seems to result in insignificant damage development. However, it may induce additional AE signals.

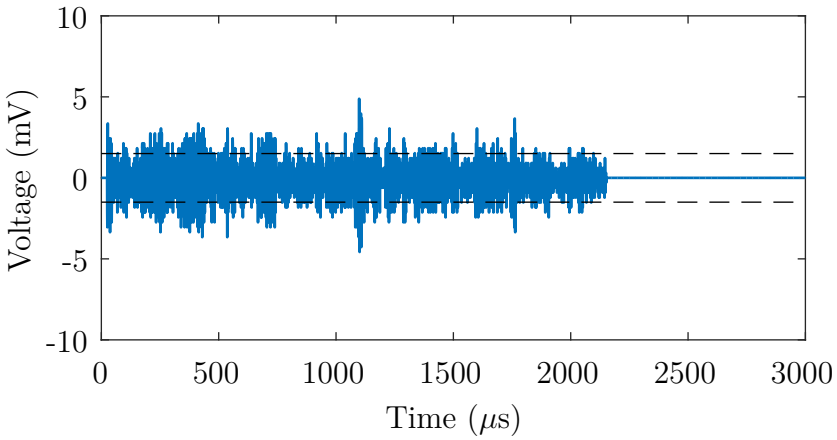

Figure 6.3 Waveform of the only AE event monitored by the nearest sensor during the temperature cycling of an AP 5HS C/PPS. This waveform seems to be noise-related due to its long duration.

6.1.2 Determination of creep stresses

Incremental LcUr (Figure 4.8c) tests were also performed in order to determine the creep stress levels used for the CC tests. The loading rate was set to 50 N/s. The creep and recovery time were set to 15 min. The same monitoring setup as that used for CC tests, though no edge replication was performed. However, the AE filter on the number of counts (*i.e.*, $n > 3$) was applied after acquisition. One of the three tests seemed to present AE monitoring issues (saturation of one sensor) and thus was put aside. Therefore, the following preliminary results are based on only two AP specimens. However, those two tests showed a good reproducibility. The figures in this section only illustrates one of them for clarity purposes.

Figures 6.4a and 6.4b represent the macroscopic damage variable d and the bundle rotations per cycle as a function of the maximum stress reached during the cycles, respectively. The damage d increases between 0 and 100 MPa with a decreasing damage rate between 50 and 100 MPa. A knee-point can be observed at about 100 MPa. It is followed by a quasi-linear damage increase until failure with a higher slope than previously. It should be noted that 15 min recovery steps are not long enough to recover all of the viscoelastic strain, thus the variable d may not describe accurately the damage state. Two thresholds are identified from bundle rotations: the initiation of reversible rotation and the initiation of irreversible rotation. The first one is about 50 MPa and the second is about 80 MPa.

Table 6.1 regroups the stress and strain at different values of cumulative events (*i.e.*, 1, 5, 10, 25 and 50) for both specimens. AE onset determination is not always straightforward. One might not consider the first detected event as the AE onset, since it could be an isolated event from a process-based defect. It appears that AE initiation occurs at about 45 MPa if a 5 events threshold is chosen. However, it seems that damage already occurred before this threshold, as illustrated by the variation of the variable d in Figure 6.4a. AE initiation reflects damage initiation perceptible through a specific AE monitoring setup. Some damage sources may not be detectable for certain experimental conditions (*e.g.*, high noise, high material attenuation, etc.). This AE threshold may be the threshold of a change in damage development (*e.g.*, a new damage mechanism, change in the kinetic of an existing damage mechanism) or a different mechanism, such as friction from bundle rotation whose threshold is about 50 MPa. However, AE events from unloading only starts at 80 MPa, as shown in Table 6.2. Therefore, AE onset threshold should reflect a damage-related mechanism.

Figures 6.5a and 6.5b represent the cumulative AE events and the cumulative AE absolute energy per cycle as a function of the applied stress. Firstly, the number of events during unloading and recovery steps and the associated energy are insignificant when compared to

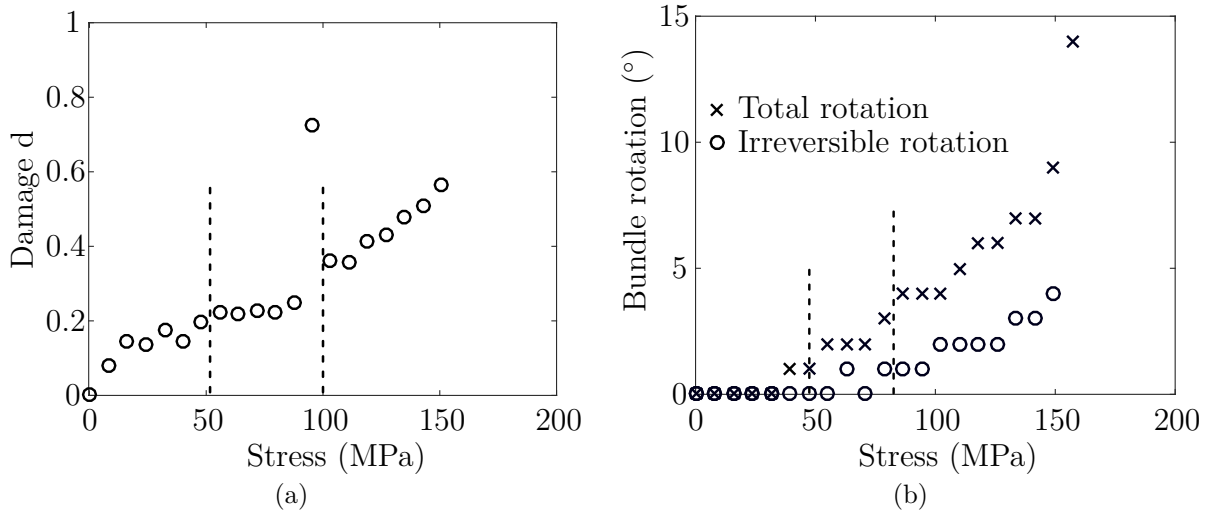

Figure 6.4 (a) Stiffness-based damage variable d and (b) bundle rotation as a function of stress during LcUr tests on AP 5HS C/PPS specimens at 120 °C. Two thresholds can be observed through the variation of the damage variable d: the first one around 50 MPa between an increasing and a stable regions, and the second one at 100 MPa corresponding to a second increase in d. Two other thresholds can be detected via the bundle rotation: the start of reversible rotation at 50 MPa and the onset of irreversible rotation at about 80 MPa.

the total number of events. This suggests that the monitored AE events are not friction-related sources. Secondly, it appears that AE activity during creep steps is larger than that during loading stages. AE activity during creep may reflect time-dependent damage. Lastly, a threshold can be identified between 80-90 MPa from those two graphs. It represents an acceleration in AE activity, which could mean a change in the main damage mechanisms occurring within the specimens. After this threshold, the cumulative AE events increase in an exponential manner and the cumulative absolute energies increase in a quasi-linear fashion until failure. This threshold is assumed to be a precursory indication of the damage threshold around 100 MPa and could be also related to the irreversible rotation threshold around 80 MPa. One possible explanation is that significant inter-bundle cracking (*i.e.*, meta-delamination) occurs around 80 MPa resulting in a high AE activity and irreversible bundle rotation, which also could accelerate the AE activity if friction-related AE events are detected. Thus, inter-bundle cracking propagation or other associated damage mechanisms development could be associated with the damage threshold at about 100 MPa. However, without knowing the exact damage chronology during those tests, further investigations are needed to confirm this hypothesis. Figure 6.6 shows the variation of the Felicity ratio with the previous maximum stress reached per cycle. This ratio was computed after 5 monitored events in Figure 6.6a and 10 monitored events in Figure 6.6b. The threshold around 70-

Table 6.1 Stress and strain at different values of the total cumulative events during LcUr tests on AP 5HS C/PPS specimens at 120 °C. The initiation of AE activity is at 45 MPa considering the threshold at 5 events.

# events	Specimen 1		Specimen 2		Average	
	Stress (MPa)	Strain	Stress (MPa)	Strain	Stress (MPa)	Strain
1	40	0.0118	31	0.0100	35	0.0109
5	48	0.015	40	0.0138	44	0.0144
10	48	0.0154	47	0.0161	48	0.0157
25	48	0.0172	56	0.0204	52	0.0188
50	56	0.0198	55	0.0238	56	0.0218

Table 6.2 Stress reached previously at different values of the cumulative events during unloading of LcUr tests on AP 5HS C/PPS specimens at 120 °C. Unloading stages starts generating significant AE event at 80 MPa.

# events	Stress (MPa)		
	Specimen 1	Specimen 2	Average
1	72	64	68
5	80	80	80
10	80	80	80
25	88	95	92
50	103	103	103

80 MPa (*i.e.*, when FR < 1) is considered as the onset of significant damage propagation (see Section 2.2.6.2) and seems to be in agreement with the observations made earlier about the increase in AE activity.

Table 6.3 summarizes the three regions identified during the LcUr tests on AP specimens. They are based on the observations made from the different monitoring tools. Two main thresholds are detected. One around 40-50 MPa and one about 80-90 MPa. Therefore, three stress creep levels are considered for the CC tests:

- 40 MPa with some subcritical damage and no bundle rotation,
- 60 MPa with the initiation of more critical damage and some reversible bundle rotation,
- 100 MPa with the development of a critical damage state and some irreversible bundle rotation.

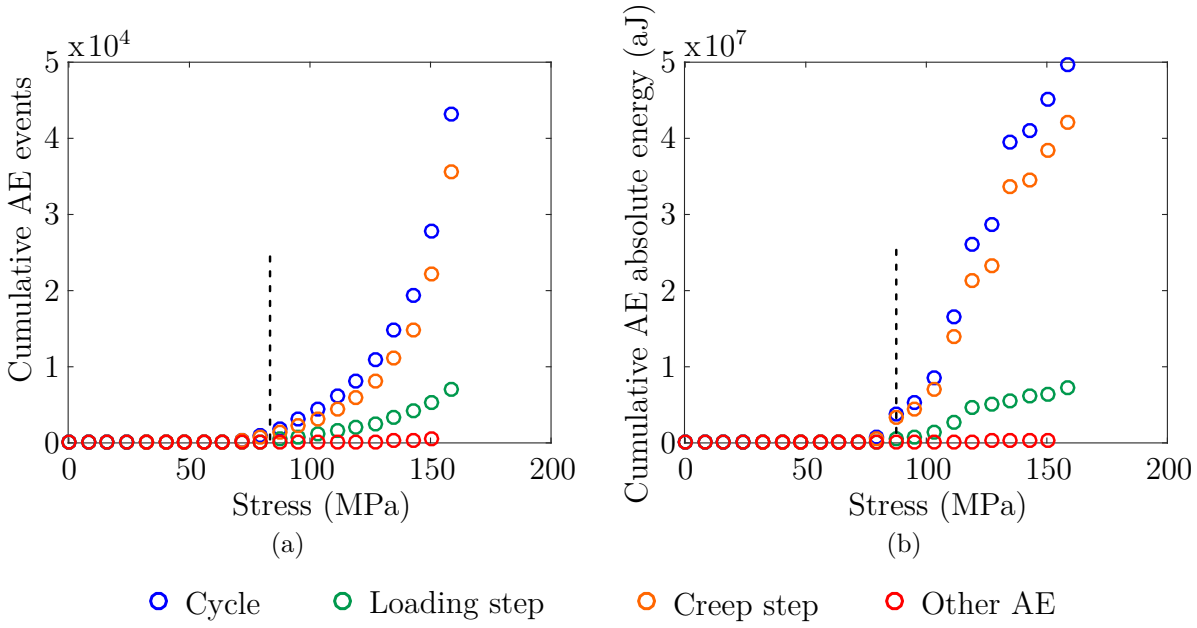

Figure 6.5 (a) Cumulative AE events and (b) cumulative AE absolute energy per cycle as a function of the applied stress during LcUr tests on AP 5HS C/PPS specimens at 120 °C. The different curves represent either the total AE acticity per cycle or a decomposition of the AE activity per cycle into three groups: activity during loading, activity during creep and activity during other stages. The insignificant number of AE events during unloading and recovery stages suggests that monitored AE events are not friction-based sources. Furthermore, the highest AE activity during creep steps when compared to loading stages may reflect time-dependent damage. Finally, a threshold can be observed at about 80-90 MPa corresponding to AE activity acceleration.

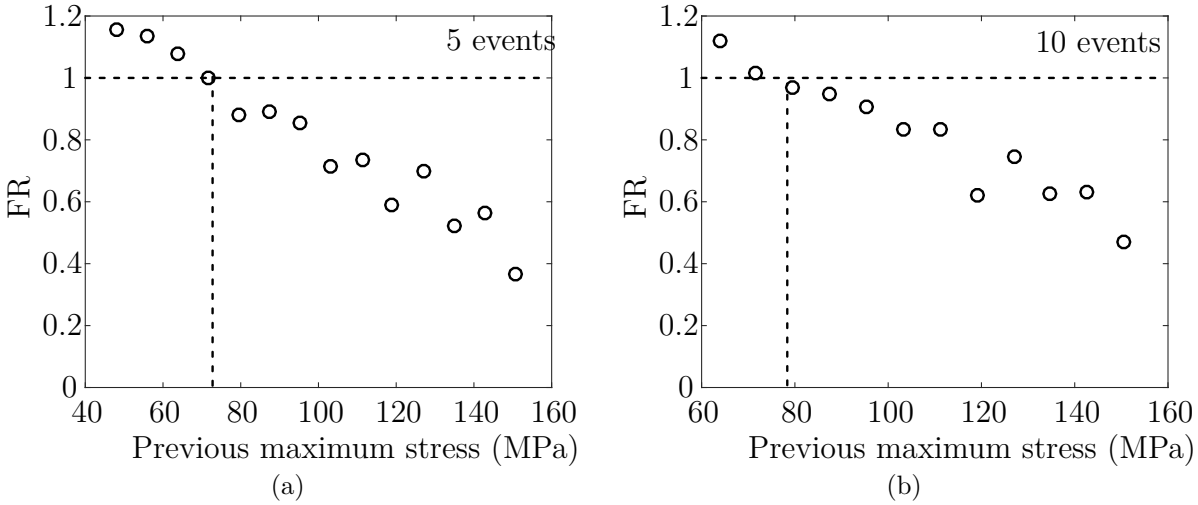

Figure 6.6 Felicity ratio as a function of the previous maximum stress reached per cycle during LcUr tests on AP 5HS C/PPS specimens at 120 °C. FR was computed after (a) 5 monitored events or (b) 10 monitored events. The decreasing FRs point out damage growth within the specimens. Furthermore, the threshold at 70-80 MPa, corresponding to FR < 1, is close to the threshold corresponding to AE activity acceleration which could reflects a critical point in damage development.

Table 6.3 Summary of the three regions identified during LcUr tests on AP 5HS C/PPS at 120 °C.

Stress range (MPa)	Variable d	AE activity	Bundle Rotation	Interpretations
0 - 40/50	Increasing d	No AE activity	No rotation	A few subcritical damage, either microcracking or intra-bundle cracking
40/50 - 80/90	d rate decrease - stable d	Initiation of AE activity	Mainly reversible rotation	Intra-bundle cracking and initiation of some inter-bundle cracking
80/90 to failure	d rate increase	AE activity increase	Reversible and irreversible rotations	Critical development of both cracking mechanisms, especially inter-bundle cracking resulting in delamination and fibre bundle pull-outs

6.2 Main results - Cyclic Creep tests

6.2.1 Viscoelastoplasticity

Figure 6.7 shows the variation of the true axial strain as a function of time during CC tests without edge replications for each stress level. It can be noted that time-dependent behaviours occur for all stress levels.

Figure 6.8 illustrates a few stress-strain cycles of CC tests without edge replications for each stress level. Figures 6.8a, 6.8b and 6.8c show the conditioning cycle, the first creep cycle (*i.e.*, 0.25 h) and the last creep cycle (*i.e.*, 8 h), respectively. The "banana" shape highlighted by Albouy [8] can be observed. The loading phases are characterized by the matrix' viscoelastoplastic behaviour and structural effects related to fibre bundle rotations. A stiffening can be observed, especially for the 100 MPa test. The unloading and recovery phases are characterized by the disorientation of fibre bundles and a viscoelastic behaviour.

The true axial strain is decomposed into two components, ϵ_{ve} and ϵ_{vp} that represent the viscoelastic strain including the instantaneous elastic part and the residual strain after recovery, respectively. This decomposition is expressed as,

$$\epsilon = \epsilon_{ve} + \epsilon_{vp}. \tag{6.1}$$

Figure 6.9 summarizes the increase in true total axial strain (Figure 6.9a), true residual axial strain (Figure 6.9b) and true viscoelastic axial strain (Figure 6.9c) either as a function of the cumulative creep time or the creep time for each stress level. This additive strain decomposition is valid under the infinitesimal strains assumption and considered valid here as a first approximation, though the strains are quite large, *e.g.*, the total strain exceeds 10% for the 100 MPa tests. As mentioned before, it should be noted that the "instantaneous" strain from the loading steps is included in the viscoelastic component. The total true strain increase is quite reproducible with and without edge replications. However, a difference is noticeable for the 40 MPa tests. This small difference can be attributed to the difference in the increase of the true residual strain, as illustrated in Figure 6.9b.

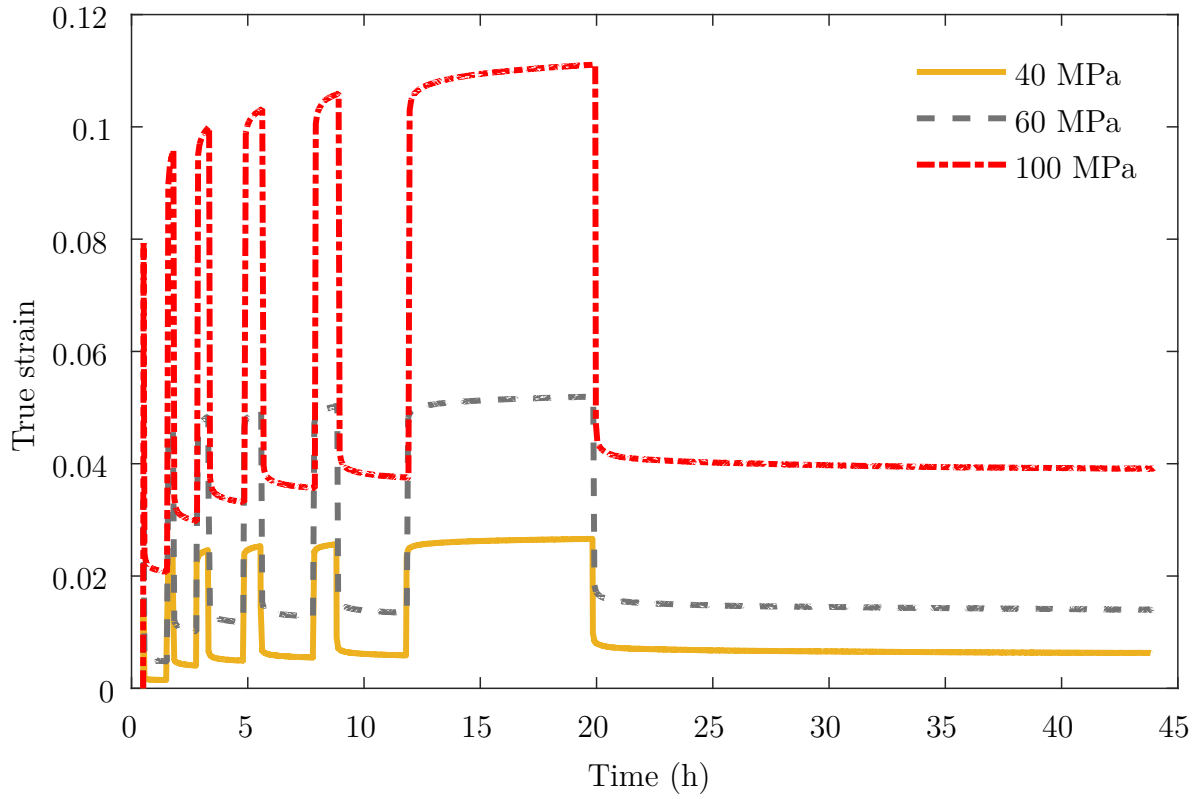

Figure 6.7 True axial strain as a function of time during CC tests on AP 5HS C/PPS at 120 °C without edge replication stages for three stress levels. Time-dependent behaviours can be observed at the three stress levels.

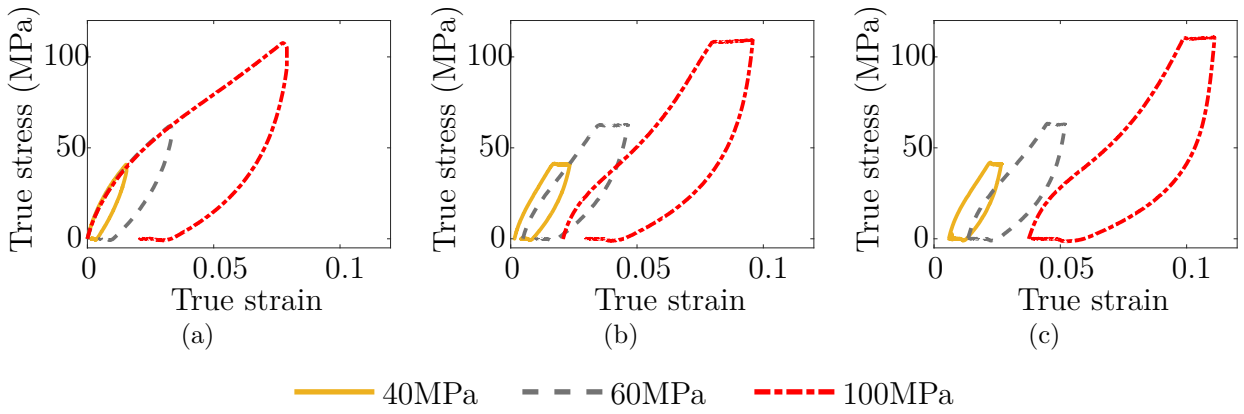

Figure 6.8 Stress-strain cycles during CC tests on AP 5HS C/PPS at 120 °C without edge replication for each stress level: (a) conditioning cycle, (b) 0.25 h creep cycle and (c) 8 h creep cycle. The stress-strain cycles are characterized by a "banana" shaped loop. These stress-strain cycles highlight the matrix' viscoelastoplastic behaviour and a structural effect related to fibre bundle rotations.

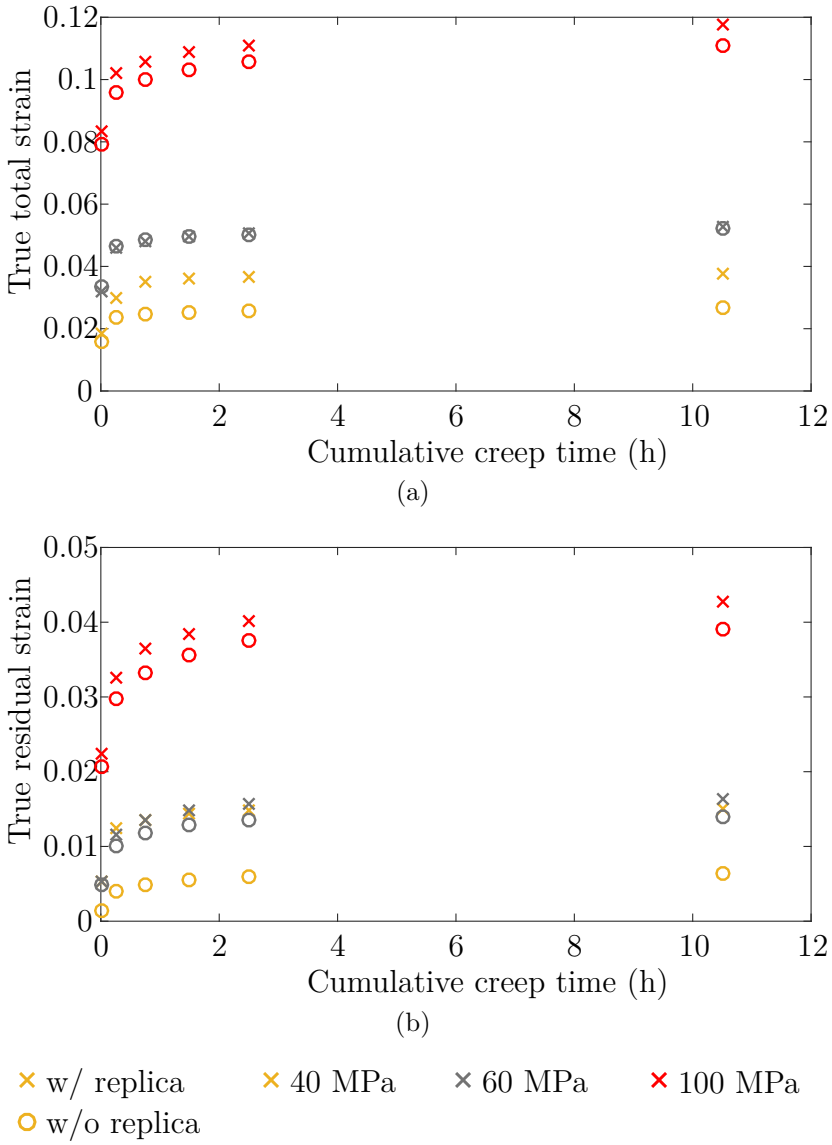

Figure 6.9 (a) Total axial strain and (b) residual axial strain as a function of the cumulative creep time and (c) viscoelastic axial strain as a function of creep time during CC tests on AP 5HS C/PPS at 120 °C for each stress level.

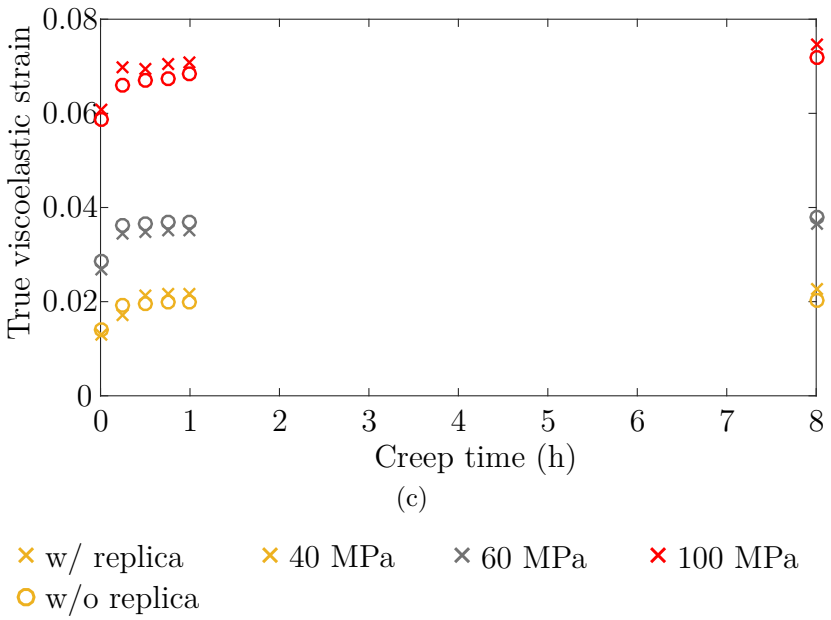

Figure 6.9 ... (continued)

6.2.2 Fibre bundle rotation

Table 6.4 summarizes the average value and the standard deviation of the fibre bundle total rotation, residual rotation and reversible rotation for the last creep cycle for each stress level. The total rotation is determined at the end of the creep stages, whereas the irreversible rotation is measured at the end of the recovery stages. The reversible component is determined from the subtraction of the total value by the irreversible component. Three distinct behaviours can be observed depending on the stress level:

- 40 MPa: little reversible rotation and negligible residual rotation.
- 60 MPa: significant reversible rotation and little residual rotation.
- 100 MPa: large reversible rotation and significant residual rotation.

Figures 6.10, 6.11 and 6.12 summarize the changes in the total, reversible and irreversible fibre bundle rotations per cycle, respectively, for each testing configurations as a function of the cumulative creep time. Time-dependent fibre bundle rotation is mainly observed during the tests at 100 MPa (Figure 6.10c), whereas no significant influence of time-dependent phenomena on the bundle rotation is observed in the 40 and 60 MPa cases. Both time-dependent reversible and irreversible rotations are observed for the 100 MPa tests, as illustrated in Figures 6.11c and 6.12c.

Table 6.4 Summary of the total, irreversible and reversible fibre bundle rotations after the last creep cycle of CC tests on AP 5HS C/PPS at 120 °C for each stress level. The 40 MPa level results in small reversible rotation and insignificant irreversible rotation. The 60 MPa level results in larger reversible rotation and small irreversible rotation. The 100 MPa level results in large reversible rotation and significant irreversible rotation.

	40 MPa		60 MPa		100 MPa	
	Avg	Std	Avg	Std	Avg	Std
Total rotation (°)	1.3	0.9	3.5	1.2	9.5	1.4
Residual rotation (°)	0.5	0.7	1.3	0.8	3.6	0.2
Reversible rotation (°)	0.9	0.3	2.1	0.4	5.9	1.3

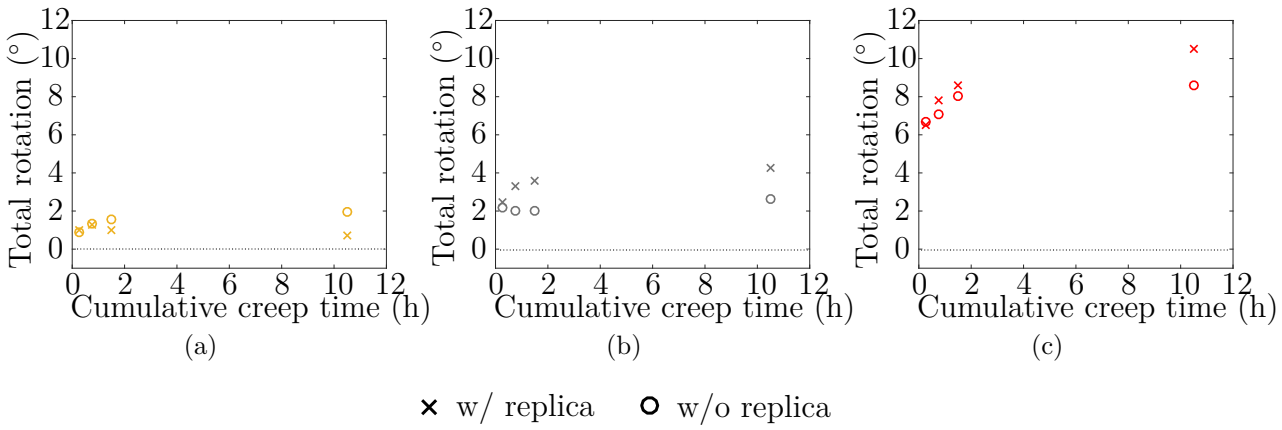

Figure 6.10 Total fibre bundle rotation for AP 5HS C/PPS subjected to CC tests at (a) 40 MPa, (b) 60 MPa and (c) 100 MPa and 120 °C. Only the fibre bundle rotation of the 100 MPa stress level is significantly time-dependent.

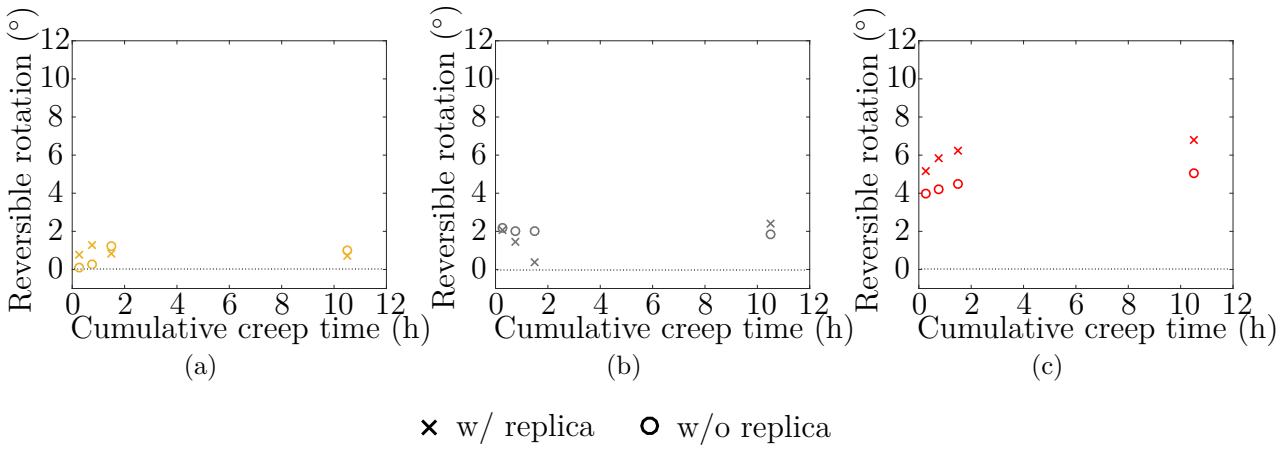

Figure 6.11 Reversible fibre bundle rotation for AP 5HS C/PPS subjected to CC tests at (a) 40 MPa, (b) 60 MPa and (c) 100 MPa and 120 °C. Only the fibre bundle rotation of the 100 MPa stress level is significantly time-dependent.

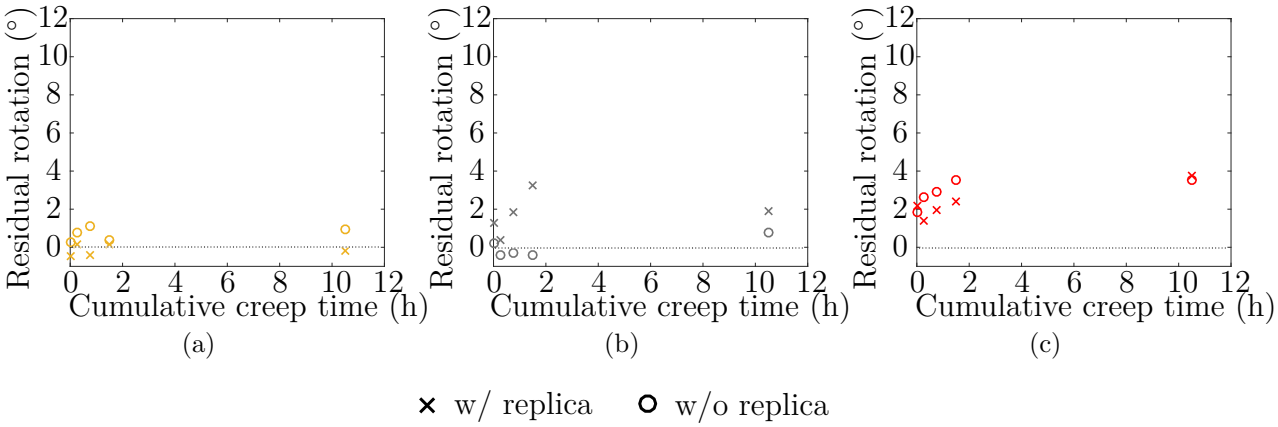

Figure 6.12 Residual fibre bundle rotation for AP 5HS C/PPS subjected to CC tests at (a) 40 MPa, (b) 60 MPa and (c) 100 MPa and 120 °C. Only the fibre bundle rotation of the 100 MPa stress level is significantly time-dependent.

6.2.3 Damage monitoring

6.2.3.1 Tomography

Figures 6.13, 6.14 and 6.15 are ex-situ tomographic observations of specimens subjected to CC loading conditions at 40, 60 and 100 MPa, respectively. It should be noted that the resolution of the tomographic observations is about 16 µm, *i.e.* about twice higher than the fibre diameter. Thus, damage whose size is lower than this resolution is difficult or even impossible to detect from those observations.

First of all, Figures 6.13.a, 6.14.a and 6.15.a show that intra-bundle cracks do not necessarily propagate through the whole specimens' width. It appears that the crack are wider at the edges and on the surfaces of the specimens, when comparing Figure 6.13.a with Figure 6.13.b, Figure 6.14.a with Figure 6.14.b and Figure 6.15.a with Figure 6.15.b. Cracks are less constrained and may open more easily on the free edges and surfaces. Figures 6.13.c, 6.14.c and 6.15.c show the inter-bundle zone in the outer plies for 40, 60 and 100 MPa tests, respectively, while figures 6.13.d, 6.14.d and 6.15.d show the inter-bundle zone in the inner plies for 40, 60 and 100 MPa tests, respectively. Inter-bundle cracking can be observed in all specimens. Those cracks are primarily localized in the crimp regions. It appears that the higher the stress level is, the higher the inter-bundle cracking extent is. Furthermore, Figure 6.15.c shows that the extent of inter-bundle cracking is larger within the surface ply than within the inner ply (Figure 6.15.d) at 100 MPa. This difference is not significant for 40 and 60 MPa tests. Figures 6.13.e, 6.13.f, 6.14.e, 6.14.f, 6.15.e and 6.15.f show the inter-ply area either between the first and second plies or the third and fourth plies in specimens subjected to 40, 60 and 100 MPa CC tests. Those figures suggest that the inter-ply area is less prone to damage accumulation in the form of interfacial cracking than the inter-bundle regions for all stress levels. Porosity-like defects are observed in those regions. However, the conclusion about this defect nature is relatively difficult probably due to the 16 µm resolution.

It is difficult to conclude that damage along the specimens' edges is the same at that observed in the specimens' core. However, it seems that damage along the edges is more significant than damage within the laminates. Therefore, one can assume that the crack density along the edges should be at best representative of damage within the composite and at worst representative of the most critical damage state within the studied specimens.

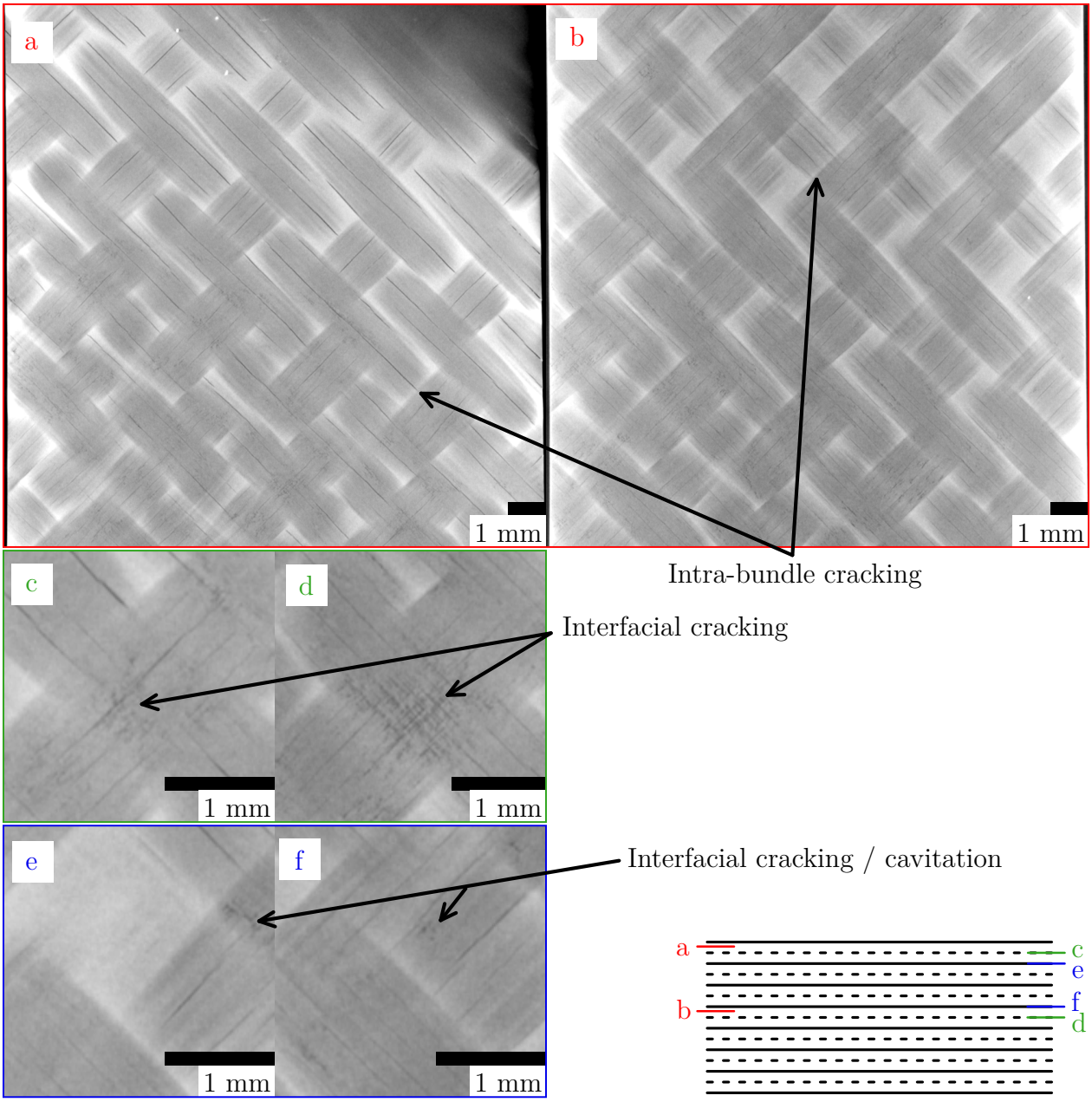

Figure 6.13 Ex-situ tomographic observations of an AP specimen subjected to CC loading at 40 MPa at 120 °C: (a) slice within the intra-bundle region of the first ply, (b) slice within the intra-bundle region of the fourth ply, (c) slice within the inter-bundle region of the first ply, (d) slice within the inter-bundle region of the fourth ply, (e) slice within interlaminar region between the first and second plies and (f) slice within interlaminar region between the third and fourth plies.

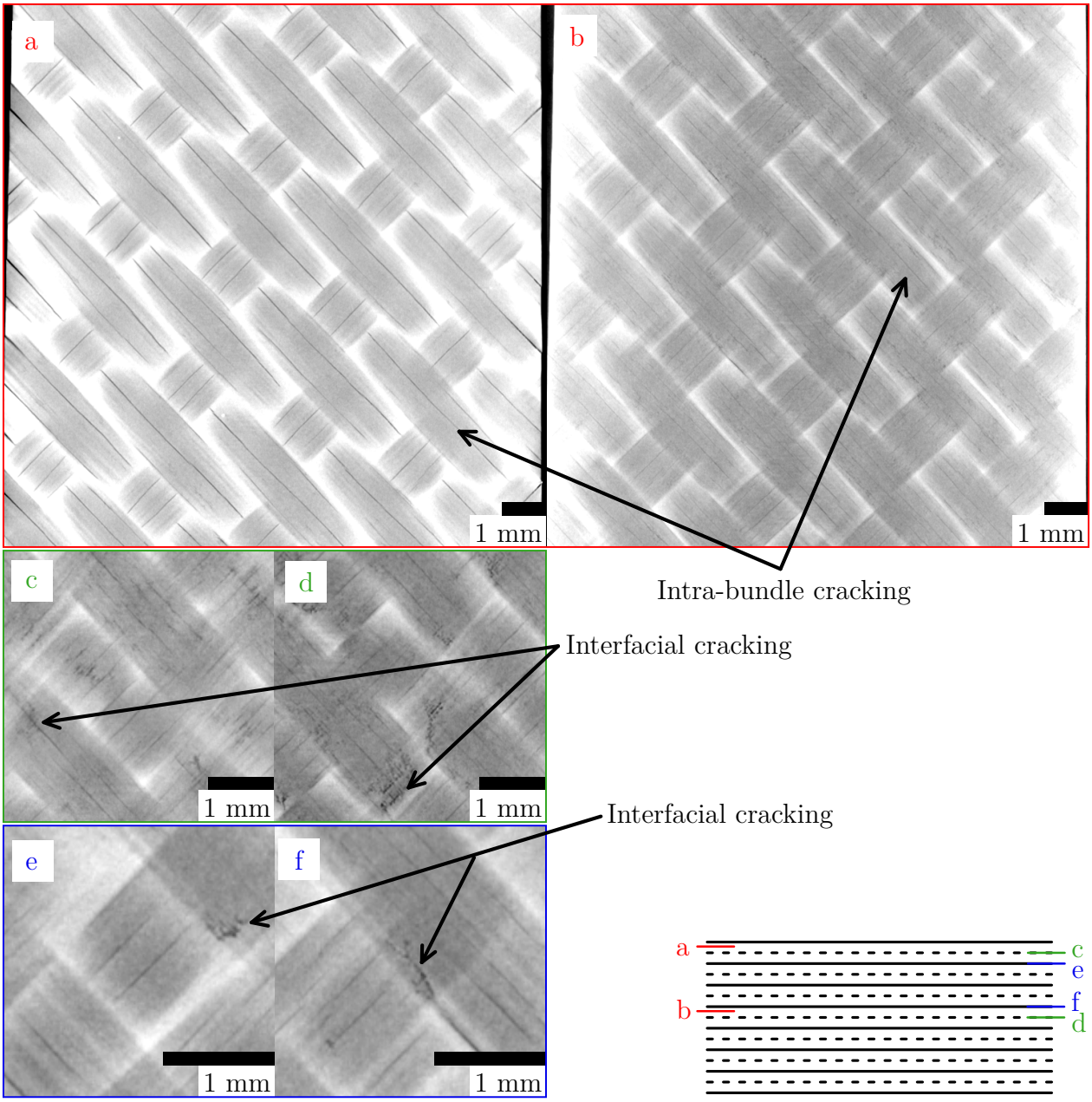

Figure 6.14 Ex-situ tomographic observations of an AP specimen subjected to CC loading at 60 MPa at 120 °C: (a) slice within the intra-bundle region of the first ply, (b) slice within the intra-bundle region of the fourth ply, (c) slice within the inter-bundle region of the first ply, (d) slice within the inter-bundle region of the fourth ply, (e) slice within interlaminar region between the first and second plies and (f) slice within interlaminar region between the third and fourth plies.

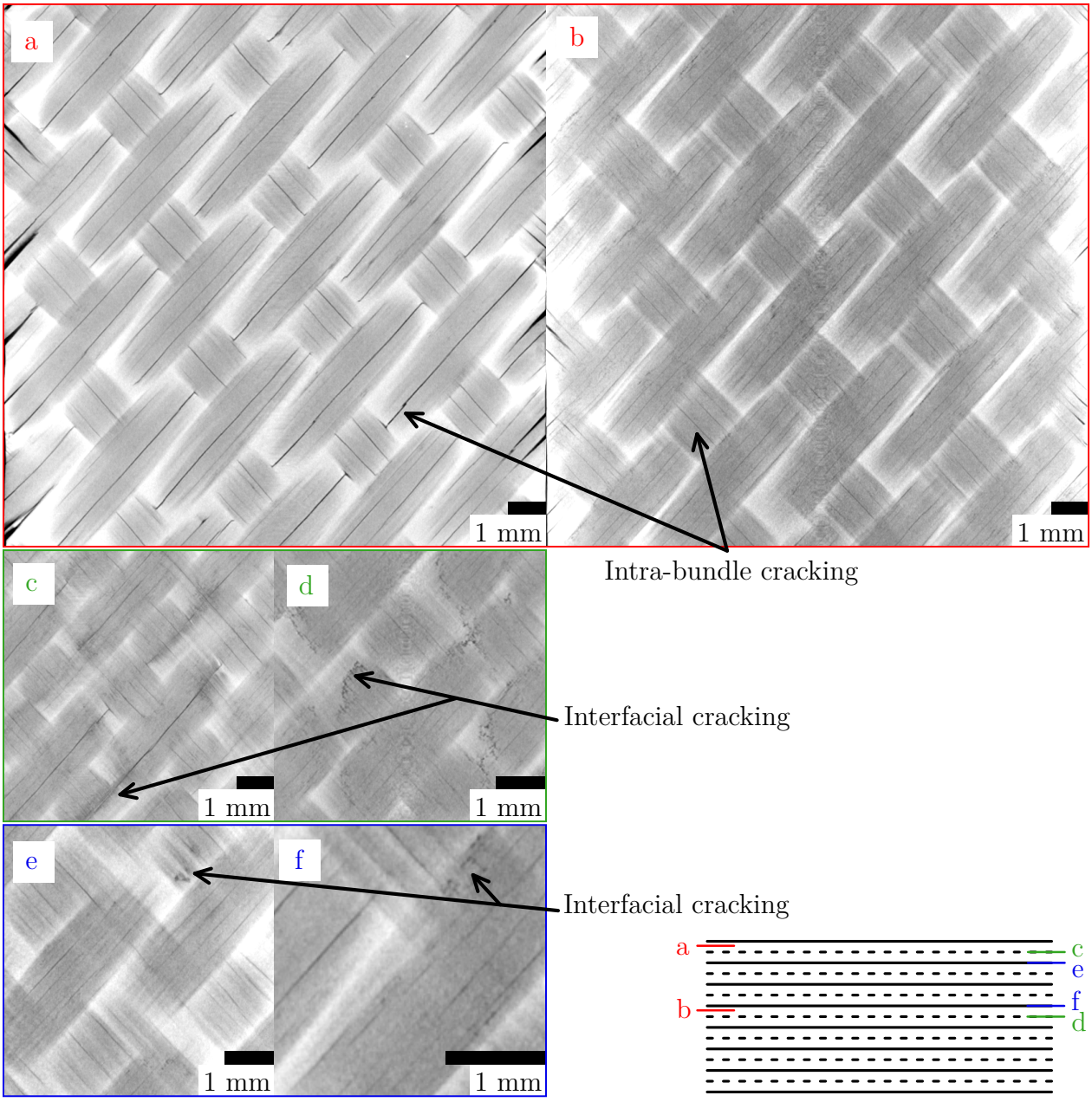

Figure 6.15 Ex-situ tomographic observations of an AP specimen subjected to CC loading at 100 MPa at 120 °C: (a) slice within the intra-bundle region of the first ply, (b) slice within the intra-bundle region of the fourth ply, (c) slice within the inter-bundle region of the first ply, (d) slice within the inter-bundle region of the fourth ply, (e) slice within interlaminar region between the first and second plies and (f) slice within interlaminar region between the third and fourth plies.

6.2.3.2 Edge crack density

Representative micrographs of the specimens' edge after test for each stress level are shown in Figure 6.16. Several trends can be deduced from those micrographs:

- the higher the stress level, the more interfacial cracks there are,
- the higher the stress level, the wider the cracks,
- the higher the stress level, the more intrabundle cracks there are, at least when comparing the 40/60 MPa tests and the 100 MPa test.

The increase in crack width with stress level has two potential causes: either the propagation of cracks towards the laminates' core or the crack blunting due to higher plastic strains at higher stresses, as observed from the plot of the residual strain in Figure 6.9b.

Figure 6.17 shows the crack density as a function of cumulative creep time for each stress level. The crack densities were determined by means of two different methods: crack counting (Figure 6.17a) and cracked surface evaluation (Figure 6.17b). On the one hand, the crack counting method was quite challenging, especially for the replications from the 100 MPa test due to the relatively high amount of cracks, their size distribution and a few bifurcations. Thus, this method was applied only on 3 out of 5 replications. The crack counting protocol produced significant uncertainties in the estimated crack densities, as observed in Figure 6.17a. This figure suggests that there is no time-dependent damage propagation for any stress level, or at least no time-dependent cracking accumulation. In addition, the 40 and 60 MPa tests are characterized by a similar damage state in terms of crack counts with $\sim$30-40 cracks/mm, whereas the 100 MPa specimen displays about 70-90 cracks/mm. On the other hand, Figure 6.17b highlights an increase in the cracked surface density along with an increase in the creep stress level. Above all, it appears that the cracked surface density remains constant with cumulative creep time for the 40 and 60 MPa tests, whereas this density increases with cumulative creep time for the 100 MPa test.

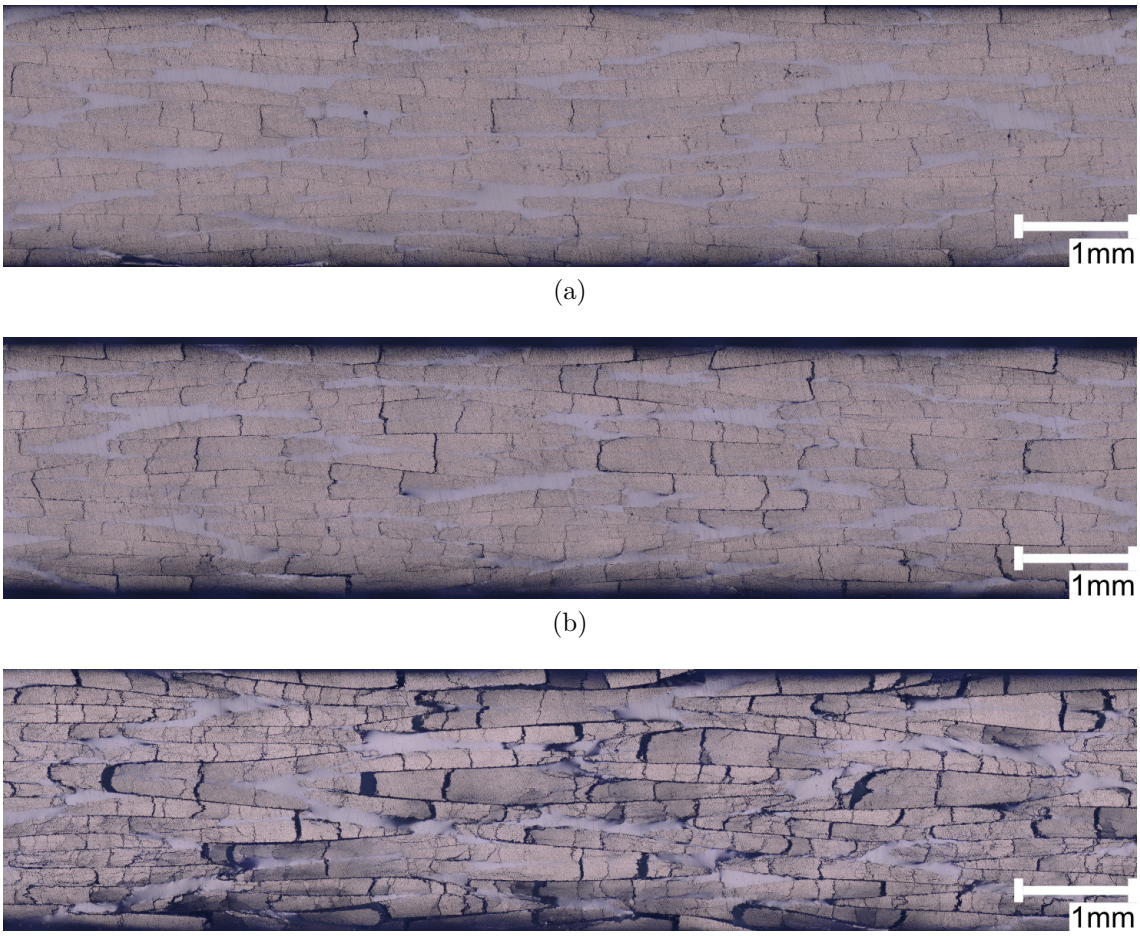

(a)

(b)

(c)

Figure 6.16 Micrographs of the AP 5HS C/PPS specimens edge after CC tests at 120 °C for each stress level: (a) 40, (b) 60 and (c) 100 MPa. The higher the stress level, the wider the cracks. Furthermore, it seems that there are more inter- and intra-bundle cracking for higher stress levels. The crack width increase with stress level is either due to the propagation of cracks towards the laminates' core or due to the crack blunting from higher plastic strains at higher stresses.

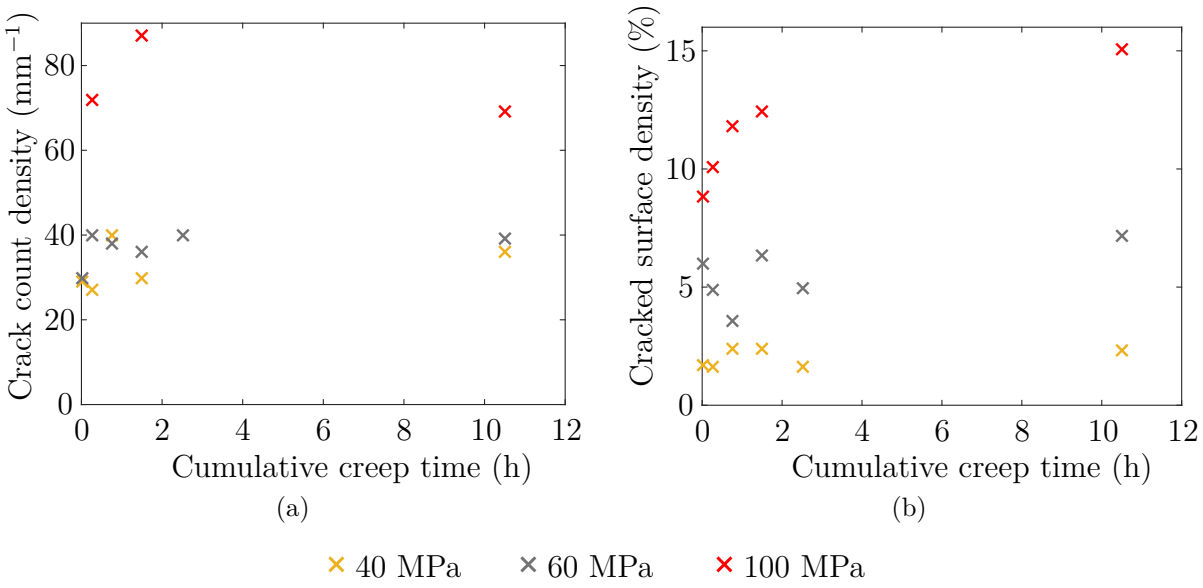

Figure 6.17 Crack density as a function of cumulative creep time during CC tests on AP 5HS C/PPS laminates at 120 °C for each stress level. Crack density was represented by two different variables: (a) crack count density and (b) cracked surface density. The crack count density method produces significant uncertainties and seems to suggest that there is no time-dependent crack accumulation. However, the cracked surface density method shows that only the 100 MPa stress level induces time-dependent damage development.

6.2.3.3 Macroscopic damage variable

Figure 6.18 shows the variation of the damage variable d, as defined in Section 4.3.2, as a function of the cumulative creep time for each stress level. Two trends emerge from this graph. The first one is the instantaneous increase followed by a time-dependent increase in the variable d for the specimens subjected to 100 MPa. The second trend applies to the specimens loaded at 40 and 60 MPa. There is an instantaneous increase in the damage variable but this is followed by a time-dependent decrease in d that reaches negative values. This last trend is discussed in Section 6.3.2.1.

6.2.3.4 Acoustic emission

Figures 6.19, 6.20 and 6.21 show the cumulative AE activity (*i.e.*, cumulative events and cumulative absolute energy) within a 15 mm centered region for 40, 60 and 100 MPa tests, respectively, as a function of the cumulative creep time. The different curves represent either the total activity per cycle or the activities of a decomposition of the AE data into three classes. The three classes represent the AE data detected during either the loading steps, the creep steps or the other steps (*i.e.*, unloading, recovery and possible replication steps). Figures 6.19a and 6.19b, illustrating the cumulative AE events and the cumulative AE absolute energy for 40 MPa tests, show a similar trend for both tests. The total activity shows a time-dependency of the cumulative events and cumulative absolute energy. The increase in AE activity is more significant during the first cycles and tends to slow down for higher cumulative creep times. This trend is similar to the one observed in axial strain with respect to creep time. Figures 6.19a and 6.19b also show that the cumulative events and absolute energy from the loading steps tend to stabilize after 0.75 h of cumulative creep time. However, the cumulative events and absolute energy kept increasing for AE during creep steps. Furthermore, the cumulative events and absolute energy of events from creep steps are greater or equal to those from the loading steps through the whole test. The AE activity associated with the other steps of the tests appears to be insignificant compared to the AE activity during the loading and creep steps. The same analysis about the time-dependency of the cumulative AE events and cumulative AE absolute energy from the total activity is valid in the 60 and 100 MPa test configurations (Figures 6.20a, 6.20b, 6.21a and 6.21b). Besides, the stabilization time of the cumulative events from loading steps is also observed at about 0.75 h for 60 MPa tests, but this stabilization is observed later in the 100 MPa configuration, at about 1.5 h. The stabilization of the cumulative absolute energy from the loading steps is observed at 0.75 h in one of the two tests at 60 MPa, whereas the other one exhibits a jump around 2.5 h. The stabilization in the 100 MPa test configuration

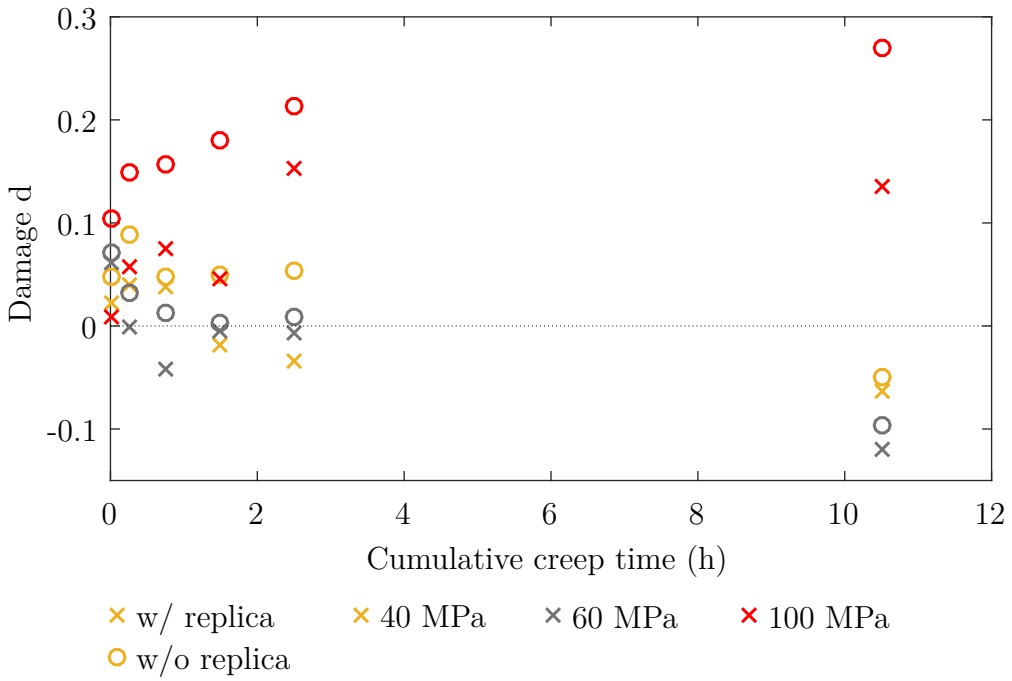

Figure 6.18 Damage variable as a function of the cumulative creep time CC tests on AP 5HS C/PPS laminates at 120 °C for each stress level. The 100 MPa stress level is characterized by a time-dependent increase in d. However, the 40 and 60 MPa stress levels are characterized by an early increase in d followed by a time-dependent decrease leading to negative values.

occurs at about 0.75-1.5 h. The cumulative event and absolute energy from creep steps kept increasing through the whole tests in both 60 and 100 MPa configurations, as observed in the 40 MPa tests. It should be noted that the cumulative events from creep steps at 60 MPa is lower than the events occurring during the loading steps until 2.5 h of cumulative creep time and then becomes higher. The same analysis is also valid for the cumulative absolute energy. However the threshold is around 1.5 h. Figures 6.21a and 6.21b show that the cumulative events from creep steps at 100 MPa are greater or equal to that resulting from the loading steps after 0.75 h of cumulative creep time, whereas the cumulative absolute energy is inferior or equal through the whole test. Both 60 and 100 MPa configurations are also characterized by an insignificant amount of AE events during the others steps of the tests, when compared to the total number of events. This analysis is also valid for the cumulative absolute energy resulting from those steps, except for one of the two tests at 100 MPa with energy jumps around 0.5 h and 2.5 h.

Figures 6.22 and 6.23 show the normalized cumulative AE events and the normalized cumulative AE absolute energy, respectively, as a function of the cumulative creep time considering the total activity or its decomposition into load/creep/other steps for 40, 60 and 100 MPa

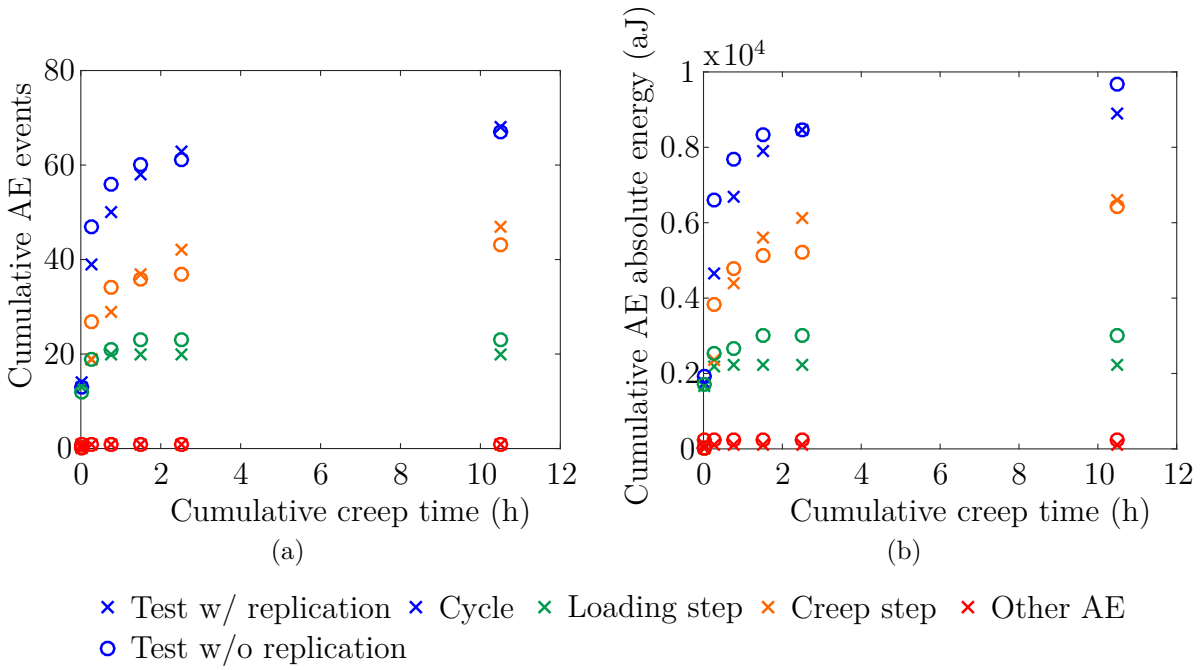

Figure 6.19 AE activity within a 15 mm centered region during 40 MPa CC tests on AP 5HS C/PPS at 120 °C: (a) cumulative events and (b) cumulative absolute energy. The AE activity increase during creep steps may reflect time-dependent damage. The AE activity during unloading and recovery stages is insignificant. Creep steps induce more AE activity than loading phases in terms of quantity and energy.

tests. Figure 6.22a, obtained from the total activity, shows that the increase in AE events is faster for the 40 MPa tests, when compared to the 60 MPa configuration, which is in turn slightly faster than the 100 MPa loading condition. Figure 6.22b confirms the observations stated previously about the stabilization of the cumulative events from loading steps. The 40, 60 and 100 MPa configurations last 0.25-1 h, 1 h and 1-2 h, respectively, to reach 90% of the total number of events detected during loading steps. The normalized cumulative AE events from creep steps increase similarly for the 60 and 100 MPa configurations (Figure 6.22c), whereas the AE events from the 40 MPa tests increase at a faster rate. Figures 6.23a, 6.23b and 6.23c illustrate the same trend regarding the increase in the normalized cumulative AE absolute energy between the 40, 60 and 100 MPa configurations for the total, load and creep data sets, respectively. The time-dependency of the cumulative absolute energy observed for the total data set, as illustrated in Figure 6.23a, is primarily associated with the increase in the cumulative absolute energy during creep steps. All tests reached 90% of the total absolute energy detected during loading steps before 0.75 h of cumulative creep time, except one test at about 2.5 h. This jump in AE absolute energy could result from either damage development or friction.

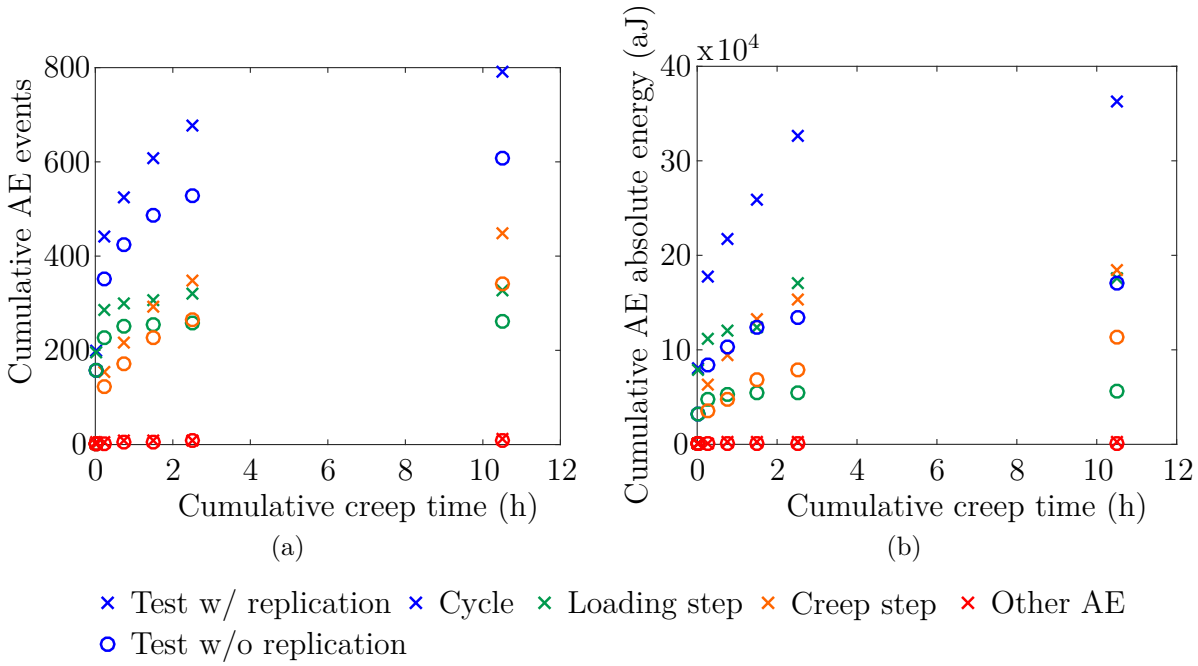

Figure 6.20 AE activity per cycle within a 15 mm centered region during 60 MPa CC tests on AP 5HS C/PPS at 120 °C: (a) cumulative events and (b) cumulative absolute energy. The AE activity increase during creep steps may reflect time-dependent damage. The AE activity during unloading and recovery stages is insignificant. Creep steps induce less AE activity than loading phases in terms of quantity and energy.

Overall, it appears that the time-dependency of the total AE activity comes from the creep steps, while the AE activity from loading steps stabilizes relatively quickly and the AE activity from other steps is not significant. This observation seems to be valid for all tested stress levels. Furthermore, it should be noted that there is an order of magnitude difference in the cumulative AE events and absolute energy between the different stress levels. This last observation suggests that more damage occurs for higher creep stresses, assuming that the monitored AE events are mainly damage-related.

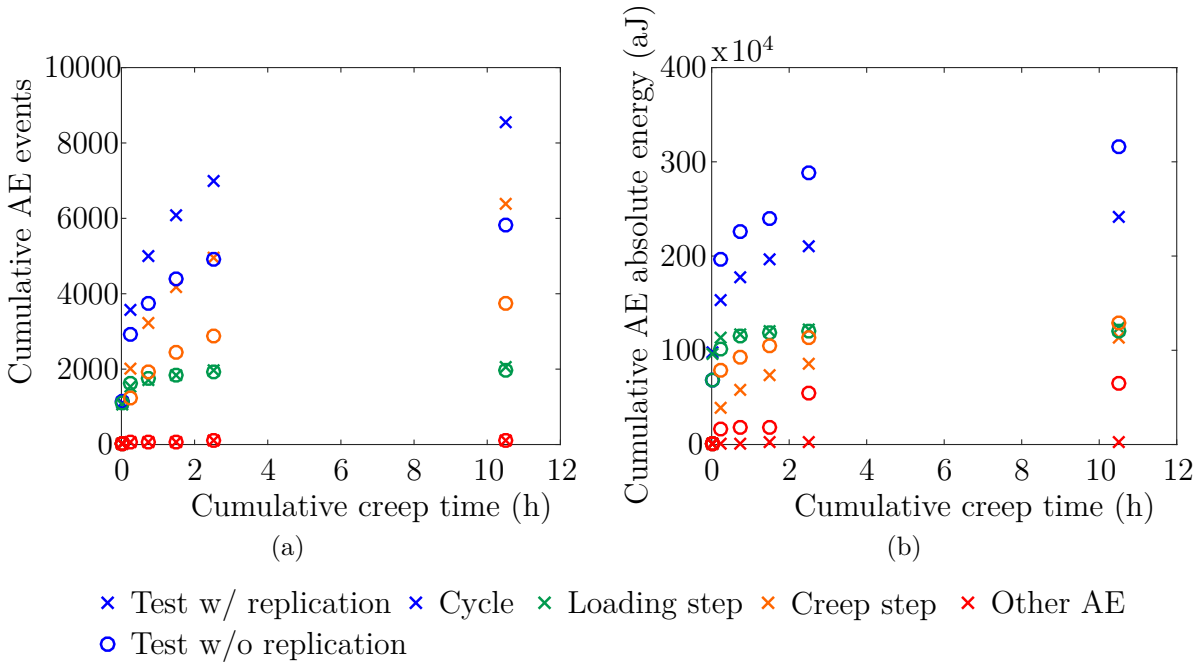

Figure 6.21 AE activity per cycle within a 15 mm centered region during 100 MPa CC tests on AP 5HS C/PPS at 120 °C: (a) cumulative events and (b) cumulative absolute energy. The AE activity increase during creep steps may reflect time-dependent damage. The AE activity during unloading and recovery stages is mostly insignificant. Creep steps induce more AE events than loading phases but less energy.

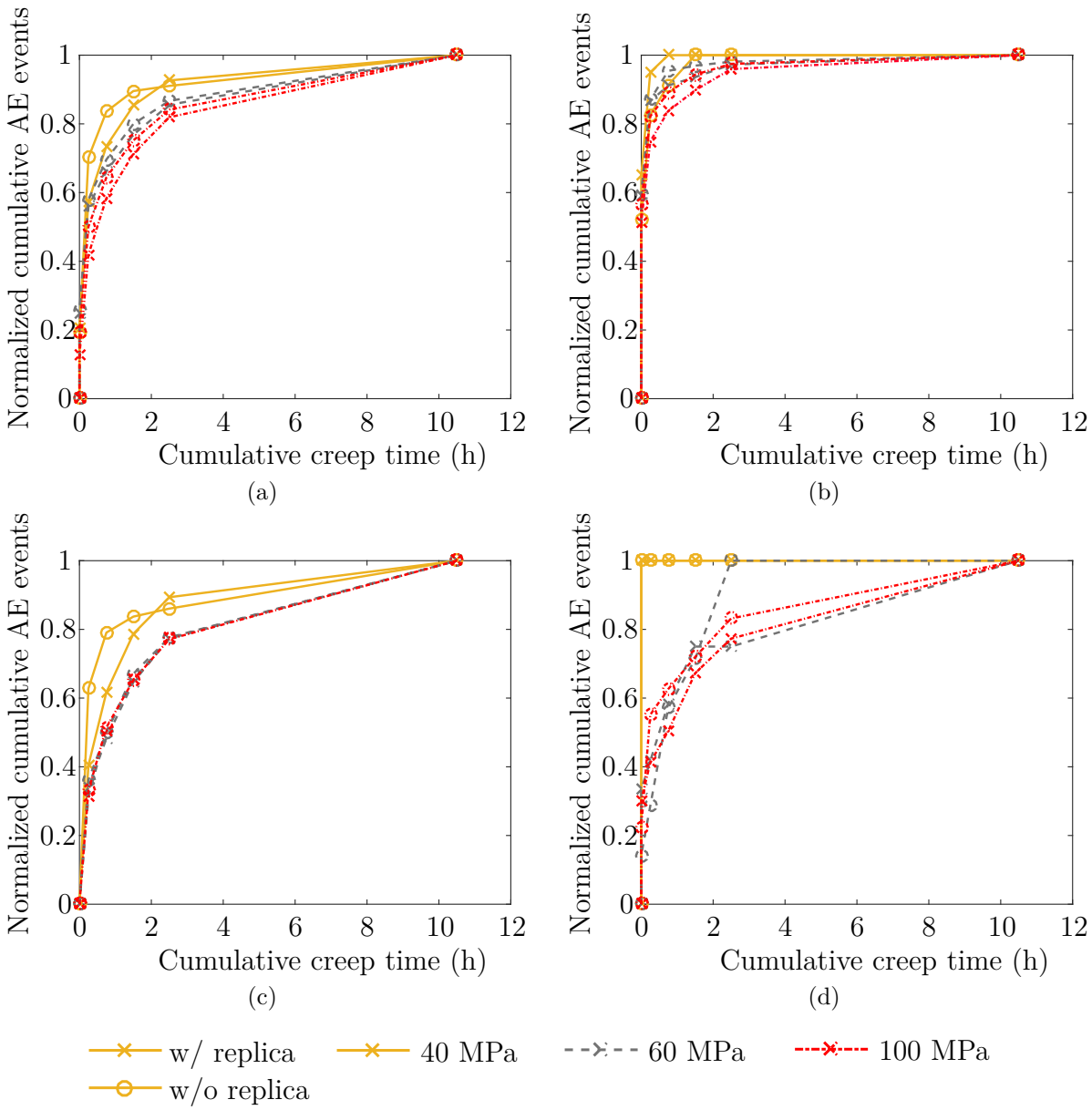

Figure 6.22 Normalized cumulative AE events per cycle within a 15 mm centered region for 40, 60 and 100 MPa tests on AP 5HS C/PPS at 120 °C: (a) total activity, (b) activity during load, (c) creep and (d) other stages. Most of AE events from loading phases occurs during the first cycles. The 60 and 100 MPa stress levels result in a more progressive time-dependent increase in cumulative AE events.

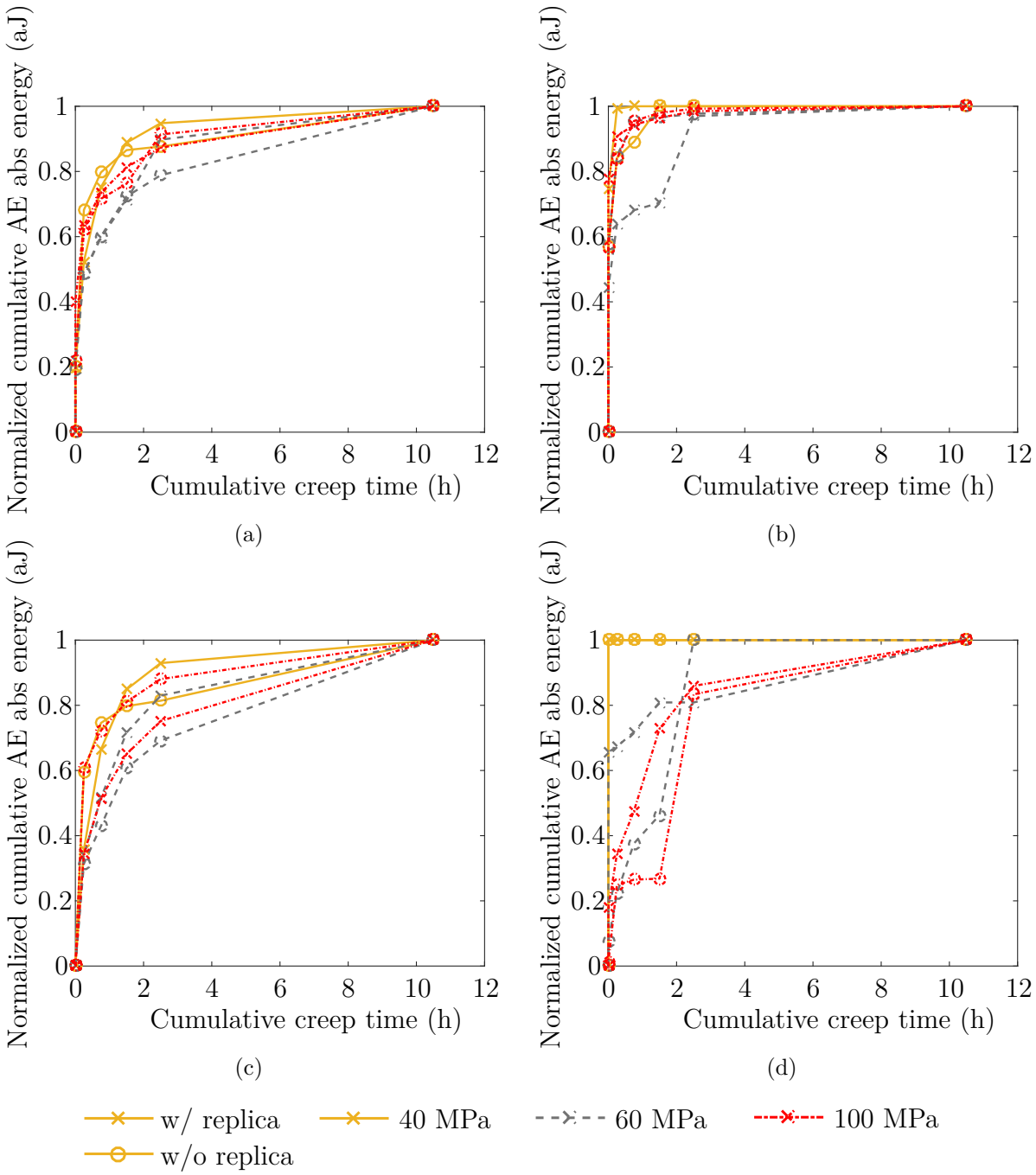

Figure 6.23 Normalized cumulative AE absolute energy per cycle within a 15 mm centered region for 40, 60 and 100 MPa tests on AP 5HS C/PPS at 120 °C: (a) total activity, (b) activity during load, (c) creep and (d) other stages. Most of AE energy from loading phases occurs during the first cycles. The normalized cumulative AE absolute energy from creep steps does not seem to be stress-dependent.

6.3 Discussion

6.3.1 Damage characterization

The first question to answer is: "Is there any damage development during the tests". It can be easily concluded that there is damage development for all stress levels investigated (*i.e.*, 40, 60 and 100 MPa) in the studied laminates at 120 °C from the edge observations (Figure 6.16) and the tomographic observations (Figures 6.13,6.14 and 6.15). Two primary damage mechanisms are detected during those tests: intra-bundle and inter-bundle (*i.e.*, metadelamination) cracking.

Intra-bundle cracking most likely originates from the coalescence of matrix-fibre debonding within bundles. Most of those cracks are oriented through the bundle's thickness, but there are a few oblique cracks. Intra-bundle cracks generally extend through the whole bundle thickness. However, cracks spanning two bundles can be observed in Figure 6.16. This observation has already been reported in the literature in the case of on-axis [31] and off-axis loadings [66]. The distribution of intra-bundle cracking is relatively even between plies. However, these cracks seem wider within the surface plies and along the specimens edges.

Inter-bundle cracking mainly occurred under the form of horizontal cracking between bundles of the same ply. Those cracks most likely originate from intra-bundle crack tips reaching the bundle boundary. The micrographs of the specimens edge suggest that the localization of inter-bundle cracks is relatively even distributed through the laminates thickness. However, the tomographic observations indicate that those cracks are wider within the surface plies than within the inner plies. This is probably due to the fact that the surface plies are less constrained in the out-of-plane direction by neighboring plies. Furthermore, the tomographic observations reveal that inter-bundle cracks preferentially occur in the crimp regions, *i.e.* where the weft bundles undulate over the warp bundles.

The influence of stress level on damage state can be explained by several statements:

- the difference in intra-bundle crack count density does not seem significant between 40 and 60 MPa when considering uncertainties. However, the 100 MPa test results in an intra-bundle crack count density about twice higher than the one obtained from 40 and 60 MPa tests.

- the cracked surface density for 60 MPa tests is slightly higher than the density from specimens tested at 40 MPa. The 100 MPa test resulted in cracked surface density a lot higher (>10%).

- the higher the stress is, the wider the cracks are and the more inter-bundle cracks there are. A more extensive metadelamination can be associated with a larger bundle rotation for higher stress levels, as shown in Figure 6.10.

6.3.2 Time-dependent damage investigations

Once damage development within the laminates is confirmed in the studied laminate, the next step is to know how and when damage mechanisms develop in the different plies.

6.3.2.1 Damage variable: limitations

At first, it should be stated that a stiffness-based damage variable is quite challenging to apply to highly ductile materials whose linear elastic domain is limited. However, a stiffness-based damage variable seemed more appropriate than a strain-based one for a material having a highly visco-elasto-plastic behaviour. The approach proposed by Bassery [20] was used in order to evaluate the elastic modulus of angle-ply specimens.

Secondly, one can notice that the damage variable d decreases after either the conditioning cycle or the first creep cycle in specimens subjected to 40 and 60 MPa. d even reaches negative values at the end of the above-mentioned tests, as stated in section 6.2.3.3. Thus, other competitive phenomena contribute to the increase in the axial stiffness and compensate stiffness loss resulting from damage development. Among these phenomena, one can think of a structural effect (*e.g.*, bundle rotation), a time-dependent behaviour related effect (*e.g.*, unrecovered viscoelastic strain) or a physico-chemical effect (*e.g.*, thermal aging).

The effect of bundle rotation on the specimen axial stiffness was estimated using the following equation [10]

$$\frac{1}{E_x} = \frac{\cos^4\theta}{E_1} + \frac{\sin^4\theta}{E_2} + \left(\frac{1}{G_{12}} - \frac{2\nu_{12}}{E_1}\right)\sin^2\theta\cos^2\theta, \tag{6.2}$$

where

E_x is the elastic modulus along the x-axis (*e.g.*, E_{45} is the elastic modulus along the 45° direction),

E_1 is the elastic modulus along the 0°-bundles,

E_2 is the elastic modulus along the 90°-bundles,

ν_{12} is the Poisson's ratio,

G_{12} is the in-plane shear modulus,

θ is the angle between the principal axis 1 of the ply and the x-direction,

and the mechanical properties of a 5HS C/PPS elementary ply at 120 °C summarized in Table 6.5 [6]. E_1, E_2 and ν_{12} were assumed temperature-independent considering that to the properties of carbon fibres are temperature-independent in the studied temperature range. The influence of fibre orientation on damage variable d computed from the axial stiffness E_{45} of a $\pm 45°$ reference ply is illustrated in Figure 6.24. Table 6.6 summarizes this effect based on the mean residual bundle rotation after the last creep cycle. Only the residual rotation should affect the evaluation of the elastic modulus of the tested specimens. It can be noted that the influence of the residual bundle rotation on d is negligible compared to the value obtained during the 40 and 60 MPa test specimens. Thus, bundle reorientation cannot explain alone the decrease in d (Figure 6.18).

The possible interference between time-dependent behaviour and the evaluation of the elastic modulus was investigated by repeating a CC test at 60 MPa with longer recovery times t_{rec} to minimize unrecovered viscoelastic strains. The recovery time was set at 10 times the creep time, whereas the previous one was only 3 times the creep time. Figure 6.25 shows the damage variable d as a function of the cumulative creep time for all the 60 MPa tests. It can be noted that the test with longer recovery times also exhibits an initial increase quickly followed by a decrease in d. This observation suggests that the origin of this change in d does not result from unrecovered viscoelastic strains. It should be also noted that the test with longer recovery times seems to induce a faster decrease in d as a function of the cumulative creep time. This specimen is exposed to a test temperature of 120 °C in the environmental chamber for a longer time than its counterpart with shorter recovery times. This observation suggests that the decrease in d results from physico-chemical changes. Several physico-chemical mechanisms may contribute to the modification of the material stiffness. Those mechanisms are primarily related to the polymer matrix because carbon fibres are quite stable at 120 °C.

Table 6.5 In-plane mechanical properties of a (0/90) 5HS C/PPS ply at 120 °C [6].

Longitudinal elasticity modulus E_1 (GPa)	Transverse elasticity modulus E_2 (GPa)	Poisson's ratio ν_{12}	Shear modulus G_{12} (GPa)
56.5	56.5	0.042	$4.7 - 0.3\exp^{0.02T}$

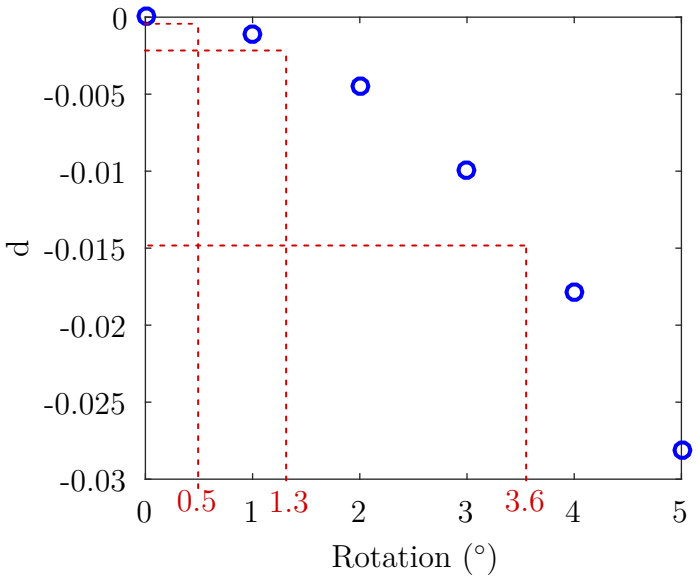

Figure 6.24 Estimation of the effect of bundle rotation on the damage variable d for a 45°-ply.

Table 6.6 Summary of the effect of the mean residual bundle rotation after the last creep cycle on the damage variable d for each stress level. Fibre bundle rotation cannot explained alone the decrease in d.

	40 MPa	60 MPa	100 MPa
Mean residual bundle rotation (°)	0.5	1.3	3.6
Effect on d	-0.0003	-0.0019	-0.0144
d after last creep cycle[1]	-0.0567	-0.1077	0.2029

[1] Mean values

In conclusion, several competing mechanisms may influence the specimen's axial stiffness and thus contribute to the modification of the damage variable d in AP 5HS C/PPS laminates subjected to CC tests at 120 °C:

- damage development, reducing the laminates axial stiffness and increasing d.
- irreversible fibre bundle rotation, increasing the laminates axial stiffness and decreasing d.
- physico-chemical phenomena (*i.e.*, thermal aging), increasing the laminates axial stiffness and decreasing d.

Therefore, the detection of damage development solely through stiffness loss does not seem

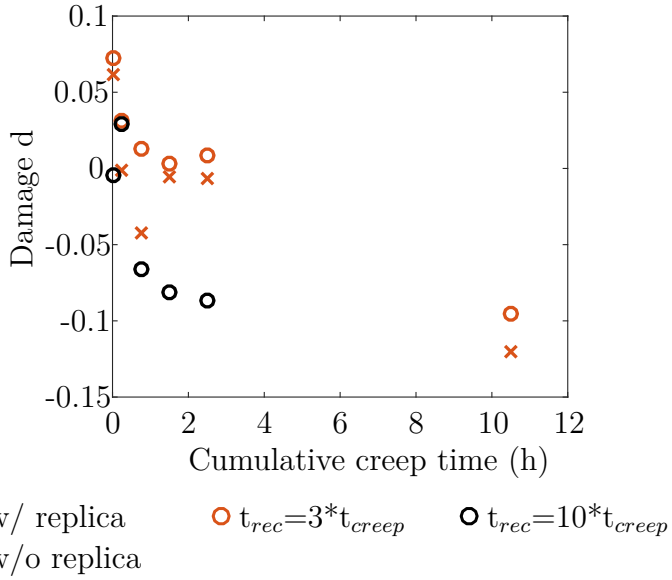

Figure 6.25 Damage variable d as a function of cumulative creep time for several CC tests on AP 5HS C/PPS at 60 MPa and 120 °C. Unrecovered viscoelasticity is not at the origin of the decrease in d. A faster decrease is observed during the test with higher recovery times. It suggest that the decrease results from some thermal aging effect.

suitable for those type of tests. Further investigations is necessary to quantify the respective effects of the different mechanisms on the axial stiffness. The damage variable can still be a qualitative indication along with other monitoring tools.

6.3.2.2 Damage variable, crack density and acoustic emission

The investigation of existing time-dependent damage within C/PPS laminates can be achieved by means of an analysis combining the damage variable d, the crack density and the AE activity as a function of the cumulative creep time for each stress level knowing a priori the different mechanisms (*e.g.*, damage mechanisms, fibre bundle rotation and possible thermal aging) occurring during CC tests at 120 °C. The crack count density is not discussed here, because this method leads to significant uncertainties (*e.g.*, for 100 MPa CC tests), as stated in section 6.2.3.2.

Figures 6.17b and 6.18 show that the cracked surface density and damage variable increase with the cumulative creep time for the CC tests carried out at 100 MPa. However, the 40 and 60 MPa specimens exhibit a stable cracked surface density and a decreasing damage variable which is probably related to thermal aging discussed in the previous section. Thus, damage development is the prominent mechanism at 100 MPa, whereas damage accumulation is either insignificant or not critical during tests at 40 and 60 MPa.

Damage development within laminates needs to be further investigated. Damage development within 100 MPa specimens was highlighted in the last paragraph, but its origin is not fully understood. It could come either from time-dependent phenomena during creep steps (*i.e.*, visco-elasto-plasticity) or from mechanical cycling. AE activity analysis enables to know if damage development occurs either during the loading or the creep steps based on one important assumptions that will be discussed in the next section: the monitored AE signals mainly originates from damage-based sources (*i.e.*, friction-based AE events are not significant). 90% of the AE events and 90% of the AE absolute energy during the loading steps occurs before 1-2 h and 0.75 h of cumulative creep time in the 100 MPa specimens (Figures 6.22b and 6.23b). At the same time the AE activity, in terms of events and energy, during creep steps is slower and reaches 90% only during the last creep cycle (Figures 6.22c and 6.23c). This observation, put into perspective along with the increase in damage variable d and cracked surface density with creep time through the whole tests, suggests that time-dependent damage develops during CC tests at 100 MPa, assuming that most of the monitored AE signals result from damage events and not noise-related sources. It should be noted that, though more AE events were monitored during creep steps, those creep steps are less energetic than loading steps from an AE absolute energy standpoint. This last observation rises questions about the source mechanisms, their extent and their criticality during the different steps of the CC tests.

The results from the 40 and 60 MPa tests indicate no significant damage development based on the damage variable and the crack density, as stated above. However, it does not mean that no time-dependent damage occurred during those tests. Both configurations display an increase in cumulative AE events and cumulative AE absolute energy through the whole tests, especially during creep steps. In addition, it appears that the AE activity in specimens subjected to 60 MPa is one order of magnitude larger than the AE activity in 40 MPa specimens. However, the damage states of both configurations were quite similar. It could either mean that those AE events are noise-related, that the damage characterization methods are not completely appropriate (*e.g.*, microcracking, damage propagation inside the specimens, etc.) or a combination of both. The same issue regarding the unknown physical meaning (*i.e.*, the source mechanisms) of the detected AE events arises. Are those AE events damage-related or simply noise? The AE data presented here are only frequency-based and feature-based ($counts > 3$) filtered during the acquisition and then spatially filtered during post-treatment.

This section gives a better insight into the possible time-dependent damage within C/PPS laminates by means of AE and damage analyses, especially during the CC tests at 100 MPa. However, the conclusions drawn in this section are based on the assumption that AE events primarily reflect damage development though friction-based sources exist during those tests

(*e.g.*, bundle rotation). The next issue to be investigated is to determine the physical mechanisms related to monitored AE signals in order to validate the previous analysis and conclusions.

6.3.2.3 Fibre bundle rotation and acoustic emission

Table 6.7 summarizes the AE activity in terms of events separated into three classes corresponding to the loading steps, the creep steps and the other steps (*i.e.*, unloading, recovery and replication steps) of the tests for each stress level. It appears that about 15% of hits for 40 and 60 MPa tests and 47% of hits for 100 MPa tests do not result from a localized source within a 50 mm centered region. These ratios increase to 71% for 40 and 60 MPa tests and 80% for 100 MPa tests for a 15 mm centered region. As spatial filtering only keeps the signals from the nearest sensor, the 15 mm spatial filtering step rejects about 85% of hits for 40 and 60 MPa specimens and 95% for 100 MPa specimens. A few AE events occur either during unloading or during the recovery steps, but those events represent only about 1.5% of the total events from the 15 mm spatial filtering. It is reasonable to assume that all the AE events from unloading and recovery steps are not damage-related and can be considered as noise. This noise could result from different sources mechanisms:

- inside the zone of interest (*i.e.*, between the two sensors): friction (*e.g.*, crack surface due to crack closing, bundle rotation)
- false positive associated with different outside sources, like friction (*e.g.*, crack closing, bundle rotation, grip), environmental noise (*e.g.*, servo-hydraulic testing machine) or electromagnetic noise.

If the AE events from unloading and recovery steps are assumed to primarily result from friction sources, and especially from fibre bundle rotation, it should be expected that there are at least as many friction-based AE events during loading and creep steps due to the reversible rotation of the fibre bundles. The 40 MPa tests are characterized by very little bundle rotation (less than 2°) which seems to be reversible and time-independent and most likely reversible. Only one AE event is detected during unloading and/or recovery steps during those tests. It occurs during the conditioning cycle, whereas loading steps lead to 22 AE events which mainly appear during the conditioning and the first creep cycles. These observations suggest that there are only a few friction-based AE events during the 40 MPa tests and the AE events from loading and creep steps primarily result from damage sources. Thus, AE events corresponding to creep steps can be related to time-dependent damage in

Table 6.7 Summary of AE activity (*i.e.*, # hits, # events within a 50 mm centered region and # events within a 15 mm centered region) during CC tests on AP 5HS C/PPS at 120 °C for each stress level.

		# hits			# events - 50 mm			# events - 15 mm		
		Load	Creep	Other	Load	Creep	Other	Load	Creep	Other
40 MPa	Avg	168	309	2	74	127	1	22	46	1
	Std	32	53	0	7	8	0	2	3	0
60 MPa	Avg	1944	2829	53	841	1195	24	298	395	10
	Std	40	469	5	11	237	2	50	78	4
100 MPa	Avg	38195	120406	3302	6428	15948	440	2540	5062	118
	Std	33586	134642	3276	474	7120	46	696	1862	3

the 40 MPa case. However, this damage seems to be subcritical considering the evolution of damage variable, as discussed in Section 6.3.2.2.

This conclusion is less obvious in the 60 and 100 MPa tests due to significant fibres bundle rotation (Figure 6.10), which can be related to the increasing cumulative AE events from unloading/recovery steps (Figure 6.22d) that are not observed in the case of CC tests at 40 MPa. However, the proportion of AE events resulting from unloading/recovery steps remains limited (about 1.5%) for all stress levels. This tends to show that friction-based AE events are not significant overall. The observation on the early occurrence of AE events during loading steps (Figure 6.22b) is similar for all stress levels, but with a slower rate as the stress level increases. This could be explained by friction-based AE events.

The previous analysis suggests that: (i) AE events associated with early loading steps mainly result from damage development, (ii) AE events associated with creep steps primarily result from time-dependent damage and (iii) friction-based AE events are relatively insignificant. However, time-dependent damage highlighted by means of AE activity can also be detected by means of others methods (*i.e.*, damage variable and cracked surface density) only for the 100 MPa configuration suggesting that the relevance of each method depends on the severity of damage.

The distribution of a few descriptors of AE events associated with the three different classes can be compared to examine the difference in the AE signal signature (*i.e.*, waveform) in order to filter out friction-based AE events from AE data monitored during loading and creep steps. Those AE events should have the same signature as the one from AE events resulting from unloading/recovery steps. Figures 6.26, 6.27 and 6.28 show Probability Distribution

Function (PDF) for the amplitude, the absolute energy and the duration, respectively, of AE events for the three different classes (*i.e.*, loading, creep and others steps). It appears that the signature of AE events from the unloading/recovery step does not significantly differ from the signature of other AE events (*i.e.*, loading and creep classes). The filtering of AE data with a simple feature-based threshold does not seem to be a relevant solution to filter out the noise-based AE events. The frequency-based distributions (*e.g.*, peak frequency and frequency centroid) are not presented here because a significant amount of AE signals from one of the channels seems to have a flawed frequency response due to an offset, whose origin is unclear. In addition, broadband sensors should have been used to analyze frequency features. Information can still be obtain from those distributions. It seems that higher stress levels result in monitoring of a few friction-based AE events with higher amplitude, higher absolute energy and higher duration. Those events may result from larger fibres bundle rotation due to the more extensive metadelamination as stress level increases. Finally, a multivariate clustering would be necessary to filter out friction-based AE events.

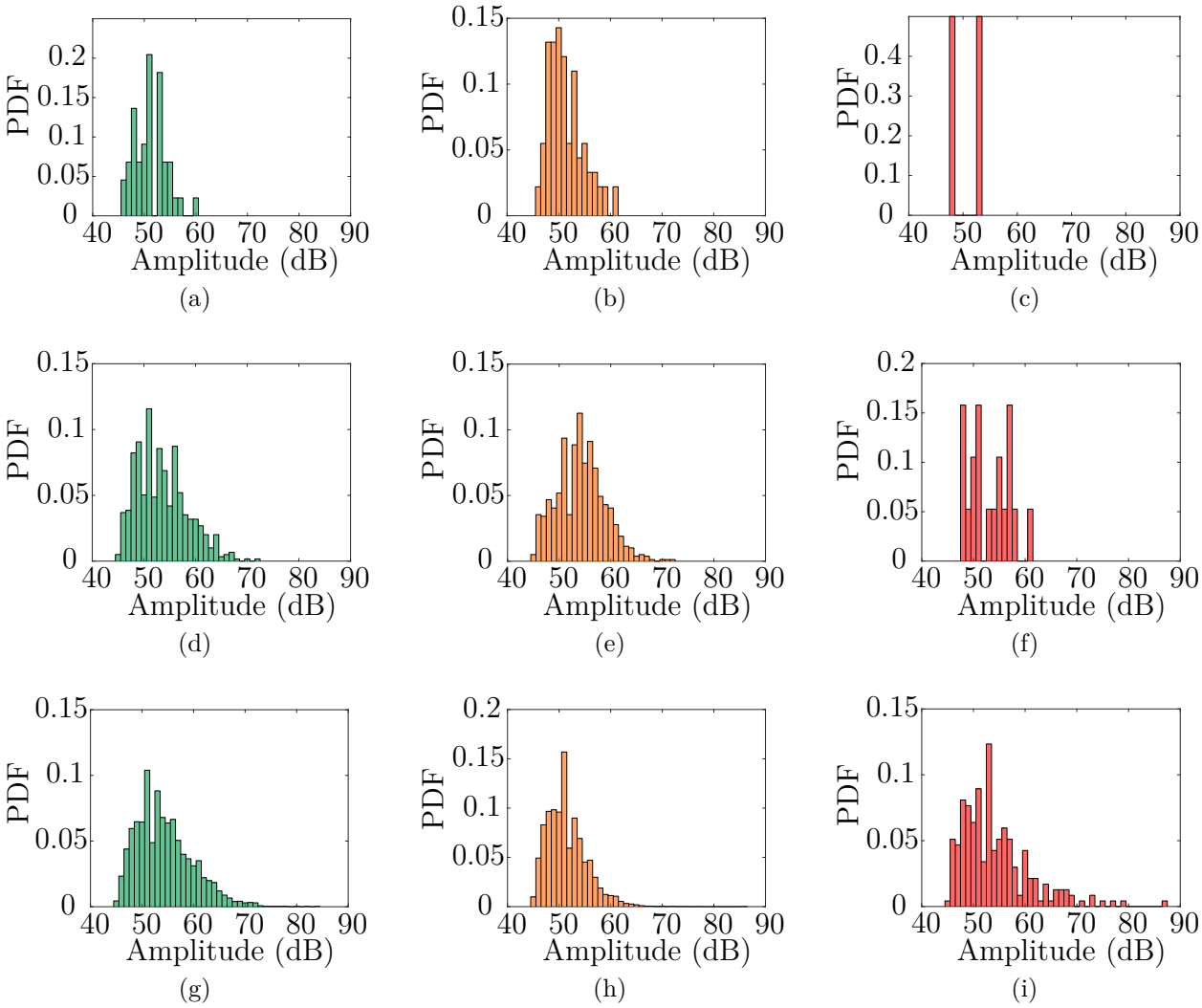

Figure 6.26 PDF of the AE events' amplitude from the three different classes (*i.e.*, (a)(d)(g) loading, (b)(e)(h) creep and (c)(f)(i) unloading/recovery stages) during CC tests on AP 5HS C/PPS at 120 °C for each stress level (*i.e.*, (a)(b)(c) 40, (d)(e)(f) 60 and (g)(h)(i) 100 MPa)

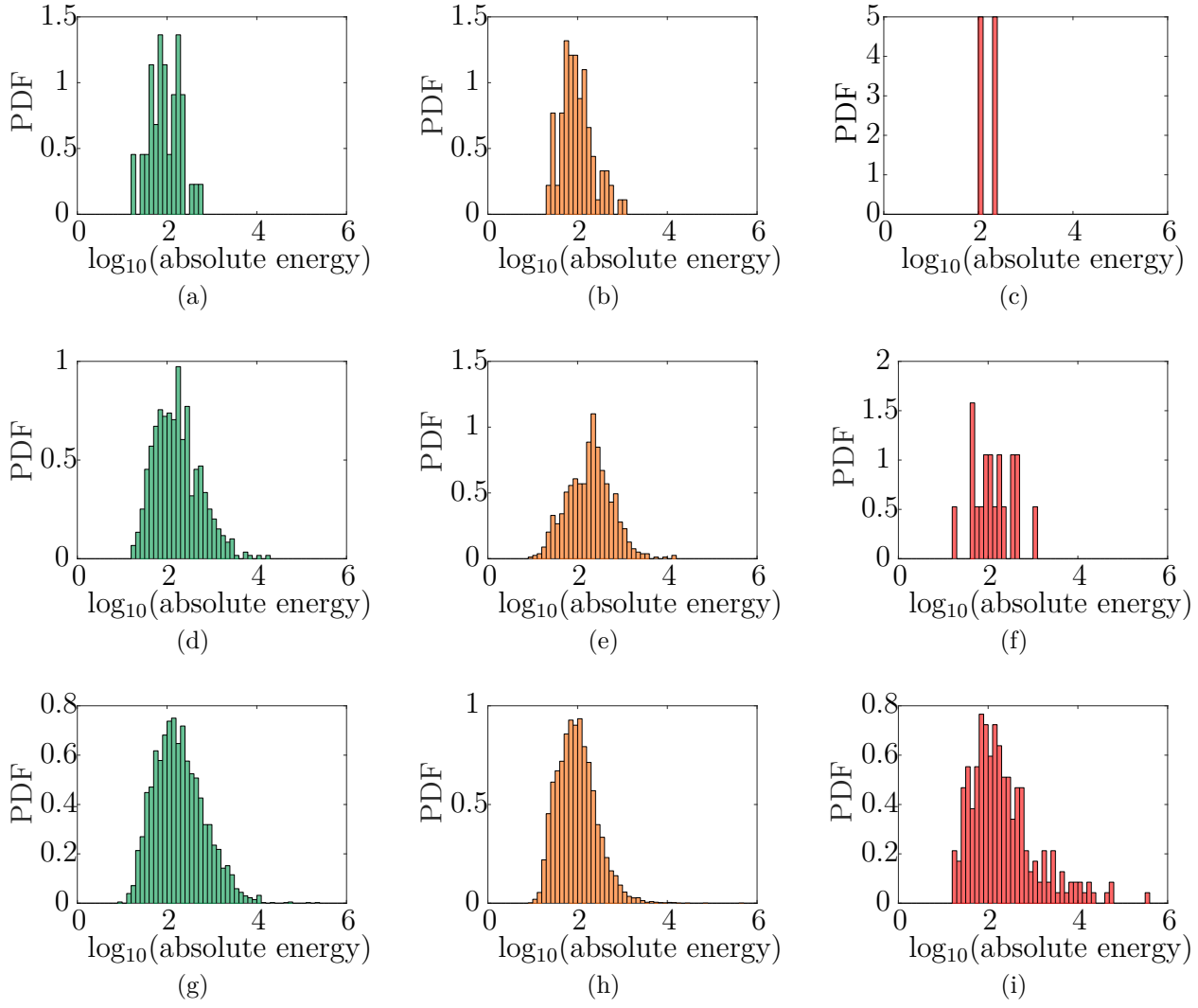

Figure 6.27 PDF of the AE events' absolute energy from the three different classes (*i.e.*, (a)(d)(g) loading, (b)(e)(h) creep and (c)(f)(i) unloading/recovery stages) during CC tests on AP 5HS C/PPS at 120 °C for each stress level (*i.e.*, (a)(b)(c) 40, (d)(e)(f) 60 and (g)(h)(i) 100 MPa)

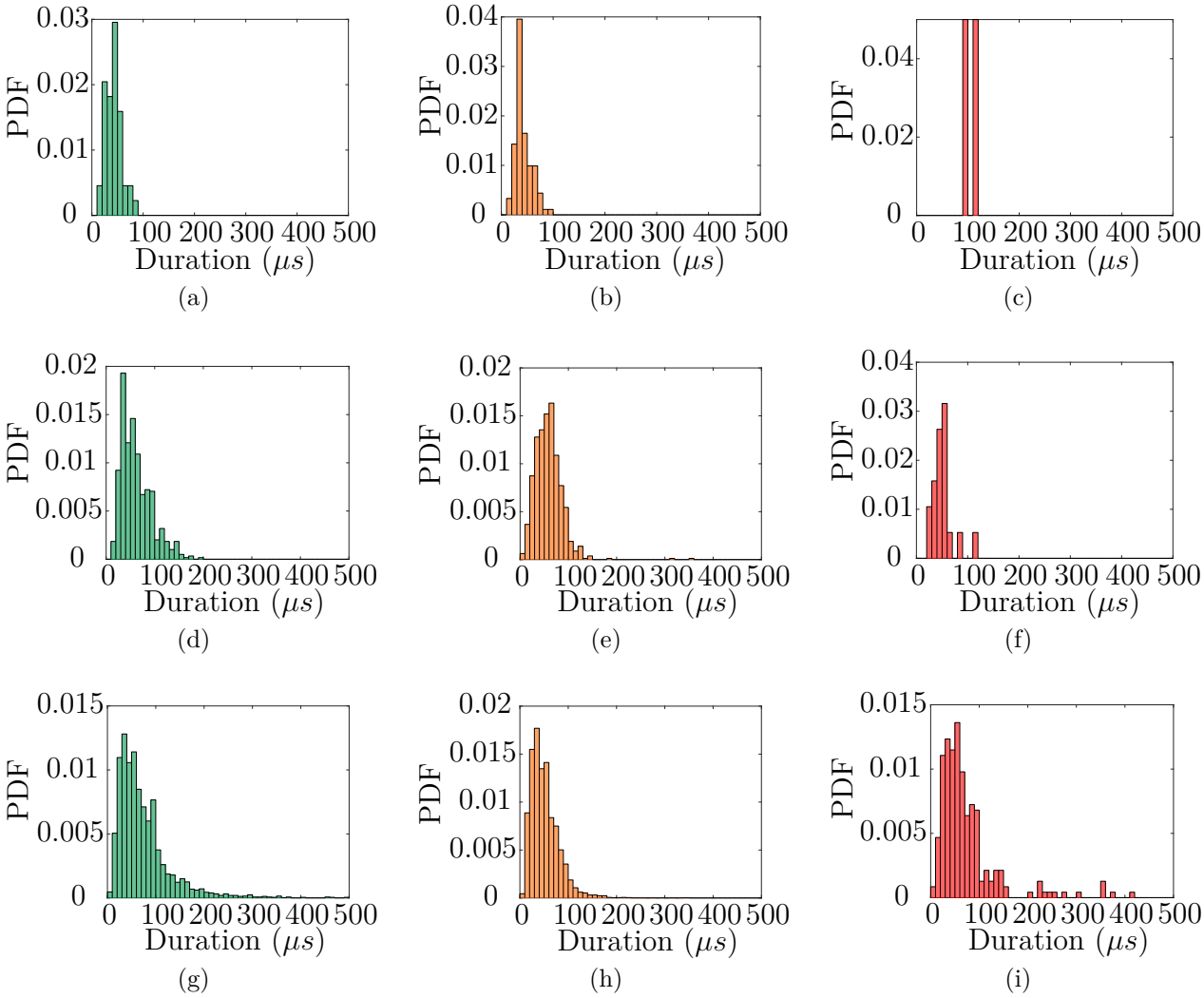

Figure 6.28 PDF of the AE events' duration from the three different classes (*i.e.*, (a)(d)(g) loading, (b)(e)(h) creep and (c)(f)(i) unloading/recovery stages) during CC tests on AP 5HS C/PPS at 120 °C for each stress level (*i.e.*, (a)(b)(c) 40, (d)(e)(f) 60 and (g)(h)(i) 100 MPa)

6.4 Conclusions and perspectives

6.4.1 Conclusions

The purpose of this chapter was to investigate possible time-dependent damage in AP 5HS C/PPS laminates whose behaviour is primarily matrix-dominated. Mechanical tests being conducted at 120 °C > T_g, matrix ductile and time-dependent behaviours are enhanced. By means of cyclic creep tests and different experimental methods (damage variable, microscopic observations and AE monitoring), time-dependent damage is specifically addressed. At first the different monitoring tools were analyzed independently to identify all the mechanisms operating during CC tests at different stress levels. Then, an analysis combining different physical data was performed in order to draw conclusions about time-dependent damage development within the studied laminates.

It appears that all stress levels (*i.e.*, 40, 60 and 100 MPa) exhibit a visco-elasto-plastic behaviour. Furthermore, fibre bundle rotation is observed to a certain extent at all stress levels. The bundle rotation of specimens subjected to 40 and 60 MPa is mainly reversible and time-independent, whereas the 100 MPa tests are characterized by time-dependent reversible and irreversible bundle rotations. Differences between stress levels are also observed in terms of damage. Higher stress levels induce higher cracked surface densities. However, crack count densities corresponding to 40 MPa and 60 MPa tests are about the same, whereas the 100 MPa tests result in higher crack counts. This difference between the 40/60 MPa and 100 MPa tests can also be put into light when considering a macroscopic damage variable d. Two main damage mechanisms are identified: intra-bundle cracking and inter-bundle cracking leading to meta-delamination. Higher stress levels may induce more inter-bundle cracking, which which comes along with larger fibre bundle rotation, and wider cracks in general. Furthermore, a physico-chemical phenomenon (*i.e.*, thermal aging) is expected to explain the decrease in the damage variable d during the 40 and 60 MPa tests.

All the previously mentioned mechanisms occurred simultaneously during the CC tests making the investigation of time-dependent damage very challenging. Time-dependent damage was mainly highlighted combining three complementary experimental methods: damage variable, cracked surface density and AE activity. Fibre bundle rotation is also taking into account to provide a better insight into the AE source mechanisms taking place during the tests. It is observed that time-dependent damage occurs during CC tests for all stress levels, but to a certain extent. It is easily deduced from the increases in damage variable and cracked surface density for the 100 MPa tests, unlike what is observed in the 40 and 60 MPa specimens. Furthermore, AE monitoring highlights a time-dependent increase in AE activity

during the creep steps for all stress levels, confirming the conclusions drawn at 100 MPa. It also confirms the development of time-dependent damage in the case of specimens subjected to 40 and 60 MPa. However, this time-dependent damage is subcritical at 40 and 60 MPa, as illustrated by the decrease in the damage variable due to a competing physico-chemical phenomenon which tends to increase the material stiffness.

One important assumption is made to draw this conclusion. It is assumed that the majority of the recorded AE events results from damage-based sources, and thus that noise-based sources, especially friction-based ones, are insignificant, whereas bundle rotation is observed to a certain extent at all stress levels. This assumption is partially confirmed by the very low proportion of AE events occurring during the unloading/recovery steps, which was about 1.5% for each stress level. In any case, the noise-related AE events need to be removed in order to analyze more accurately time-dependent damage using a clustering analysis to identify the different damage mechanisms (*i.e.*, mainly intra-bundle cracking and inter-bundle cracking) and monitor their growth. The filtering of AE data with a simple feature-based threshold did not seem to be a correct solution to filter out the noise-based AE events. An unsupervised clustering algorithm can be used to verify if the noise-related events are naturally clustered in the same class, and then remove them. If this is not the case, one can imagine using an equivalent unsupervised clustering algorithm by initializing one of the class centroids at the centroid of the AE events from the unloading/recovery steps to verify if there is a local minimum.

6.4.2 Perspectives

Overall, this combined analysis highlights the difficulty to characterize damage (time-dependent or not) and quantify its growth within AP 5HS C/PPS laminates, whose behaviour is characterized by simultaneous phenomena. Several other improvements should be considered to further investigate the time-dependent damage within AP 5HS C/PPS laminates, namely:

- The air-annealing of the specimens at 120 °C before conducting mechanical tests to minimize the effect of physico-chemical phenomena on the material stiffness, and thus the decrease in damage variable. The annealing time can be estimated through isotherm DMA.

- To perform CC tests at ambient temperature if the previous point is not applicable. A particular interest should be given to physical aging. In-situ tomographic observations could be considered.

- To conduct tests at other stress levels, *e.g.* 80 MPa or close the ultimate strength.

The 80 MPa stress level would enable to obtain an intermediate response between 40/60 MPa and 100 MPa. Stress levels close to the ultimate strength may result in creep fracture.

- To carry out tests for longer creep times.
- To improve the crack density estimation method.
- To use broadband sensors to verify if a frequency-based filtering is possible.
- To optimize the AE acquisition parameters, such as the pre-amplifier gain, which may be too low.
- To use an unsupervised clustering algorithm (*e.g.*, k-mean) to verify if the different AE sources can be classified properly.

Finally, CC tests should also be performed on QI and/or cross-ply laminates though a limited visco-elasto-plastic behaviour is expected. Those tests would deliver a better insight of time-dependent damage within 5HS C/PPS laminates and its relation with visco-elasto-plastic behaviour. Testing QI or cross-ply laminates should have some advantages:

- Less or no structural effect, such as fibre bundle rotation, resulting in less friction-based AE sources.
- Monitoring other damage mechanisms, such as fibre breakage during tests at high stress levels.

However, those tests may need some additional precautions, such as a non stiffness-based macroscopic damage variable. Indeed, on-axis testing exhibits limited decrease in axial stiffness, as mentioned in Section 2.2.1. Thus, a damage variable based on Poisson's ratio may be a relevant approach, though it requires the use of two extensometers or DIC.

CHAPTER 7 CONCLUSION AND PERSPECTIVES

The work presented in this thesis was motivated by several previous studies dealing with the thermomechanical behaviour of 5HS C/PPS laminates that have been conducted in our laboratory [5, 6]. These studies raised questions on the time-dependent damage within woven laminates. Different time-dependent softening/hardening phenomena occur within polymer composites; such as mechanical softening (*e.g.*, viscoelasticity, viscoplasticity, damage), physico-chemical (*e.g.*, physical aging, thermal aging) and structural (*e.g.*, fibre bundle rotation) phenomena. The separation and the identification of each mechanism are important durability issues to understand the long-term behaviour of woven PMCs, particularly when TP-based laminates are subjected to mechanical loadings at $T > T_g$. More specifically this thesis focuses on the detection and investigation of time-dependent damage development and other conjoint mechanisms within 5HS C/PPS laminates at 120 °C, which is a common service temperature for aircraft engine nacelles.

7.1 Summary of works

The first experimental campaign investigated the influence of time-dependent phenomena on the translaminar fracture of angle-ply and quasi-isotropic 5HS C/PPS SEN specimens in tension at 120 °C. It appeared that critical damage mechanisms resulting in ultimate failure were not influenced by time-dependent phenomena for both stacking sequences. The QI specimens' failure is time-independent mainly due to the fibre-dominated behaviour. This time-independent fracture seems to be also observed in the AP case, even though the matrix should have a greater role on the macroscopic behaviour, when compared to solicitations along the fibre bundle direction. However, it seems that time-dependent mechanisms rather influence the early stage of damage. Furthermore, a significant amount of AE events were detected during creep steps for both stacking sequences. If those AE sources are related to time-dependent damage, time-dependent damage development seems subcritical. This last observation led to the second part of this work.

The second experimental study focused on the investigation of this possible time-dependent damage development during creep. Cyclic creep tests were performed on unnotched 5HS C/PPS angle-ply specimens at 120 °C and three different stress levels: 40, 60 and 100 MPa. Those tests were developed to monitor conjointly the different mechanisms occurring within AP laminates during creep tests, *e.g.*, viscoelasticity, viscoplasticity, damage development and fibre bundle rotation. Damage development was monitored through several techniques:

AE, edge replication, stiffness-based damage variable and ex-situ XμCT. All stress levels displayed a visco-elasto-plastic behaviour. However, only the specimens subjected to 100 MPa exhibited time-dependent reversible and irreversible bundle rotations. The other specimens mainly exhibited time-independent reversible rotations. Furthermore, another significant difference between 40/60 MPa and 100 MPa stress levels was observed concerning damage development. The higher stress level induced higher crack densities which was in accordance with a higher damage variable. Two main damage mechanisms occurred for each stress level: intra-bundle and inter-bundle cracking (*e.g.*, meta-delamination). However, the 100 MPa stress level seemed to exhibit more inter-bundle cracking, which is also related to higher fibre bundle rotation. It seemed that only the 100 MPa tests displayed time-dependent damage development based on the damage variable d and the cracked surface density. However, time-dependent damage may also developed in specimens at 40 and 60 MPa according to the increasing AE activity during the creep steps and assuming that those AE sources are damage-related, which is plausible based on the comparison with the insignificant friction-based AE activity during unloading and recovery stages. This time-dependent damage seemed to be subcritical for 40 and 60 MPa based on the damage variable d and the crack densities. Furthermore, the specimens subjected to 40 and 60 MPa highlighted a possible competitive time-dependent physico-chemical phenomenon due to thermal aging which stiffened the material, as highlighted by the decrease of the damage variable d.

To summarize the contribution of this PhD, it seems that the translaminar fracture of AP and QI 5HS C/PPS at 120 °C ($> T_g^{C/PPS}$) is not influenced by time-dependent phenomena occurring during incremental load-unload solicitations. However, some AE observations indicated possible time-dependent damage during creep stages. Those observations were confirmed by means of cyclic creep tests conducted on AP 5HS C/PPS laminates. Those tests were performed at 120 °C and three stress levels (40, 60 and 100 MPa). A coupled approach was used to characterize and isolate the different time-dependent mechanisms. The characterization method developed in this study enabled to point out time-dependent damage for the three tested stress level and its influence on the axial stiffness, as well as a possible competitive time-dependent physico-chemical phenomenon due to thermal aging which stiffened the material.

7.2 Future research

7.2.1 Influence of time-dependent phenomena on damage development

From the experimental characterization standpoint, several improvements should be considered to further investigate this coupling. Several changes concerning the fracture mechanics-based approach are required to obtain more quantitative and accurate results:

- Firstly, the development of a stable crack growth is necessary to study the influence of time-dependent phenomena on the crack propagation. Furthermore, it may reduce the undesired failure mechanisms, such as the significant interlaminar failure during the tests in AP specimens. This point can be solved by using another specimen geometries (*e.g.*, compact tension) and by performing displacement-controlled tests.
- Secondly, to perform monotonic tests instead of incremental load-unload tests to remain within the EPFM assumptions.
- Lastly, DIC or IR thermography are complementary techniques to determine the macro-crack initiation and to follow the crack tip along with AE monitoring.

The second experimental campaign highlighted several points that need to be addressed:

- Thermal aging of the PPS matrix at 120 °C. This aging tends to stiffen the matrix [114,115], which interferes with the determination of the stiffness-based damage variable d. One way to minimize the effect of this physico-chemical phenomena on stiffness is to achieve air-annealing at 120 °C on the specimens before the CC tests.
- The source of the time-dependent damage development observed in the increasing variable d and the increasing cracked surface density during 100 MPa tests is not fully characterized. It seemed that the crack count density of intra-bundle cracks remained constant or at least in the incertitude range. A surface information of damage on the edges may not be enough to fully characterize this time-dependent damage development. One might consider interrupted creep tests at different creep time coupled with either cross-sectioning or XμCT (ex-situ at 120 °C or in-situ at RT), but this type of tests can become quickly expensive for several stress levels. The use of AE monitoring followed by a multivariate approach such as an unsupervised clustering algorithm (*e.g.*, k-means++) should also be attempted to discriminate the different mechanisms and to filtered out noise-based events.

- The 40 and 60 MPa stress levels exhibited relatively similar behaviours, when compared to the 100 MPa stress level. Other intermediate stress levels might be needed, as well as levels above 100 MPa to observe more severe damage development and possibly creep rupture. However, the higher the stress level is, the higher the risk of monitoring friction-based AE events due to fibre bundle rotation is.

This last experimental study focused only on time-dependent damage within AP laminates. Those tests should also be performed on on-axis (*e.g.*, QI and [(0/90)]) specimens to verify if possible time-dependent damage occurs, though a limited visco-elasto-plastic behaviour is expected. Furthermore, comparing the AE results of on-axis and AP specimens may ease the interpretation of the AE analyses and the clustering of AE signatures. Indeed, on-axis specimens may result in less friction-based AE sources and different damage chronologies (*e.g.*, occurrence of fibre breakage). However, this comparison should be considered with caution as the propagation medium's properties are anisotropic, which should altered the AE waves differently.

Another relevant aspect to be investigated is the influence of the weave pattern on the visco-elasto-plastic behaviour (*e.g.*, during creep tests) and the possible influence of the mesoscopic geometric features on time-dependent damage development. Gupta and Raghavan [28] noticed that a higher crimp angle resulted in a higher creep compliance and a higher creep rate. This crimp angle depends on the weave pattern, among other parameters. Furthermore, Osada et al. [17] and Montesano et al. [26] noted that the damage threshold was delayed for weave pattern with less crimp regions.

7.2.2 Influence of damage on viscoelastic behaviour

Since this work focused on the influence of time-dependent phenomena on damage development (*i.e.*, time-dependent damage development), the next step would be to experimentally observe the influence of the damage state on the time-dependent behaviour (*e.g.*, viscoelasticity) of woven PMCs, *i.e.*, to correlate specific damage mechanisms with the change in the macroscopic visco-elasto-plastic behaviour of woven TP-based laminates.

An approach based on the work by Bocchieri [69] is proposed in Figure 7.1. Three damage states are generated via cyclic creep conditioning on the same specimen. Then, each conditioning is followed by a damage characterization step through edge replicas for example. Finally, the viscoelastic response is investigated for stresses lower or equal to the stress used to induce the given damage state.

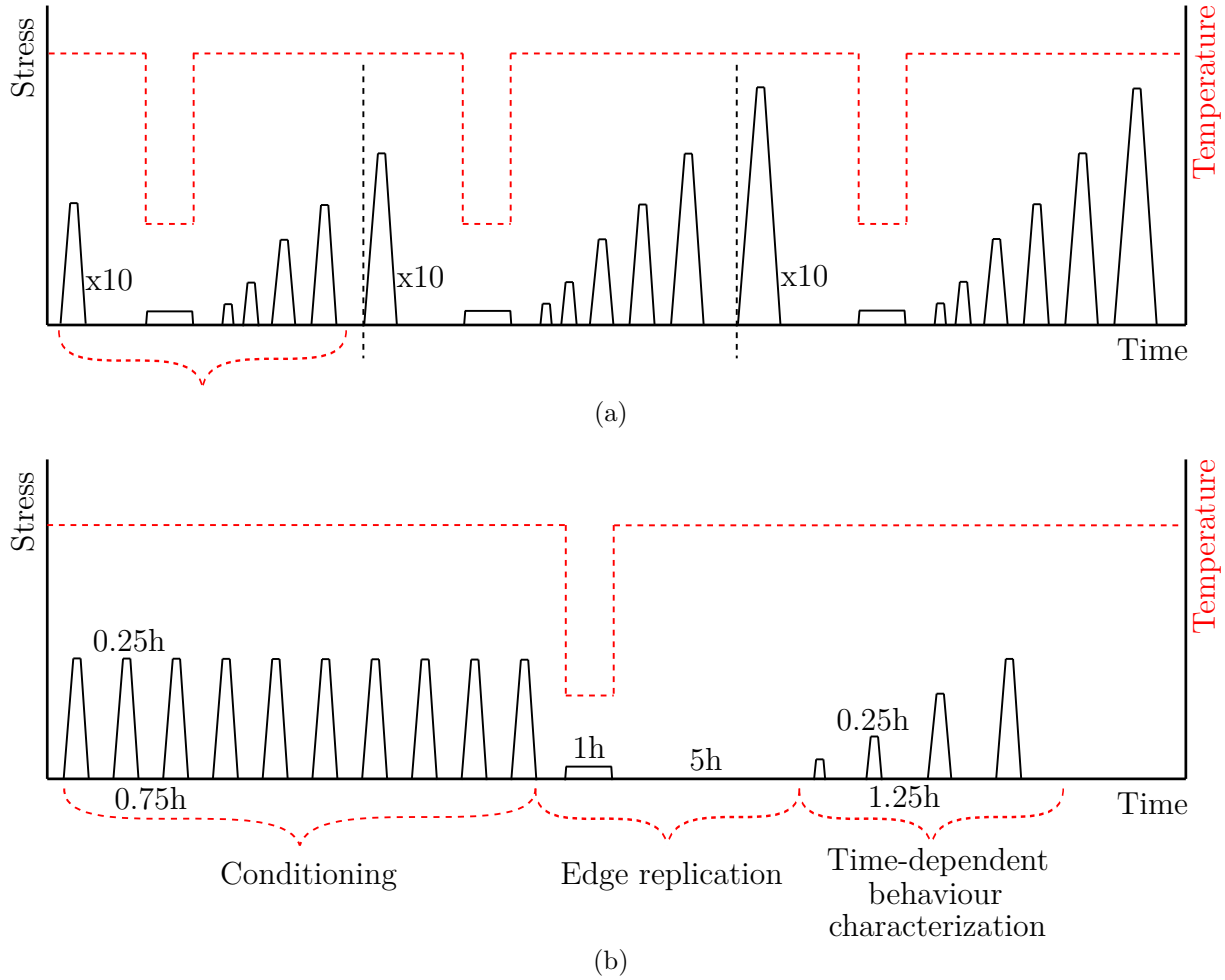

Figure 7.1 (a) Protocol of the damage effect study on the macroscopic viscoelastic behaviour (based on [69]) with three damage states. (b) Zoom on one damage state of the previous protocol.

REFERENCES

[1] Group of Personalities, "European aeronautics: a vision for 2020," European Commission, Tech. Rep., 2001.

[2] High Level Group on Aviation Research, "Flightpath 2050: Europe's vison for aviation," European Commission, Tech. Rep., 2011.

[3] A. C. Long, "Introduction," in *Design and Manufacture of Textile Composites*, ser. Woodhead Publishing Series in Textiles, A. C. Long, Ed. Woodhead Publishing, Jan. 2005, pp. xiii–xvi.

[4] J.-K. Kim and M.-L. Sham, "Impact and delamination failure of woven-fabric composites," *Composites Science and Technology*, vol. 60, no. 5, pp. 745–761, Apr. 2000. [Online]. Available: http://www.sciencedirect.com/science/article/pii/S0266353899001669

[5] J. Aucher, "Etude comparative du comportement composites à matrice thermoplastique ou thermodurcissable," PhD dissertation, Dép. mécanique, INSA de Rouen, Rouen, Dec. 2009. [Online]. Available: https://tel.archives-ouvertes.fr/tel-00557897/document

[6] W. Albouy, "De la contribution de la visco-élasto-plasticité au comportement en fatigue de composites à matrice thermoplastique et thermodurcissable," PhD dissertation, Dép. mécanique, INSA de Rouen, Rouen, Nov. 2013. [Online]. Available: http://www.theses.fr/2013ISAM0021

[7] B. Vieille *et al.*, "Prediction of the notched strength of woven-ply PolyPhenylene Sulfide thermoplastic composites at a constant high temperature by a physically-based model," *Composite Structures*, vol. 153, pp. 529–537, Oct. 2016. [Online]. Available: https://www.sciencedirect.com/science/article/pii/S0263822316310133

[8] W. Albouy and B. Vieille, "Determination of the damage threshold in woven-ply thermoplastic laminates at T>Tg: Acoustic emission and microscopic damage analysis," *Composites Part B: Engineering*, vol. 64, pp. 138–146, Aug. 2014. [Online]. Available: http://www.sciencedirect.com/science/article/pii/S1359836814001826

[9] D. Bouscarrat, M. Levesque, and B. Vieille, "Influence of time-dependent phenomena on translaminar fracture of woven-ply C/PPS laminates above the glass transition

temperature," *Composites Part B: Engineering*, p. 107561, Oct. 2019. [Online]. Available: http://www.sciencedirect.com/science/article/pii/S1359836819321821

[10] J.-M. Berthelot, *Matériaux composites: comportement mécanique et analyse des structures*, 4th ed. Tec et Doc, 2005.

[11] F. C. Campbell, *Structural Composite Materials*. ASM International, 2010.

[12] C. Sauder, J. Lamon, and R. Pailler, "Thermomechanical properties of carbon fibres at high temperatures (up to 2000c," *Composites Science and Technology*, vol. 62, no. 4, pp. 499–504, Mar. 2002. [Online]. Available: http://www.sciencedirect.com/science/article/pii/S0266353801001403

[13] P. Combette and I. Ernoult, *Physique des polymères: Propriétés mécaniques*. Hermann, 2005.

[14] R. A. Schapery, "On the characterization of nonlinear viscoelastic materials," *Polymer Engineering & Science*, vol. 9, no. 4, pp. 295–310, Jul. 1969. [Online]. Available: http://onlinelibrary.wiley.com/doi/10.1002/pen.760090410/abstract

[15] J. Lemaitre *et al.*, *Mécanique des matériaux solides*, 3rd ed. Dunod, 2009.

[16] I. M. Daniel, J.-J. Luo, and P. M. Schubel, "Three-dimensional characterization of textile composites," *Composites Part B: Engineering*, vol. 39, no. 1, pp. 13–19, Jan. 2008. [Online]. Available: http://www.sciencedirect.com/science/article/pii/S1359836807000327

[17] T. Osada, A. Nakai, and H. Hamada, "Initial fracture behavior of satin woven fabric composites," *Composite Structures*, vol. 61, no. 4, pp. 333–339, Sep. 2003. [Online]. Available: http://www.sciencedirect.com/science/article/pii/S0263822303000588

[18] S. D. Pandita *et al.*, "Tensile fatigue behaviour of glass plain-weave fabric composites in on- and off-axis directions," *Composites Part A: Applied Science and Manufacturing*, vol. 32, no. 10, pp. 1533–1539, Oct. 2001. [Online]. Available: http://www.sciencedirect.com/science/article/pii/S1359835X01000537

[19] J. Montesano *et al.*, "Elevated temperature off-axis fatigue behavior of an eight-harness satin woven carbon-fiber/bismaleimide laminate," *Composites Part A: Applied Science and Manufacturing*, vol. 43, no. 9, pp. 1454–1466, Sep. 2012. [Online]. Available: http://www.sciencedirect.com/science/article/pii/S1359835X12001455

[20] J. Bassery, "Prise en compte du vieillissement et de la fatigue dans le dimensionnement de structures en matériaux composites," PhD dissertation, École Nationale Supérieure des Mines de Paris, Paris, Jun. 2011. [Online]. Available: https://pastel.archives-ouvertes.fr/pastel-00609158/document

[21] P. Carnevale, "Fibre-matrix interfaces in thermoplastic composites: A meso-level approach," PhD dissertation, Aerospace Engineering: Aerospace Structures and Materials, TU Delft, Delft University of Technology, Delft, Feb. 2014. [Online]. Available: http://resolver.tudelft.nl/uuid:880605ea-fb4c-4b9b-a25e-ad610d94a5cd

[22] J. Yang *et al.*, "The effect of off-axis angles on the mesoscale deformation response and failure behavior of an orthotropic textile carbon-epoxy composite," *Composite Structures*, vol. 206, pp. 952–959, Dec. 2018. [Online]. Available: http://www.sciencedirect.com/science/article/pii/S0263822318310596

[23] B. Vieille and L. Taleb, "About the influence of temperature and matrix ductility on the behavior of carbon woven-ply PPS or epoxy laminates: Notched and unnotched laminates," *Composites Science and Technology*, vol. 71, no. 7, pp. 998–1007, May 2011. [Online]. Available: http://www.sciencedirect.com/science/article/pii/S0266353811000960

[24] M. Kawai and T. Taniguchi, "Off-axis fatigue behavior of plain weave carbon/epoxy fabric laminates at room and high temperatures and its mechanical modeling," *Composites Part A: Applied Science and Manufacturing*, vol. 37, no. 2, pp. 243–256, Feb. 2006. [Online]. Available: http://www.sciencedirect.com/science/article/pii/S1359835X05002824

[25] A. Gupta and J. Raghavan, "Creep of plain weave polymer matrix composites under on-axis and off-axis loading," *Composites Part A: Applied Science and Manufacturing*, vol. 41, no. 9, pp. 1289–1300, Sep. 2010. [Online]. Available: http://www.sciencedirect.com/science/article/pii/S1359835X10001545

[26] J. Montesano, Z. Fawaz, and H. Bougherara, "Non-destructive assessment of the fatigue strength and damage progression of satin woven fiber reinforced polymer matrix composites," *Composites Part B: Engineering*, vol. 71, pp. 122–130, Mar. 2015. [Online]. Available: http://www.sciencedirect.com/science/article/pii/S1359836814005174

[27] M. A. V. Rui Miranda Guedes, "Comparison of Creep Behavior of UD and Woven CFRP in Bending," *Mechanics of Composite Materials and Structures*, vol. 8, no. 2, pp. 119–134, Apr. 2001. [Online]. Available: https://doi.org/10.1080/10759410118348

[28] A. Gupta and J. Raghavan, "Parametric study of the effect of microstructure on creep of plain weave composites," *Composites Part A: Applied Science and Manufacturing*, vol. 42, no. 5, pp. 511–520, May 2011. [Online]. Available: http://www.sciencedirect.com/science/article/pii/S1359835X11000273

[29] T. Matsuda *et al.*, "Elastic–viscoplastic behavior of plain-woven GFRP laminates: Homogenization using a reduced domain of analysis," *Composite Structures*, vol. 79, no. 4, pp. 493–500, Aug. 2007. [Online]. Available: http://www.sciencedirect.com/science/article/pii/S0263822306000559

[30] T. Fujii, S. Amijima, and K. Okubo, "Microscopic fatigue processes in a plain-weave glass-fibre composite," *Composites Science and Technology*, vol. 49, no. 4, pp. 327–333, 1993. [Online]. Available: http://www.sciencedirect.com/science/article/pii/026635389390063M

[31] F. Gao *et al.*, "Damage accumulation in woven-fabric CFRP laminates under tensile loading: Part 1. Observations of damage accumulation," *Composites Science and Technology*, vol. 59, no. 1, pp. 123–136, Jan. 1999. [Online]. Available: http://www.sciencedirect.com/science/article/pii/S0266353897002315

[32] W. Albouy, B. Vieille, and L. Taleb, "Experimental and numerical investigations on the time-dependent behavior of woven-ply PPS thermoplastic laminates at temperatures higher than glass transition temperature," *Composites Part A: Applied Science and Manufacturing*, vol. 49, pp. 165–178, Jun. 2013. [Online]. Available: http://www.sciencedirect.com/science/article/pii/S1359835X13000717

[33] A. Doitrand, "Endommagement à l'échelle mésoscopique et son influence sur la tenue mécanique des matériaux composites tissés," PhD dissertation, Université de Bretagne occidentale, Brest, Nov. 2016. [Online]. Available: https://hal.archives-ouvertes.fr/tel-01455235/document

[34] S. V. Lomov *et al.*, "Experimental methodology of study of damage initiation and development in textile composites in uniaxial tensile test," *Composites Science and Technology*, vol. 68, no. 12, pp. 2340–2349, Sep. 2008. [Online]. Available: http://www.sciencedirect.com/science/article/pii/S0266353807002801

[35] A. El Mourid, "Mechanical Behavior of a Triaxially Braided Textile Composite at High Temperature," PhD dissertation, Dép. de génie mécanique, École Polytechnique de Montréal, Montreal, Oct. 2014. [Online]. Available: http://publications.polymtl.ca/1562/

[36] S. Daggumati *et al.*, "Local damage in a 5-harness satin weave composite under static tension: Part I – Experimental analysis," *Composites Science and Technology*, vol. 70, no. 13, pp. 1926–1933, Nov. 2010. [Online]. Available: http://www.sciencedirect.com/science/article/pii/S0266353810002605

[37] S. G. Ivanov *et al.*, "Damage development in woven carbon fibre thermoplastic laminates with PPS and PEEK matrices: A comparative study," *Journal of Composite Materials*, vol. 51, no. 5, pp. 637–647, Mar. 2016. [Online]. Available: https://doi.org/10.1177/0021998316653460

[38] L. Li, S. V. Lomov, and X. Yan, "Correlation of acoustic emission with optically observed damage in a glass/epoxy woven laminate under tensile loading," *Composite Structures*, vol. 123, pp. 45–53, May 2015. [Online]. Available: http://www.sciencedirect.com/science/article/pii/S0263822314006850

[39] T. Lisle *et al.*, "Damage analysis and fracture toughness evaluation in a thin woven composite laminate under static tension using infrared thermography," *Composites Part A: Applied Science and Manufacturing*, vol. 53, pp. 75–87, Oct. 2013. [Online]. Available: http://www.sciencedirect.com/science/article/pii/S1359835X13001644

[40] ——, "Damage of woven composite under translaminar cracking tests using infrared thermography," *Composite Structures*, vol. 161, pp. 275–286, Feb. 2017. [Online]. Available: http://www.sciencedirect.com/science/article/pii/S0263822316313964

[41] M. Naderi, A. Kahirdeh, and M. M. Khonsari, "Dissipated thermal energy and damage evolution of Glass/Epoxy using infrared thermography and acoustic emission," *Composites Part B: Engineering*, vol. 43, no. 3, pp. 1613–1620, Apr. 2012. [Online]. Available: http://www.sciencedirect.com/science/article/pii/S1359836811003362

[42] B. Vieille and W. Albouy, "Fatigue damage accumulation in notched woven-ply thermoplastic and thermoset laminates at high-temperature: Influence of matrix ductility and fatigue life prediction," *International Journal of Fatigue*, vol. 80, pp. 1–9, Nov. 2015. [Online]. Available: http://www.sciencedirect.com/science/article/pii/S0142112315001358

[43] B. Vieille *et al.*, "High-temperature fatigue behaviour of notched quasi-isotropic thermoplastic and thermoset laminates: Influence of matrix ductility on damage mechanisms and stress distribution," *Composite Structures*, vol. 153, pp. 311–320, Oct. 2016. [Online]. Available: http://www.sciencedirect.com/science/article/pii/S026382231630842X

[44] B. Yu *et al.*, "2d and 3d imaging of fatigue failure mechanisms of 3d woven composites," *Composites Part A: Applied Science and Manufacturing*, vol. 77, pp. 37–49, Oct. 2015. [Online]. Available: http://www.sciencedirect.com/science/article/pii/S1359835X15002122

[45] R. Böhm *et al.*, "A quantitative comparison of the capabilities of in situ computed tomography and conventional computed tomography for damage analysis of composites," *Composites Science and Technology*, vol. 110, pp. 62–68, Apr. 2015. [Online]. Available: http://www.sciencedirect.com/science/article/pii/S0266353815000585

[46] M. G. R. Sause, *In Situ Monitoring of Fiber-Reinforced Composites: Theory, Basic Concepts, Methods, and Applications*, ser. Springer Series in Materials Science. Springer International Publishing, 2016.

[47] S. Huguet, "Application de classificateurs aux données d'émission acoustique : identification de la signature acoustique des mécanismes d'endommagement dans les composites à matrice polymère," PhD dissertation, INSA Lyon, Lyon, Jan. 2002. [Online]. Available: http://www.theses.fr/2002ISAL0087

[48] G. N. Morscher, "Modal acoustic emission of damage accumulation in a woven SiC/SiC composite," *Composites Science and Technology*, vol. 59, no. 5, pp. 687–697, Apr. 1999. [Online]. Available: http://www.sciencedirect.com/science/article/pii/S0266353898001213

[49] M. Kharrat *et al.*, "Influence of damage accumulation under fatigue loading on the AE-based health assessment of composite materials: Wave distortion and AE-features evolution as a function of damage level," *Composites Part A: Applied Science and Manufacturing*, vol. 109, pp. 615–627, Jun. 2018. [Online]. Available: http://www.sciencedirect.com/science/article/pii/S1359835X16300379

[50] "AEwin Software : Installation, Operation and User's Reference Manual," MISTRAS Group Inc., Princeton Juntion, NJ, USA, Technical report, 2011.

[51] M. Moevus, "Mécanismes d'endommagement, émission acoustique et durées de vie en fatigue statique du composite SiCf/[Si-B-C] aux températures intermédiaires," PhD dissertation, INSA Lyon, Lyon, Jan. 2007. [Online]. Available: http://www.theses.fr/2007ISAL0114

[52] E. Maillet *et al.*, "Damage monitoring and identification in SiC/SiC minicomposites using combined acousto-ultrasonics and acoustic emission," *Composites Part A: Applied Science and Manufacturing*, vol. 57, pp. 8–15, Feb. 2014. [Online]. Available: http://www.sciencedirect.com/science/article/pii/S1359835X13002856

[53] ——, "Real-time evaluation of energy attenuation: A novel approach to acoustic emission analysis for damage monitoring of ceramic matrix composites," *Journal of the European Ceramic Society*, vol. 34, no. 7, pp. 1673–1679, Jul. 2014. [Online]. Available: http://www.sciencedirect.com/science/article/pii/S0955221913006146

[54] S. Barré and M. L. Benzeggagh, "On the use of acoustic emission to investigate damage mechanisms in glass-fibre-reinforced polypropylene," *Composites Science and Technology*, vol. 52, no. 3, pp. 369–376, Jan. 1994. [Online]. Available: http://www.sciencedirect.com/science/article/pii/0266353894901716

[55] S. Huguet *et al.*, "Use of acoustic emission to identify damage modes in glass fibre reinforced polyester," *Composites Science and Technology*, vol. 62, pp. 1433–1444, Aug. 2002. [Online]. Available: http://www.sciencedirect.com/science/article/pii/S0266353802000878

[56] D. Scida, Z. Aboura, and M. L. Benzeggagh, "The effect of ageing on the damage events in woven-fibre composite materials under different loading conditions," *Composites Science and Technology*, vol. 62, no. 4, pp. 551–557, Mar. 2002. [Online]. Available: http://www.sciencedirect.com/science/article/pii/S0266353801001476

[57] P. J. de Groot, P. A. M. Wijnen, and R. B. F. Janssen, "Real-time frequency determination of acoustic emission for different fracture mechanisms in carbon/epoxy composites," *Composites Science and Technology*, vol. 55, no. 4, pp. 405–412, Jan. 1995. [Online]. Available: http://www.sciencedirect.com/science/article/pii/0266353895001212

[58] N. Godin *et al.*, "Clustering of acoustic emission signals collected during tensile tests on unidirectional glass/polyester composite using supervised and unsupervised classifiers," *NDT & E International*, vol. 37, no. 4, pp. 253–264, Jun. 2004. [Online]. Available: http://www.sciencedirect.com/science/article/pii/S096386950300135X

[59] R. Gutkin *et al.*, "On acoustic emission for failure investigation in CFRP: Pattern recognition and peak frequency analyses," *Mechanical Systems and Signal Processing*, vol. 25, no. 4, pp. 1393–1407, May 2011. [Online]. Available: http://www.sciencedirect.com/science/article/pii/S0888327010004176

[60] S.-E. Mechraoui, A. Laksimi, and S. Benmedakhene, "Reliability of damage mechanism localisation by acoustic emission on glass/epoxy composite material plate," *Composite Structures*, vol. 94, no. 5, pp. 1483–1494, Apr. 2012. [Online]. Available: http://www.sciencedirect.com/science/article/pii/S0263822311004521

[61] L. Li *et al.*, "Cluster analysis of acoustic emission signals for 2d and 3d woven glass/epoxy composites," *Composite Structures*, vol. 116, pp. 286–299, Sep. 2014. [Online]. Available: http://www.sciencedirect.com/science/article/pii/S0263822314002335

[62] V. Carvelli, A. D'Ettorre, and S. V. Lomov, "Acoustic emission and damage mode correlation in textile reinforced PPS composites," *Composite Structures*, vol. 163, pp. 399–409, Mar. 2017. [Online]. Available: http://www.sciencedirect.com/science/article/pii/S0263822316322619

[63] N. Godin, P. Reynaud, and G. Fantozzi, "Challenges and limitations in the identification of acoustic emission signature of damage mechanisms in composites materials," *Applied Sciences (Switzerland)*, vol. 8, no. 8, 2018. [Online]. Available: https://hal.archives-ouvertes.fr/hal-01916330

[64] S. V. Lomov *et al.*, "A comparative study of tensile properties of non-crimp 3d orthogonal weave and multi-layer plain weave E-glass composites. Part 1: Materials, methods and principal results," *Composites Part A: Applied Science and Manufacturing*, vol. 40, no. 8, pp. 1134–1143, Aug. 2009. [Online]. Available: https://linkinghub.elsevier.com/retrieve/pii/S1359835X09000815

[65] M. Karayaka and P. Kurath, "Deformation and Failure Behavior of Woven Composite Laminates," *Journal of Engineering Materials and Technology*, vol. 116, no. 2, pp. 222–232, Apr. 1994. [Online]. Available: http://dx.doi.org/10.1115/1.2904277

[66] M. Selezneva *et al.*, "Microscale experimental investigation of failure mechanisms in off-axis woven laminates at elevated temperatures," *Composites Part A: Applied Science and Manufacturing*, vol. 42, no. 11, pp. 1756–1763, Nov. 2011. [Online]. Available: http://www.sciencedirect.com/science/article/pii/S1359835X11002375

[67] E. Ahci and R. Talreja, "Characterization of viscoelasticity and damage in high temperature polymer matrix composites," *Composites Science and Technology*, vol. 66, no. 14, pp. 2506–2519, Nov. 2006. [Online]. Available: http://www.sciencedirect.com/science/article/pii/S0266353806000522

[68] L. J. Hart-Smith, "Application of the strain invariant failure theory (SIFT) to metals and fiber–polymer composites," *Philosophical Magazine*, vol. 90, no. 31-32, pp. 4263–4331, Nov. 2010. [Online]. Available: https://doi.org/10.1080/14786435.2010.510450

[69] R. T. Bocchieri and R. A. Schapery, "Time-Dependent Deformation and Damage Growth in a Rubber-Toughened Fiber Composite," *Mechanics of Time-Dependent Materials*, vol. 8, no. 2, pp. 137–167, Jun. 2004. [Online]. Available: https://link.springer.com/article/10.1023/B:MTDM.0000027682.24503.04

[70] J. Raghavan and M. Meshii, "Time-dependent damage in carbon fibre-reinforced polymer composites," *Composites Part A: Applied Science and Manufacturing*, vol. 27, no. 12, pp. 1223–1227, Jan. 1996. [Online]. Available: http://www.sciencedirect.com/science/article/pii/1359835X96000735

[71] A. Asadi and J. Raghavan, "Model for prediction of simultaneous time-dependent damage evolution in multiple plies of multidirectional polymer composite laminates and its influence on creep," *Composites Part B: Engineering*, vol. 79, pp. 359–373, Sep. 2015. [Online]. Available: http://www.sciencedirect.com/science/article/pii/S1359836815002772

[72] R. H. Moore and D. A. Dillard, "Time-dependent matrix cracking in cross-ply laminates," *Composites Science and Technology*, vol. 39, no. 1, pp. 1–12, Jan. 1990. [Online]. Available: http://www.sciencedirect.com/science/article/pii/0266353890900295

[73] K. Ogi and Y. Takao, "Evolution of Transverse Cracking in CF/Epoxy Cross-Ply Laminates under Creep Loading," *Journal of Reinforced Plastics and Composites*, vol. 18, no. 13, pp. 1220–1230, Sep. 1999. [Online]. Available: http://journals.sagepub.com/doi/abs/10.1177/073168449901801305

[74] A. Birur, A. Gupta, and J. Raghavan, "Creep Rupture of Multidirectional Polymer Composite Laminates — Influence of Time-Dependent Damage," *Journal of Engineering Materials and Technology*, vol. 128, no. 4, pp. 611–617, Jun. 2006. [Online]. Available: http://dx.doi.org/10.1115/1.2345454

[75] A. Birur, "Time-dependent damage evolution in multidirectional polymer matrix composite laminates," Master's thesis, Department of Mechanical and Manufacturing Engineering, University of Manitoba, Winnipeg, Manitoba, Canada, May 2008. [Online]. Available: http://mspace.lib.umanitoba.ca/xmlui/handle/1993/3035

[76] M. C. Lafarie-Frenot, D. Gamby, and T. H. Nguyen, "Experimental and numerical analysis of loading rate and temperature effects on matrix cracking in CFRP laminates," *Proceedings of the Institution of Mechanical Engineers, Part L: Journal of Materials: Design and Applications*, vol. 218, no. 1, pp. 47–53, Jan. 2004. [Online]. Available: http://journals.sagepub.com/doi/abs/10.1177/146442070421800106

[77] T. H. Nguyen and D. Gamby, "Effects of nonlinear viscoelastic behaviour and loading rate on transverse cracking in CFRP laminates," *Composites Science and Technology*, vol. 67, no. 3–4, pp. 438–452, Mar. 2007. [Online]. Available: http://www.sciencedirect.com/science/article/pii/S026635380600337X

[78] R. T. Bocchieri, R. A. Schapery, and M. R. Gorman, "Time-dependent Microcracking Detected in a Rubber-toughened Carbon-epoxy Composite by the Modal Acoustic Emission Method," *Journal of Composite Materials*, vol. 37, no. 5, pp. 421–451, Mar. 2003. [Online]. Available: https://doi.org/10.1177/0021998303037005058

[79] A. Gupta, "Creep of plain weave polymer matrix composites," PhD dissertation, Department of Mechanical and Manufacturing Engineering, University of Manitoba, Winnipeg, Manitoba, Canada, 2009. [Online]. Available: http://mspace.lib.umanitoba.ca/xmlui/handle/1993/3849

[80] Y. Lou and R. Schapery, "Viscoelastic Characterization of a Nonlinear Fiber-Reinforced Plastic," *Journal of Composite Materials*, vol. 5, no. 2, pp. 208–234, Feb. 1971. [Online]. Available: https://doi.org/10.1177/002199837100500206

[81] S. P. Zaoutsos and G. C. Papanicolaou, "On the influence of preloading in the nonlinear viscoelastic–viscoplastic response of carbon–epoxy composites," *Composites Science and Technology*, vol. 70, no. 6, pp. 922–929, Jun. 2010. [Online]. Available: http://www.sciencedirect.com/science/article/pii/S0266353810000655

[82] T. L. Anderson, *Fracture Mechanics: Fundamentals and Applications*, 3rd ed. CRC Press, Jun. 2005.

[83] H. Tada, P. C. Paris, and G. R. Irwin, *The Stress Analysis of Cracks Handbook*, 3rd ed. Three Park Avenue New York, NY 10016-5990: ASME, Jan. 2000, dOI: 10.1115/1.801535. [Online]. Available: http://ebooks.asmedigitalcollection.asme.org/book.aspx?bookid=230

[84] J. R. Rice, "A Path Independent Integral and the Approximate Analysis of Strain Concentration by Notches and Cracks," *Journal of Applied Mechanics*, vol. 35, no. 2, pp. 379–386, Jun. 1968.

[85] N. E. Dowling and J. A. Begley, "Fatigue Crack Growth During Gross Plasticity and the J-Integral," *Mechanics of Crack Growth*, Jan. 1976.

[86] J. A. Begley and J. D. Landes, "The J Integral as a Fracture Criterion," *Fracture Toughness: Part II*, Jan. 1972.

[87] D. Landes and J. A. Begley, "The Effect of Specimen Geometry on J^{ic}," *Fracture Toughness: Part II*, Jan. 1972.

[88] J. Rice, P. Paris, and J. Merkle, "Some Further Results of J-Integral Analysis and Estimates," *Progress in Flaw Growth and Fracture Toughness Testing*, Jan. 1973.

[89] J. D. G. Sumpter and C. E. Turner, "Method for Laboratory Determination of Jc," *Cracks and Fracture*, Jan. 1976.

[90] N. E. Dowling, "Geometry Effects and the J-Integral Approach to Elastic-Plastic Fatigue Crack Growth," *Cracks and Fracture*, Jan. 1976.

[91] M. J. Laffan *et al.*, "Translaminar fracture toughness testing of composites: A review," *Polymer Testing*, vol. 31, no. 3, pp. 481–489, May 2012.

[92] H. Zabala *et al.*, "Loading rate dependency on mode I interlaminar fracture toughness of unidirectional and woven carbon fibre epoxy composites," *Composite Structures*, vol. 121, no. Supplement C, pp. 75–82, Mar. 2015.

[93] S. Mall, G. E. Law, and M. Katouzian, "Loading Rate Effect on Interlaminar Fracture Toughness of a Thermoplastic Composite," *Journal of Composite Materials*, Jul. 1987.

[94] S. T. Pinho, P. Robinson, and L. Iannucci, "Developing a four point bend specimen to measure the mode I intralaminar fracture toughness of unidirectional laminated composites," *Composites Science and Technology*, vol. 69, no. 7, pp. 1303–1309, Jun. 2009. [Online]. Available: http://www.sciencedirect.com/science/article/pii/S0266353809001067

[95] ASTM, "E1922-04, Test Method for Translaminar Fracture Toughness of Laminated and Pultruded Polymer Matrix Composite Materials," ASTM International, Tech. Rep., 2015.

[96] M. Rokbi *et al.*, "On experimental investigation of failure process of woven-fabric composites," *Composites Science and Technology*, vol. 71, no. 11, pp. 1375–1384, Jul. 2011. [Online]. Available: http://www.sciencedirect.com/science/article/pii/S0266353811001655

[97] M. Chabchoub *et al.*, "Investigations on the mode I translaminar failure and determination of fracture toughness in woven-ply carbon fibers thermoplastic composites at high temperatures," *Applied Acoustics*, vol. 128, pp. 55–63, Dec. 2017. [Online]. Available: http://www.sciencedirect.com/science/article/pii/S0003682X17300932

[98] B. Vieille *et al.*, "A fracture mechanics approach using Acoustic Emission Technique to investigate damage evolution in woven-ply thermoplastic structures at temperatures higher than glass transition temperature," *Composites Part B: Engineering*, vol. 116, pp. 340–351, May 2017.

[99] B. Vieille, M. Chabchoub, and C. Gautrelet, "Influence of matrix ductility and toughness on strain energy release rate and failure behavior of woven-ply reinforced thermoplastic structures at high temperature," *Composites Part B: Engineering*, vol. 132, pp. 125–140, Jan. 2018.

[100] R. R. R. Souza *et al.*, "Translaminar fracture toughness and fatigue crack growth characterization of carbon-epoxy plain weave laminates," *Polymer Composites*, vol. 0, no. 0, 2019. [Online]. Available: https://onlinelibrary.wiley.com/doi/abs/10.1002/pc.25247

[101] M. Chabchoub *et al.*, "Determination of J-R curves by load separation criterion in highly ductile TP-based composites under high temperature conditions," *Composite Structures*, vol. 182, pp. 391–401, Dec. 2017. [Online]. Available: http://www.sciencedirect.com/science/article/pii/S0263822317304282

[102] R. Böhm and W. Hufenbach, "Experimentally based strategy for damage analysis of textile-reinforced composites under static loading," *Composites Science and Technology*, vol. 70, no. 9, pp. 1330–1337, Sep. 2010. [Online]. Available: http://www.sciencedirect.com/science/article/pii/S0266353810001375

[103] TORAYCA, "T300 Data Sheet," Torayca, Tech. Rep.

[104] TICONA, "Designing with Forton - Polyphenylene Sulfide," Ticona, Tech. Rep., 2006.

[105] Tencate, "Cetex PPS technical data sheet," Tencate advanced composites, Tech. Rep., 2014.

[106] W. Albouy, B. Vieille, and L. Taleb, "Influence of matrix ductility on the high-temperature fatigue behavior of off-axis woven-ply thermoplastic and thermoset

laminates," *International Journal of Fatigue*, vol. 63, pp. 85–96, Jun. 2014. [Online]. Available: http://www.sciencedirect.com/science/article/pii/S0142112314000115

[107] ——, "Influence of matrix ductility on the high-temperature fatigue behaviour of quasi-isotropic woven-ply thermoplastic and thermoset laminates," *Composites Part A: Applied Science and Manufacturing*, vol. 67, pp. 22–36, Dec. 2014. [Online]. Available: http://www.sciencedirect.com/science/article/pii/S1359835X14002103

[108] B. Gross and J. Srawley, "Stress-Intensity Factors for a Single-Edge-Notch Tension Speciment by Boundary Collocation of a Stress Function," Tech. Rep. NASA TN D-2395, 1964.

[109] W. Brown and J. Srawley, "Plane Strain Crack Toughness Testing of High Strength Metallic Materials," in *Plane Strain Crack Toughness Testing of High Strength Metallic Materials*. ASTM International, Jan. 1966. [Online]. Available: https://www.astm.org/DIGITAL_LIBRARY/STP/PAGES/STP44663S.htm

[110] J. F. Maire and J. L. Chaboche, "A new formulation of continuum damage mechanics (CDM) for composite materials," *Aerospace Science and Technology*, vol. 1, no. 4, pp. 247–257, Jun. 1997. [Online]. Available: http://www.sciencedirect.com/science/article/pii/S1270963897900353

[111] B. Vieille, "Evolution of the strain energy release rate during ductile or brittle failure in woven-ply reinforced thermoplastic laminates under high temperature conditions," *Polymer Composites*, vol. 40, no. 1, pp. 121–131, 2019.

[112] K. G. Dassios *et al.*, "Crack Growth Monitoring in Ceramic Matrix Composites by Combined Infrared Thermography and Acoustic Emission," *Journal of the American Ceramic Society*, vol. 97, no. 1, pp. 251–257, 2014.

[113] M. Saeedifar *et al.*, "Prediction of quasi-static delamination onset and growth in laminated composites by acoustic emission," *Composites Part B: Engineering*, vol. 85, pp. 113–122, Feb. 2016.

[114] E. Ernault *et al.*, "Influence of the Rigid Amorphous Fraction on the thermo-mechanical behavior of Carbon/PPS composites," in *Comptes Rendus des JNC 21*, Bordeaux, 2019, p. 11.

[115] P. Zuo *et al.*, "Thermal aging effects on overall mechanical behavior of short glass fiber-reinforced polyphenylene sulfide composites," *Polymer Engineering*

& Science, vol. 59, no. 4, pp. 765–772, 2019. [Online]. Available: https://onlinelibrary.wiley.com/doi/abs/10.1002/pen.25003